University of Alberta

The Combined Effect of Ceria and Chromium on the Ductility of NiAl

by

Joshua Robert Hines ©

A thesis submitted to the Faculty of Graduate Studies and Research in partial fulfillment of the requirements for the degree of Master of Science

in

Materials Engineering

Department of Chemical and Materials Engineering

Edmonton, Alberta

Fall 2007

Canada

Abstract

The combined effect of cerium or ceria with chromium on the room temperature ductility of NiAl was investigated. Alloy preparation techniques included vacuum induction melting followed by investment casting, as well as arc-melting. Alloy additions made included 2.25 at.% Cr and/or 0.02 at.% cerium or the equivalent elemental mass in ceria. Both metallographic and fractographic characterizations were employed along with hardness and compression testing. The maximum ductility, defined as strain at peak load, was 12.8% for the alloy with ceria and chromium addition. This ductility result was not higher than values found in literature for stoichiometric NiAl. Unlike in other studies, one significant observation was that the addition of chromium did not seem to affect the ductility of NiAl in a detrimental manner.

Acknowledgements

I would like to thank the following people:

My wife, Stefanie, for your patience and encouragement that helped me get through when the end seemed unattainable.

My mother, for teaching me that I can do anything I put my mind to and encouraging me to always do my best, and my father, for your insatiable curiosity and showing me that you should never stop learning. Without the support you have both given me over the last nine years, I would not be where I am today.

My supervisor, Dr. Weixing Chen, for his guidance and expertise.

Table of Contents

List of Tables

List of Figures

1.0 Introduction

The equiatomic intermetallic in the nickel-aluminum system, NiAl, possesses certain properties that would make it a good candidate for high temperature structural applications including high melting temperature, low density relative to current superalloys, high thermal conductivity, and resistance to oxidizing, carburizing, and sulfidizing environments. However, other properties stand as serious obstacles to its application: poor creep resistance in the un-alloyed condition, insufficient high temperature strength, and almost no polycrystalline ductility below 400°C. Of these limiting properties, improvements have been made to the creep resistance and high temperature strength through precipitation hardening, but no progress to date has been made on the room temperature ductility.

Based on some of the potential in slip modification seen from chromium as well as the beneficial effect of ceria on NiAl coatings, the direction of this research has been selected. Additions of ceria with chromium as well as cerium with chromium have been made to NiAl with the hope of improving the room temperature ductility. Characterization methods including metallography and fractography were employed along with hardness and compression testing in order to determine the affect of combined cerium/ceria and chromium additions on NiAl.

1

A literature review of the current state of research emphasizing room temperature ductility and the effect of alloy addition is included in Section 2. Experimental methods used are detailed in Section 3. Results and discussion of characterization and testing on investment cast and arc-melted alloys are contained in Sections 4 and 5. A general discussion and conclusion are included in Sections 6 and 7.

2

2.0 Literature Review

This literature review will consist of an introduction to the nickel–aluminum system, with a brief discussion of Ni_3Al followed by a thorough overview of the physical and mechanical properties of NiAl. Emphasis will be placed on room temperature mechanical properties and in particular ductility as it is the major limiting factor to the application of NiAl as a structural intermetallic.

2.1 Nickel-Aluminum System

The nickel-aluminum system encompasses a number of intermetallic compounds, but by far the most important are NiAl and Ni_3Al (Figure 1). Both of these compounds exhibit a very high degree of order right up to their melting temperatures and exist over a relatively large composition range. Both have good oxidation resistance and high melting points making them good candidates for high temperature structural materials.

The immediate section will deal only with Ni_3Al as NiAl will be the topic of the rest of this literature review and will be discussed in greater detail in the following sections.

3
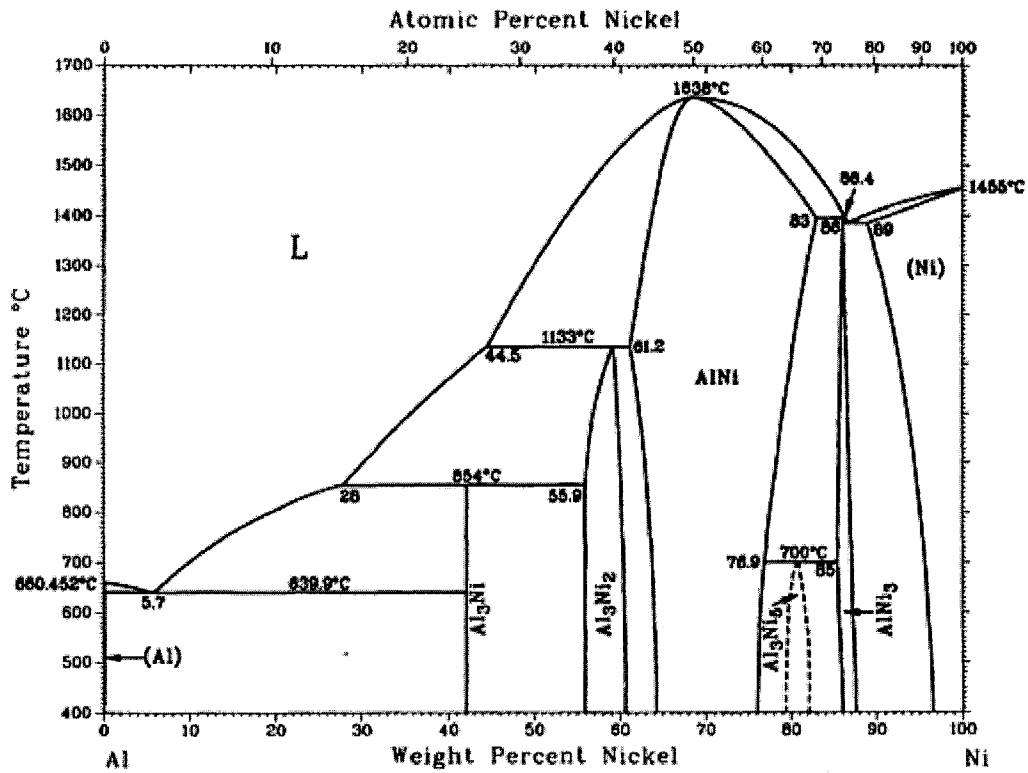
Figure 1: Al-Ni System Phase Diagram [1]

2.2 Ni$_3$Al

This compound is the most nickel-rich intermetallic of the nickel-aluminum system, existing from approximately 73 to 76 at.% nickel at room temperature with a narrowing phase field at higher temperatures [2]. Ni$_3$Al, commonly referred to as γ', is probably the single most important strengthening phase in high temperature nickel superalloys leading to their high temperature strength and creep resistance. This compound is highly ordered and maintains an L1$_2$ structure as shown in Figure 2, up to its melting point of 1397°C [3]. Deviations from the ideal stoichiometry of 25 at.% aluminum are accommodated through

4

the formation of anti-site defects consisting of either nickel or aluminum atoms on the opposite sub-lattice [4]. Unlike some other intermetallics, Ni_3Al has a high thermal vacancy enthalpy of formation and therefore the thermal vacancy concentrations are relatively low and have limited effect on the mechanical properties [5].
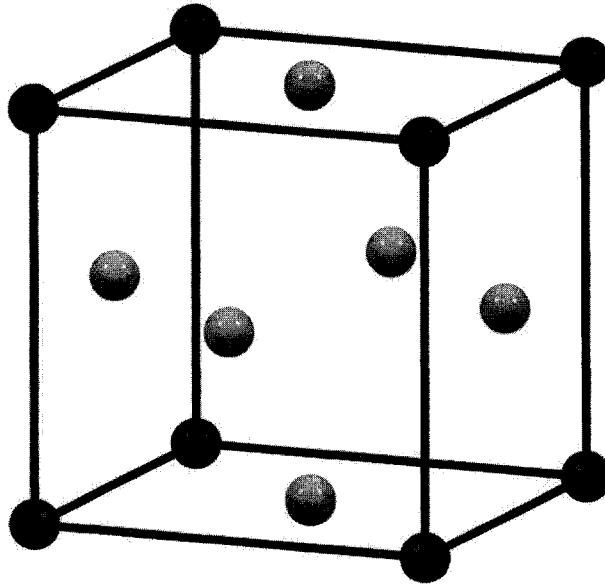
Figure 2: L1$_2$ Structure, Ni$_3$Al

Although this intermetallic has a relatively high melting temperature and good environmental resistances that include both oxidizing and carburizing environments, its intermediate temperature strength is its most advantageous property. Ni_3Al displays an anomalous yielding behaviour that results in increasing flow stress from room temperature to about 700°C [6]. This yielding behaviour is the result of <110> dislocations dissociating into super-partials, $\frac{a}{2}[110] \rightarrow \frac{a}{6}[211] + \frac{a}{6}[1\overline{1}2]$, and slipping from the {111} to the {100} planes where they become sessile and impede other dislocation motion.

5

There are also a number of problems or challenges facing the use of Ni_3Al as a high temperature structural material. This intermetallic suffers from brittle grain boundaries leading to very limited ductility at room temperature in the polycrystalline form. In addition to the brittle grain boundary issue, poor high temperature strength (>700°C) and high temperature environmental embrittlement (600 to 800°C) result in challenges to industrial application [7, 8].

It was originally thought that the poor polycrystalline ductility was due to impurities on the grain boundaries as Ni_3Al single crystals exhibit ample ductility at room temperature. The use of Auger electron microscopy revealed that even with very clean grain boundaries, poor ductility persists[8]. It has been proposed that there may be two mechanisms involved in the grain boundary embrittlement. The first and most widely accepted of these mechanisms is the hydrogen embrittlement of the grain boundary regions. This embrittlement is a result of the reaction between aluminum and the moisture in the air to produce aluminum oxide and hydrogen, which then diffuses into the material [7]. The second mechanism that has been proposed is that, due to the difficulty in transmitting slip across the grain boundaries, dislocation pileups cause crack nucleation. This behaviour has also been described as "poor grain boundary cohesion" [9].

6

The problem of polycrystalline grain boundary ductility can be solved in the case of aluminum deficient alloys (<25 at.%) with micro-additions of boron. Additions of 500 to 1000 ppm are sufficient to control both the environmental embrittlement and poor grain boundary cohesion resulting in an increase in tensile ductility from approximately 3% in the unalloyed condition to as much as 50% with alloying [6]. Research suggests that boron decreases the ordering energy of the grain boundary region allowing easier slip transfer from one grain to another [7].

Another type of embrittlement that affects this intermetallic compound is known as internal oxidation. Internal oxidation occurs as a result of oxygen diffusion along the grain boundaries at high temperatures (>700°C), resulting in decreased ductility and intergranular fracture [10]. This high temperature embrittlement can be eliminated through the addition of chromium on the order of 8 at.%, which helps to form a self-healing oxide coating preventing oxygen diffusion down the grain boundaries.

Above the temperature at which anomalous yielding takes place (~700°C), there is a rapid drop in strength through the advent of thermally activated dislocation climb. This decrease in strength can be addressed through the addition of Zr, Mo and Hf which act as solid solution hardening elements [10].

Although alloys of Ni_3Al have been produced with sufficient ductility, oxidation resistance, and high temperature strength, their properties cannot compete with some of the newer single crystal nickel superalloys currently used for high temperature turbine blades. However, there are many other applications where these alloys are well suited, including the following: [11]

- Gas, water, and stream turbines (cavitation, erosion, oxidation resistance);
- Aircraft fasteners (low density and high strength);
- Automotive turbochargers (high fatigue resistance and low density);
- Pistons and valves (wear resistance);
- Tooling (high-temperature strength and wear resistance); and
- Permanent molds.

One of the most recent applications of an Ni_3Al alloy is for transfer rolls in a steel hardening furnace where temperatures of 900 to 1000°C are experienced [12]. In this environment, the carburization and oxidation resistance, as well as the high temperature strength and fatigue resistance, are utilized. The rolls are fabricated through the centrifugal casting of the roll body and ingot casting followed by electrical discharge machining for the ends. The Exo-Melt™ process [13] was used for production of the molten intermetallic necessary for casting, and gas tungsten arc welding was used to attach the ends to the roll. In total, 220 rolls with 14-inch O.D., 2-inch wall thickness, and 164-inch lengths were produced in four months. This involved 220 automated gas tungsten arc welds, which was the largest number of welds successfully produced in an intermetallic alloy.

8

The purpose of this overview of the Ni_3Al compound was to show the difficulties involved with its application as a structural intermetallic as well as the solutions that have been found. Issues such as poor room temperature ductility, low high temperature strength, and insufficient high temperature environmental resistance have been overcome to a point where application of Ni_3Al as a high temperature structural material has been realized.

2.3 NiAl

The equiatomic intermetallic in the nickel-aluminum system has both the widest phase field and the highest melting temperature. The coupling of this high melting temperature along with its low density, high thermal conductivity, and good oxidation resistance make NiAl a promising candidate as a high temperature structural material. NiAl has a potential peak operating temperature higher than any of the currently applied alloys. As will be discussed in the following sections, there are also many problems associated with the use of NiAl as a high temperature structural material that must be overcome in order for this material to be applied industrially.

2.3.1 Physical Properties

2.3.1.1 Bonding and Crystal Structure

The bonding in NiAl is very strong, which leads to its high melting temperature (1638°C) and enthalpy of formation (-72 KJ/mol) [14]. The nature of the bonding is still widely argued, but the most accepted description is that of strong

9

Ni d − Al p hybridization along the <111> directions, which represent nearest neighbour A-B bonding, and weak ionic bonding in the <100> directions, which represents the nearest neighbour A-A or B-B bonding [15]. This directional difference in bonding character and strength is said to explain the elastic anisotropy shown in NiAl single crystals. In fact, the bonding between the nickel and aluminum atoms is so favourable that short range order is even maintained in the molten state at the 50 at.% composition [16]. Much research has been done in the last 10 years on the effect of ternary alloy additions on the electronic structure of NiAl through computer-based modelling, but the results are often found to be contradictory to other research and experimental findings and will thus be omitted from this literature review.

The nickel and aluminum atoms in stoichiometric nickel aluminide are arranged in the B2 structure that is shown in Figure 3, from nickel contents of 45.3 to 60.5 at.% [17]. The lattice parameter of NiAl is 0.2887 nm at the 50 at.% composition [18] and decreases with deviation from the stoichiometric composition in either the nickel- or aluminum-rich directions according to the following correlations [19]:

50 to 60 at.% Ni:
$$a_o(nm) = 0.299839 - 0.000222 \ (at.\% \ Ni)$$

45 to 50 at.% Ni:
$$a_o(nm) = 0.266819 + 0.000438 \ (at.\% \ Ni)$$

Deviations from stoichiometry are accommodated through anti-site and/or vacancy-type point defects [17]. In the case of an aluminum-rich composition,

10

nickel vacancies are formed due to the larger size of the aluminum atom, whereas in the nickel-rich case, nickel can occupy the aluminum sub-lattice. Although the behaviour stated above is widely accepted, some research has shown that up to 1 at.% aluminum can occupy the nickel sub-lattice before vacancies are formed [20].
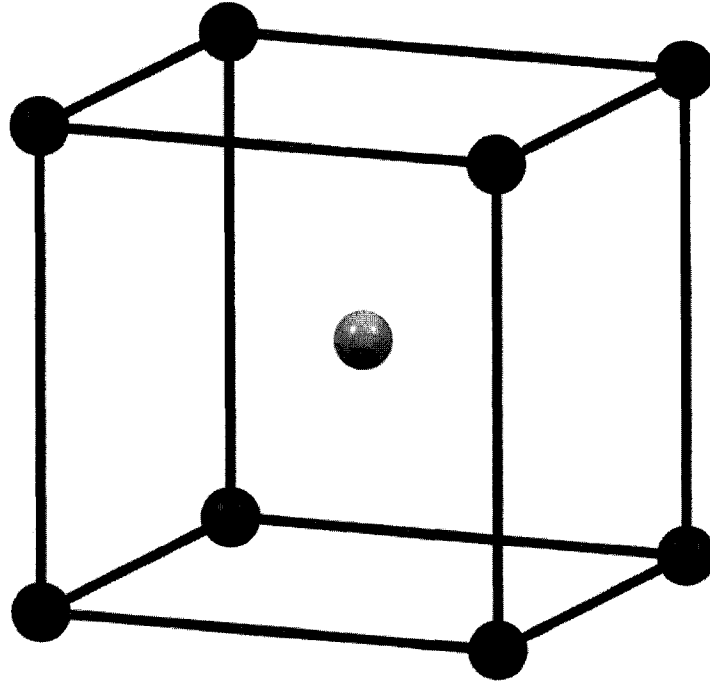
Figure 3: B2 Structure of NiAl

In addition to constitutional vacancies, thermal vacancies are formed upon heating of NiAl. Unlike the case of disordered materials, vacancies are formed in pairs in ordered crystals. In the case of NiAl, up to 2% thermal vacancies can be present at its melting temperature and 0.5 to 1% of these can be retained upon quenching [21, 22]. The formation mechanisms for thermal vacancies are affected by composition in the case of NiAl. As a result of the larger size of the aluminum atom in comparison to nickel, the aluminum sub-lattice is always full,

11

reducing the strain on the lattice. Consequently, in the case of nickel-rich stoichiometry, thermal vacancy formation may involve a triple-point defect which includes an anti-site defect along with two lattice vacancies. Initially, vacancies are formed on both sub-lattices. This is followed by a nickel atom shifting to the aluminum sub-lattice in the form of an anti-site atom in order to reduce the overall strain on the lattice [23]. The order of events described above was provided for illustrative purposes; although not necessarily correct, the final outcome is the same. It should be noted that despite this type of triple defect being seen in other ordered CsCl-type structures, concrete evidence of this has not been found in highly ordered crystals like NiAl. Nevertheless, it can be used to explain the large thermal vacancy concentrations that can be quenched into the NiAl lattice. In the case of the stoichiometric or aluminum-rich compositions, vacancies form in pairs with no associated anti-site defect because of the larger size of the aluminum atom.

As a result of the widening of the NiAl phase field with increasing temperature (as illustrated in Figure 1), a martensitic-type transformation is possible in the 32 to 40 at.% aluminum composition range [24]. Here, upon rapid cooling from the single phase region, the B2 crystal can transform into a face-centred tetragonal $L1_0$ structure [25] or a rhombohedral-type cell with 7R stacking in the Ramsdell notation [26]. This transformation satisfies all of the criteria necessary for a reversible shape memory effect.

2.3.1.2 Density

The density of NiAl is a function of composition as the densities of nickel and aluminum are quite different (8.9 and 2.70 g/cm^3, respectively) [27]. NiAl has a density of approximately 5.90 g/cm^3 at the stoichiometric composition and densities of 5.35 and 6.50 g/cm^3 at the aluminum- and nickel-rich sides of the phase field [17, 18, 20]. The intermediate densities conform to the following correlations compiled by Noebe et al. [19]:

50 to 60 at.% Ni:
$$\rho(g/cm^3) = 3.15 + 0.055 \, (at.\% \, Ni)$$

45 to 50 at.% Ni:
$$\rho(g/cm^3) = 0.118 \, (at.\% \, Ni)$$

It should be noted that the rate of change in the density is greater on the aluminum side of stoichiometry. This can easily be justified if the compositional defect structure is considered. On the aluminum-rich side, the extra aluminum cannot occupy the nickel lattice to any significant extent and therefore nickel vacancies are formed, resulting in an amplified density decrease. Alternately, in the case of excess nickel atoms, anti-site defects are formed and there is no significant increase in vacancy concentration. The density information again justifies the accepted constitutional point defect mechanisms.

The density of NiAl is approximately 66% of the current nickel superalloys, which makes it attractive as a jet engine turbine blade material. Such a decrease

13

in the weight of the turbine blades would allow the rest of the components to be smaller since they would have less centrifugal force to support [28].

2.3.1.3 Melting

As seen in the Ni-Al phase diagram (Figure 1), nickel aluminide melts congruently at 1638°C at the stoichiometric composition. The melting temperature decreases on either side of the 50:50 composition, but is still remains high at values of approximately 1580 and 1600°C for the liquidus temperature at 45.3 and 60.5 at.% Ni, respectively.

2.3.1.4 Modulus

The elastic modulus of single crystal NiAl is highly anisotropic, with a Zener's anisotropy factor of $A = 2C_{44}/(C_{11}-C_{12})$ being between 3.3 and 3.7 for the stoichiometric composition [29, 30]. This anisotropic behaviour is moderately dependent on temperature, falling to 2.94 at 600°C, and strongly dependent on composition, ranging from 1.85 to 5.67 for 45 and 55 at.% Ni compositions, respectively [30]. The resulting elastic moduli are only weakly dependent on composition, but they do vary with temperature according to the following correlations developed by Wasilewski [29]:

$$E <100> = 94.53 - 1.29 \times 10^{-2} T \ (GPa)$$
$$E <110> = 184.64 - 3.49 \times 10^{-2} T \ (GPa)$$
$$E <111> = 270.62 - 7.10 \times 10^{-2} T \ (GPa)$$
(Temperature in °C)

14

At 20°C, the above correlations yield elastic moduli of 94.27, 183.94, and 269.2 GPa for the <100>, <110>, and <111> directions, respectively.

The elastic modulus of polycrystalline cast and homogenized NiAl was found to be nearly independent of composition, with an almost linear relationship with temperature described by the following correlation [31]:

$$E = 204.9 - 0.041 \ (T + 273) \ (GPa)$$
$$(\text{Temperature in } °C)$$

According to the above equation, the room temperature (20°C) elastic modulus is 192.89 GPa, which is in agreement with currently accepted values. It should be noted that reported values of the elastic modulus vary greatly due to the processing method employed [19]. This variation in the elastic behaviour is a result of thermo-mechanical processes such as hot extrusion. This processing method, which is quite popular in NiAl research, normally results in the formation of some degree of texture and as a result of the strongly anisotropic nature outlined above, the elastic modulus can vary greatly. An example of the severity of the texture effect is evident in the elastic modulus of hot extruded powder processed NiAl, which was reported by Harmouche and Wolfenden [32] as being 237 GPa at the stoichiometric composition at 20°C.

In the nickel-rich compositions, as mentioned in Section 2.3.1.1, a reversible shear-type transformation occurs and the elastic modulus exhibits the associated behaviour in this region.

15

2.3.1.5 Thermal Conductivity

The thermal conductivity of NiAl is strongly affected by its composition or location in the phase field, as well as by ternary alloy additions. When looking at Figure 4, it is quite clear that the thermal conductivity of nickel aluminide is at a maximum of approximately 92 W/mK [33] at the stoichiometric composition. With deviations from stoichiometry in either direction, there is a rapid decrease in the thermal conductivity. This decrease results from the apparent disruptive effect of point defects on the periodicity of electron waves that are necessary to transfer thermal energy through the solid [33].

16
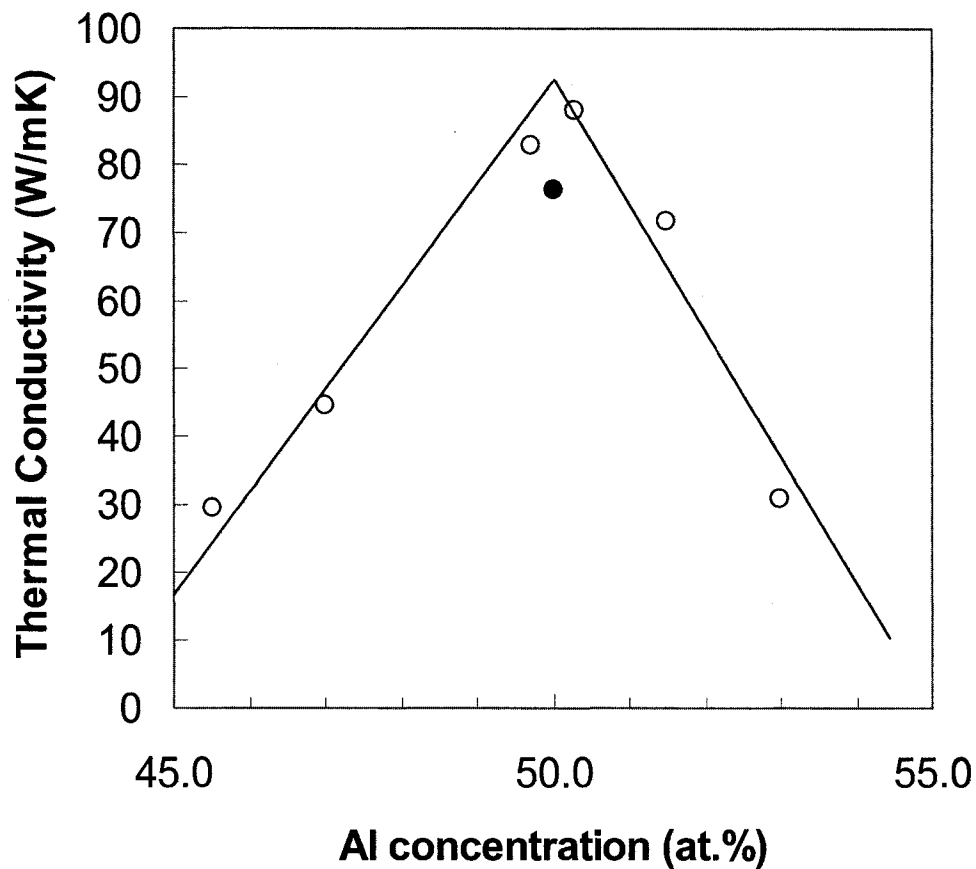
Figure 4: Effect of Composition on the Thermal Conductivity of Nickel, Iron, Cobalt, and Manganese Aluminides [33] (The solid point represents data from Darolia, 1991 [34]).

Investigations on the effects of ternary alloy additions on the thermal conductivity of NiAl are by no means complete, but a summary of some of the strategic elements used for alloying is shown in Figure 5. It can be seen that the thermal conductivity varies greatly from one alloy addition to another, and also it depends on which constituent the addition is substituted for. Ternary additions on the order of approximately 2 at.% result in a marked drop in thermal conductivity. The maximum point in Figure 5 represents the thermal

17

conductivity of stoichiometric NiAl and is consistent with that represented in Figure 4.

It can also be seen from Figure 5 that the ratio of nickel to aluminum is quite influential on the thermal conductivity. In the case of some additions, such as gallium and cobalt, the severity of the conductivity decrease depends greatly on the NiAl constituent for which they are substituted. This varied effect is a result of the preferred site occupancy and the resulting point defects generated by the alloy addition. For example, gallium prefers to occupy the nickel sub-lattice and therefore affects the thermal conductivity less if it is substituted for nickel. On the other hand, cobalt prefers to occupy the aluminum sub-lattice and therefore would result in the least affect on thermal conductivity when added to nickel-rich NiAl. If cobalt were substituted for nickel, it would occupy the aluminum sub-lattice and generate constitutional vacancies on the nickel sub-lattice. Some alloy additions, including iron and copper will occupy either of the lattice sites with little preference and thus have comparable thermal conductivities in either substitution case.

18
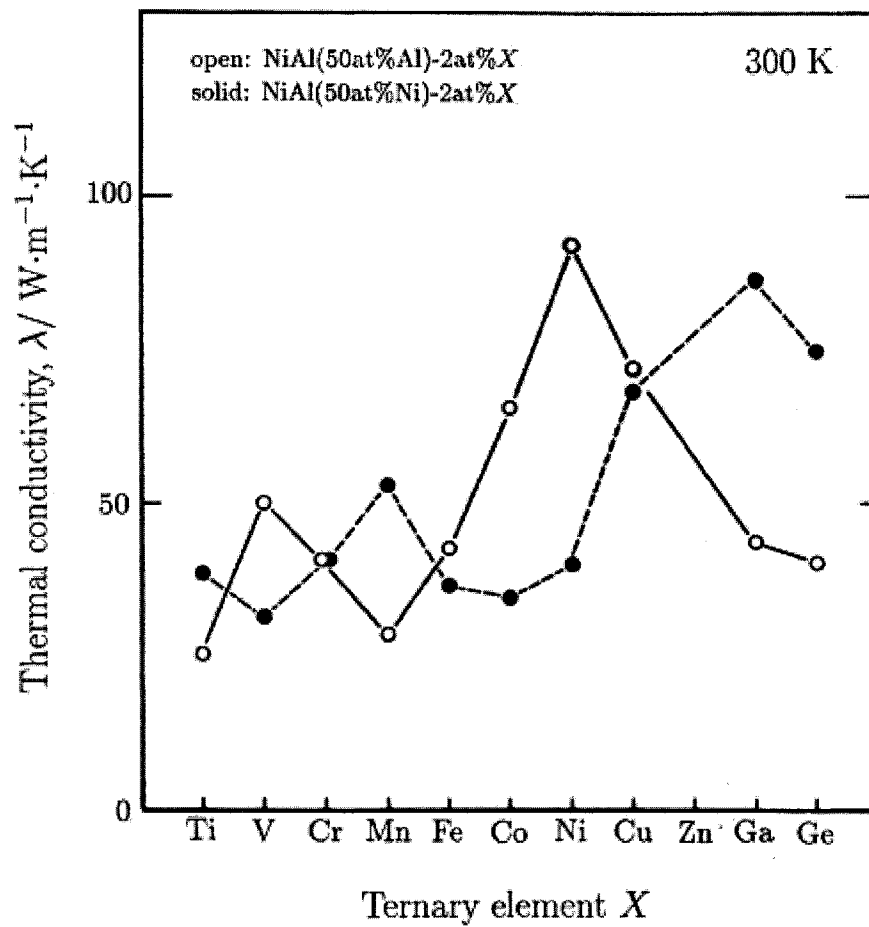
Figure 5: Effect of Ternary Element Additions on the Conductivity of NiAl [35]

In general, the thermal conductivity of NiAl increases rather rapidly up to about 600°C and then levels off. Figure 6 summarizes the effect of select ternary alloy additions on the temperature dependence of the thermal conductivity of nickel aluminide.

19
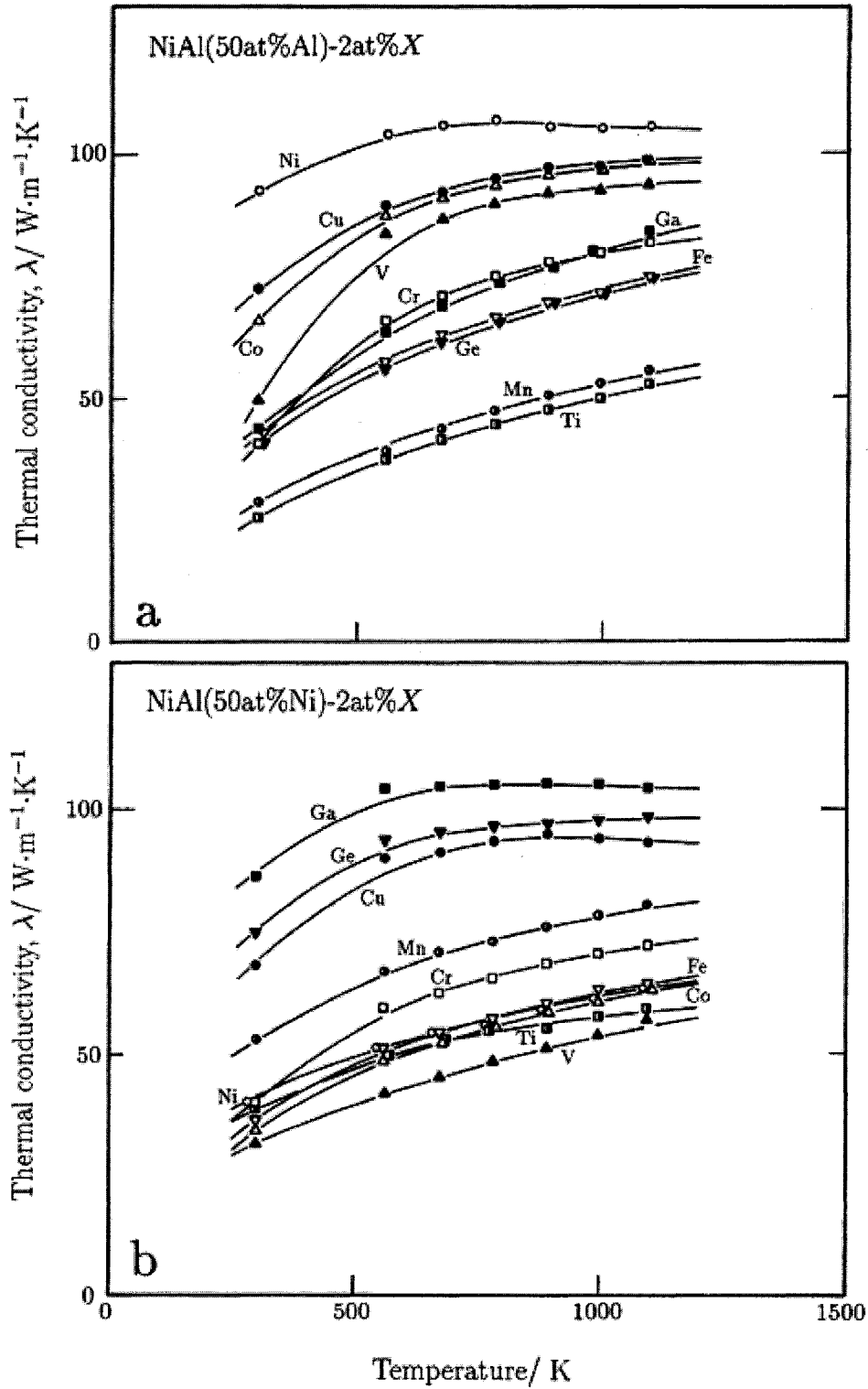
Figure 6: Temperature Dependence of Thermal Conductivity of NiAl with Alloy Additions
[35]

20

The relatively high thermal conductivity of NiAl compared with current superalloys is instrumental in its potential use as turbine blade material in jet engines. Higher thermal conductivity makes active cooling more effective, allowing for higher operating temperatures.

2.3.1.6 Oxidation Resistance

The oxidation resistance of NiAl is by far its most important asset. The generation of a self-healing aluminum oxide coating up to temperatures as high as 1200°C [36] makes NiAl attractive as a high temperature material and is the reason for its use over the last three decades as a protective coating for superalloys used in gas turbine engines [37].

NiAl in its pure form generates different oxide coatings in different temperature ranges. At temperatures around and just below 800°C, the initial oxide formed is a combination of $NiAl_2O_4(s)$ and δ-Al_2O_3, which then grow into θ-Al_2O_3 after around 10 hours at 800°C [38]. At temperatures around 700°C, a γ modification of Al_2O_3 produces the stable oxide form. It is not until temperatures reach between 950 and 1050°C that the final transformation from the θ-Al_2O_3 to the desirable α-Al_2O_3 structure occurs [39]. The particulars of the transient oxides outlined above are not as important to this discussion as the understanding of the oxidation process being a transient one. During the transition from the θ- to α-Al_2O_3 oxide modifications, there is a large volume change that introduces stresses and results in spalling of the oxide layer. This transformation-induced spalling results in a higher overall oxidation rate and is therefore not desirable. It

21

should also be noted that the kinetics of transient oxide growth are much faster than the growth of the α-Al$_2$O$_3$ oxide and thus ideally these regions would be avoided [38].

Through the addition of certain alloys the oxidation properties of NiAl can be improved. For example, chromium is known to increase the oxidation resistance of NiAl in the 900 to 1000°C range by introducing Cr$_2$O$_3$ into the oxide which acts to accelerate the transformation from θ- to α-Al$_2$O$_3$ [39]. The addition of oxygen-active elements, Y, Zr, Hf, Ce, and La, is also known to increase the oxidation resistance of NiAl, but through means that are not completely understood [5]. Zirconium and cerium in particular are known to increase the thermal cycling resistance of NiAl and NiAl-based coatings [40, 41].

NiAl does not suffer from the phenomenon known as pesting, to which many intermetallics are susceptible. Pesting involves internal oxidation by way of oxygen diffusion along the grain boundaries, which can result in turning a sample to dust. The grain boundary area is oxidized away and the grains fall apart freely. The only reports of this phenomenon occurring are in the cases of very low oxygen partial pressures where a stable oxide layer cannot form [42].

2.3.2 Mechanical Properties

Although many of the physical properties of NiAl, discussed above, lend it to being a potential high temperature structural material, some of the mechanical properties have proven to be substantial barriers to implementation. Issues,

22

including low room temperature ductility, poor high temperature strength, and poor creep resistance must be addressed before implementation as a structural material can be realized.

Discussion of mechanical properties in this literature review will be limited to ductility and related properties, such as ductile to brittle transition temperature fracture.

2.3.2.1 Room Temperature Ductility

NiAl exhibits poor polycrystalline room temperature ductility stemming from its possession of only three active slip systems, <100>{011}. It is known that to transfer adequate slip across a grain boundary, resulting in polycrystalline ductility, there must be at least five independent slip systems [43]. Some of the first mechanical studies of NiAl were conducted in the 1960s by Rozner and Wasilewski [44], and Ball and Smallman [45, 46]. At this early stage in the investigation there was some disagreement on the tensile ductility of NiAl. Rozner and Wasilewski [44] published reports of 4% tensile ductility at room temperature, while Ball and Smallman [46] and Grala [47] reported no ductility at room temperature. Hahn and Vedula [48] later published a tensile ductility value of 2.3%, while Nagpal and Baker [49] also reported 2.3%. All cases, where ductility has been reported, have employed hot extrusion of alloys of the stoichiometric composition.

23

Polycrystalline NiAl in compression has been reported to exhibit much higher ductility in tension [50]. This increased ductility brings to light the question of the definition of failure in compression. Unlike tensile failure, compressive failure usually results from the joining of a number of cracks, which leads to the loss of load bearing capacity. Often, the non-linear deformation can include crack propagation as well as dislocation motion. This can help in the understanding of the wide range of compressive ductility in polycrystalline NiAl found in literature. However, compressive strains to failure are generally reported as nil [49] or as values as high as 12 [51] and 17% [52].

NiAl has been found to deform at room temperature predominantly by <100> dislocations on {011} planes, but it has also been found to slip by <100> dislocations on the {001} planes [11, 44, 45, 53-55]. Although it was originally thought that <011> dislocations were active in NiAl at room temperature, it is now mainly accepted that evidence of their existence in deformed polycrystalline samples found through transmission electron microscopy (TEM) examination is a result of <100> dislocation interactions [53, 54, 56]. Having said this, compressive tests on NiAl bi-crystals consisting of one crystal in the soft orientation beside a crystal in a hard orientation have shown evidence of <110>{110} slip originating in the hard-orientated crystal from <100> dislocation pileups at the interface in the soft-oriented crystal [57]. The significance of this finding is uncertain as this has never been witnessed in polycrystals in compression or tension.

Other possible, non-active slip systems in NiAl are <110> dislocations on {110} planes, mentioned above, and <111> dislocations on {110} planes. The <110> dislocation has a longer burgers vector and thus, as expected, have a higher critical resolved shear stress than that of 70 MPa belonging to the experimentally observed <100> dislocation on the {110} plane [45, 52, 55]. Although the burgers vector of the <111> dislocation is shorter than either the <100> or <110> dislocations, this direction requires the production of an anti-phase region.

The ductility of NiAl drastically increases at temperatures above 400°C, where thermally-induced dislocation climb and glide are responsible for tensile elongations of up to 40% at 600°C [48]. Although <110> dislocations have been observed at temperatures above 400°C in the hard-orientation single crystal NiAl, [52, 58], only <110> dislocations resulting from <100> interactions have been observed in polycrystalline NiAl.

One of the suggested solutions for an increase in the room temperature ductility of NiAl has been to attempt to activate the <111> dislocation. As mentioned above, the dislocation line energy is much higher than that of the <100> dislocation. If this dislocation were to travel in pairs, the critical resolved shear stress calculated from the length of the burgers vector would be greatly reduced. Unfortunately, observations of <111> super-lattice dislocations in hard-oriented

25

single crystals have only been identified indirectly. Fischer et al. [59] saw evidence of an anti-phase boundary in NiAl with chromium addition using atom probe field ion microscopy. Through the use of computer modelling and simulation, the APB energy of NiAl has been found to decrease with large additions of Ni (10%), Cr, Mn, or V (17%) [60-62]. The problem with these findings is that in the case of the Cr, Mn, and V, the required addition is far above the solid solubility of the additives in the matrix. In the case of Ni additions, 10% Ni added from stoichiometry would result in a two-phase alloy. Exclusive of the solubility and phase limit issues, the question of the effect of these additions on the ordering energy must be asked. If these elemental additions lower the ordering energy, will they also negatively affect the high temperature properties? A more detailed discussion of the effect of alloy additions on the ductility of NiAl will be addressed separately in a section to follow.

2.3.2.2 Brittle to Ductile Transition

A large increase in the ductility of NiAl above a temperature of approximately 400°C was observed by Ball and Smallman [45] in 1966, and has since been verified by many others. Although there seems to be agreement on this ductility increase known as the brittle to ductile transition (BDT), the temperature at which it occurs is somewhat in dispute. Over the years, the ductile to brittle transition temperature (BDTT) has been reported to be as low as 277°C [44, 48] and as high as 727°C [47]. This discrepancy can be attributed to the dependency

26

of BDT on parameters such as Ni:Al ratio, interstitial composition, strain rate, existing dislocation density and makeup (processing), grain size, and ternary alloy addition [51, 63, 64]. Deviation from the stoichiometric composition, presence of interstitial elements, or increase in strain rate tends to increase the BDTT. Processing history seems to be a bit more complicated, with the one constant being the beneficial effect of extrusion. Evidence shows that extrusion leads to a decrease in BDTT through the generation of favourable texture and high volumes of mobile dislocations. On the other hand, heat treatment after extrusion can lead to pinning of mobile dislocations with interstitial elements, therefore increasing the BDTT. Research has shown that BDTT decreases with decreasing grain size [49, 64]; however, this effect is only encountered in the 275 to 475°C range. Considering the effect of ternary alloy additions, more have been found to decrease the BDTT of stoichiometric NiAl.

It was originally thought that the increase in ductility was a result of the activation of another slip system. Although <011> and <111> dislocations have been found in NiAl, no evidence of substantial dislocation activity other than <001> dislocations has been found to date. As a result, it is currently accepted that the increase in ductility experienced at the BDTT is a result of thermally-activated cross slip of <001> dislocations [50].

2.3.2.4 Fracture

There is general consensus that the room temperature fracture mode of stoichiometric NiAl is intergranular in nature [48, 52, 65, 66]; however, there has been some debate on the reasons for this. It was initially thought that intergranular fracture occurred as a result of impurities at the grain boundaries such as oxygen [67]. This impurity-based embrittlement theory has since been disproved through the use of Auger electron microscopy [66]. It has been found that in stoichiometric NiAl, which exhibits intergranular fracture, no impurities are present at the grain boundaries. These findings seem to support the theory of insufficient slip compatibility from one grain to another. In this situation, there would simply be a pile-up of dislocations at the grain boundary with increasing stress until intergranular fracture occurred.

Transgranular fracture has been found in off-stoichiometric and alloyed NiAl, in which cases fracture occurs before significant plastic deformation [19, 65, 68, 69]. In the case of stoichiometric departure or alloys addition, the result is almost exclusively that of an increase in flow stress (see Sections 2.3.1.1 addressing point defects and Section 2.3.2.1 discussing ductility). In the cases where transgranular fracture is observed, it is reasonable to assume that fracture is initiated in the grain interior as a result of hardening or strengthening of the NiAl matrix.

28

2.3.3 Alloy Additions

This section reviews the effect of ternary alloy additions on the ductility of NiAl. Micro-alloy additions, less than 1 at.%, will be discussed separately from macro-additions. Chromium will be addressed separately. Discussion of macro-additions will be limited to precipitate type two phase systems. Eutectic and directionally solidified systems will be omitted.

2.3.3.1 Micro-Alloying Additions

Interstitial Additions: Boron (B) and Carbon (C)

Due to its small size, boron is thought to occupy the octahedral site in the B2 structure of NiAl. Investigation by Law and Blackburn [68] indicated that 0.25% boron added to stoichiometric NiAl results in a change in the fracture mode from intergranular to transgranular, but yields no increase in ductility. George and Liu [66] arrived at a similar conclusion with 300 wppm boron suppressing intergranular fracture, but again leading to no increase in ductility. In addition to the change in fracture mode, solid solution hardening effects as high as 1500 MPa / at.% B were quantified. It was concluded by George and Liu that the change in fracture mode was somehow related to the observed segregation of boron to the grain boundaries. It was hypothesized that the boron somehow strengthens this region and therefore suppresses intergranular fracture. Although boron additions successfully suppress intergranular fracture, they significantly harden the matrix of NiAl and result in no increase in ductility.

29

In NiAl, carbon is inherently present as it is a common impurity in nickel. George and Liu [66] studied the impact of carbon on the mechanical properties of NiAl. Carbon additions of 300 ppm to stoichiometric NiAl resulted in solid solution hardening as high as 1700 MPa/at.% C (up to 300 ppm) with no change in fracture mode. Unlike boron, carbon was not found to segregate to the grain boundaries. Weaver and Noebe [70, 71] studied static strain ageing in NiAl using nitrogen, oxygen, and carbon and found carbon to be the element responsible for strain ageing. They also confirmed that there was no noticeable change in fracture mode as a result of carbon. Weaver and Noebe also found that reactive elements such as titanium will act as "getters" to carbon, eliminating the dislocation pinning ability.

Beryllium (Be)

The effect of beryllium addition to NiAl was also studied by George and Liu [66]. They found that beryllium additions of 500 ppm resulted in only 100 MPa/at.% Be hardening and no change in the fracture mode. Tensile elongations of 3% were obtained compared to 2% for the stoichiometric NiAl. Thus, it appears that beryllium may result in slight increases in ductility, but no effect on the slip system has been found.

Nitrogen (N)

Nitrogen addition, an interstitial occupier, was studied by Noebe and Garg [72] by means of gas atomization of molten NiAl, followed by powder compaction

30

and extrusion. Nitrogen was used for the atomizing gas resulting in a nitrogen content of 904 ppm. Results showed an increase in the yield strength from solid solution hardening and an increase in the tensile elongation from 1.5 to 2.75%. Results of the same alloy were published later by Weaver and Noebe [71] reporting a tensile yield increase of 85%, but with no significant increase in ductility compared with commercial or high purity stoichiometric NiAl. No appreciable change in the fracture mode was observed from nitrogen addition.

Titanium (Ti)

Alloy additions of titanium have been investigated for its ability to act as a "getter" to interstitial impurities, mainly carbon. Golberg and Sauthoff [73, 74] investigated the effect of 0.1 at.% Ti addition on the strain ageing phenomenon resulting from interstitial carbon. Although titanium addition eliminated the serrated yielding seen in the stoichiometric alloy, an almost 100% increase in the yield stress was seen with no increase in the strain to failure. It was concluded that although the carbon was tied up with the titanium, the fine titanium carbides restricted dislocation motion to a greater degree. No fracture mode information was given in this study.

Weaver and Noebe [71] also investigated the effect of titanium as a getter for carbon. Using additions of 0.03 at.% Ti to stoichiometric NiAl eliminated the yield point in tension. Unlike the previously mentioned study, the yield strength was basically unchanged, which is possible due to the lower addition levels. In

31

keeping with the unchanged yield stress, the fracture mode remained intergranular. Although the effects of carbon were eliminated, no increase in tensile ductility was achieved.

Most recently, Ebrahimi and Hoyle [75] added 1 at.% titanium to stoichiometric NiAl. Yield strength increases were 163% with a change in the fracture mode from intergranular to transgranular. The tensile ductility was drastically reduced from 2.8% for the stoichiometric alloy to just 0.22% for the 1 at.% Ti addition.

Although it appears that titanium can be used to successfully eliminate the effects of carbon on dislocation motion, no significant increase in ductility has been seen.

Iron (Fe), Gallium (Ga), and Molybdenum (Mo)

Detailed studies of iron, gallium, and molybdenum micro-alloy additions were performed by Darolia et al. using single crystals [76]. It was found that small additions of these elements lead to significant increases in the tensile ductility of single crystals in the soft orientation. Increases of 600, 100, and 450% were seen for iron, molybdenum, and gallium with additions of 0.25, 0.11, and 0.1 at.%, respectively. Gallium had no effect on the yield strength, while iron resulted in slight softening. Molybdenum additions resulted in a doubling of the yield strength because of small α-molybdenum precipitates. Gallium and iron yielded single phase microstructures.

32

The positive results in the single crystal study prompted an investigation of iron and gallium addition to polycrystalline NiAl by Noebe et al [77]. Using extruded alloys with 0.1 at.% Fe and Ga additions, poor tensile ductility was found. With yield strength increases of 13% over the stoichiometric specimen, the elongations fell from 1.4 to slightly less than 1% for both. The fracture mode increased in transgranular nature for both iron and gallium addition.

A separate study on the effects of molybdenum on polycrystalline NiAl was conducted by Liu and Horton [78]. Unlike iron and gallium, molybdenum additions resulted in a slight increase in polycrystalline ductility with elongations as high as 3.6% with 0.4% Mo addition. This molybdenum addition also resulted in increases in yield and tensile strengths of 65 and 73%, respectively. Both the stoichiometric composition and the alloy with molybdenum were reported as having mixed mode failure.

Although these micro-alloy additions seem to significantly improve the ductility of single crystals, only molybdenum shows any improvement in the polycrystalline form.

Zirconium

Additions of zirconium to NiAl have been found to result in an increase in yield strength and a change from intergranular to transgranular fracture with no

33

increase in ductility [65, 69]. Zirconium has been found to act as an effective getter for interstitial impurities, virtually eliminating static and dynamic strain ageing [73].

Liu and Horton [78] studied the combined effect of molybdenum and zirconium addition. Additions of 0.08, 0.2, 0.4, and 0.7% Zr were added to NiAl with 0.7% Mo, resulting in significant yield strength increases, but zero ductility. Considering that molybdenum additions of 0.7% alone resulted in 3.5% tensile elongation, it is clear that zirconium does not beneficially affect the ductility of NiAl at room temperature.

Phosphorus (P) and Silver (Ag)

Both phosphorus and silver additions have been investigated by Guo and Zhou [79, 80]. Phosphorus was reported to increase the ductility of NiAl when added in concentrations of 0.005, 0.02, and 0.05%. Compressive strains to failure were reported as 2, 9, and 6% for the previously mentioned concentrations, respectively. Yield strengths were shown to decrease to 570, 340, and 400 MPa from the non-alloyed value of 600 MPa. No elongation results for the stoichiometric NiAl were reported, which makes comparison difficult. The definition of failure was also not given. Since NiAl can continue to displace in compression after the formation of intergranular cracks, compressive crack growth is often misreported as ductility. Although these results are interesting, no room temperature follow-up work has been performed by the authors to date.

34

Guo and Zhou [79] found that small amounts of silver (0.5 and 1%) were found to increase compressive yield strength from 450 to 580 MPa and result in compressive strains to failure of 2.5%. Again, there was no ductility data for the stoichiometric NiAl presented for comparison. These strength increases were attributed to precipitation hardening.

Hafnium (Hf)

Golberg and Sauthoff [73] added Hf to soft-oriented single crystal NiAl in a concentration of 0.09%. With a solubility limit of 0.3 at.% [81], this addition resulted in solid solution hardening as well as a reduction in ductility. The compressive yield strength increased form 106.5 MPa for stoichiometric NiAl to 310.3 MPa, while the peak compressive stress increased from 464 to 631 MPa. The compressive strain to fracture changed from 9.1% for NiAl to 7.3% for NiAl with Hf.

The addition of 0.08% Hf combined with 0.7% Mo was investigated by Liu and Horton [78]. Results indicated that the addition of the 0.08% Hf to the molybdenum-containing alloy produced a decrease in tensile elongation from 3.4% to nil. There were increases in yield and tensile strengths from 254 to 566 MPa and 395 to 566 MPa, respectively. Fracture mode was a mix of intergranular and transgranular for the molybdenum and molybdenum-hafnium alloys.

35

Tantalum (Ta)

Micro-alloy additions of tantalum (0.2 at.%) were made to stoichiometric NiAl single crystals by Messerschmidt et al. [82]. Although no ductility data was given, an increase in yield strength from 220 to 380 MPa for a non-alloyed single crystal was seen. No second phase particles were seen using transmission electron microscopy (TEM) examination, indicating that the strength increase was a result of solid solution hardening.

Liu and Horton [78] added a combination of 1.5% Mo and 0.4% Ta, as well as a combination of 1.5% Mo and 1.0% Ta, to NiAl. The addition of 0.4% Ta to the molybdenum containing alloy reduced the tensile ductility from 4.4 to 2.9%, while the yield and tensile strengths changed from 276 to 328 MPa and 486 to 472 MPa, respectively. The alloy with 1.0% Ta and 1.5% Mo had a tensile ductility of 1.3%, a yield strength of 388 MPa, and a tensile strength of 413 MPa. The fracture mode remained a combination of intergranular and transgranular.

Niobium (Nb)

Additions of 0.4 and 1.0% Nb along with 1.5% molybdenum were also made by Liu and Horton [78]. Tensile ductility was reduced from 4.4% for the Mo alloy to 2.8 and 1.0% for additions of 0.4 and 1.0% Nb, respectively. Yield and tensile strength changed from 276 to 325 and 402 MPa and 486 to 466 and 431 MPa,

36

respectively. The failure mode remained a combination of intergranular and transgranular fracture.

Lanthanum (La)

Kovalev et al. [83] investigated the effects of 0.1% La additions of 0.1% to stoichiometric NiAl. Compression testing showed a strain to failure of 29.5% compared with 12% for the stoichiometric NiAl, while yield strength was 311 MPa compared with 292 MPa. In this study, the fracture mode shifted from 70% intergranular for NiAl to only 3% for the lanthanum-containing alloy. No extension of this work has been published. Without a definition of failure being given, it is likely that 29.5% compressive strain involved fracture propagation that would lead to immediate failure in tension.

Cerium (Ce) and Ceria (CeO₂)

Cerium has been used as an additive to NiAl coatings [84, 85]. There has been no investigation of the effect of cerium or ceria on the ductility or mechanical properties of bulk NiAl. In this research, the addition of ceria was found to increase the bonding of the coating to the substrate. Unpublished research conducted by Chen et al. at the University of Alberta, also indicated that the additions of ceria increased the resistance of HVOF thermal spreyed coatings to spalling or cracking from repeated thermal cycling. Micro-indentation and erosion results showed that ceria greatly increased the hardness of the coating as well as the erosion resistance. In addition, after the erosion testing of the

37

coatings, the ceria-containing specimens had a much different micro-crack appearance. The ceria-containing coating appeared to exhibit the appearance of ductile wear.

2.3.3.2 Macro-Alloying Additions

In order to increase the ductility of NiAl through alloy addition, the element would most likely have to be soluble. Additions above the solubility limit are usually utilized to increased high temperature strength or creep resistance. A summary of macro-alloy additions to NiAl is listed below.

Intermetallic Second Phase Formers

Additions of group IIIB, IVB, and VB elements from the periodic table tend to form second phase intermetallic compounds, normally Heusler phases (Ni_2AlX), when added to NiAl. These elements tend to have very low solubility due to their affinity to form ordered compounds. Elements that have been added to NiAl include scandium, titanium, vanadium, yttrium, zirconium, niobium, lanthanum, hafnium, and tantalum [86-93]. These ordered phases are desirable because of their stability at high temperature, leading to increases in high temperature strength and creep resistance, but no ductility improvements.

Iron (Fe)

Iron addition to NiAl has been investigated due to its similar structure and ductility at room temperature [93-95]. In addition, FeAl is known to deform by

38

motion of <111> dislocations [96]. Additions of iron, added for aluminum, less than 0.5% resulted in increased ductility in single crystals [76]. Similar increases in ductility were not seen for polycrystalline material. No ductility whatsoever was seen in a Ni-30Al-20Fe alloy [97]; an increase in ductility was not seen until 30% Fe was added for aluminum resulting in an eutectic structure. Miracle et al. [98] abandoned an investigation with additions of 10.3, 20.6, and 30.9% Fe to an alloy with 48.5% Al after compression specimens could not be successfully machined. A more recent study by Kovalev et al. [83] indicates a ductility increase in compression with 2% Fe addition to stoichiometric NiAl. Although an increase from 12 to 28% compressive strain is reported, no definition of compressive failure was given and these values could include post-fracture deformation. The material used by Kovalev was produced from alloyed powders, and the grain size was 7 microns.

Manganese (Mn)

The effects of macro-alloy additions of manganese to NiAl were investigated by Law and Blackburn [68]. They observed that a Ni-44Al-5Mn alloy deformed in compression to 2% showed slip of <111> dislocations on {112} planes. Although there seemed to be activation of <111> slip, there was no tensile ductility at room temperature.

39

2.3.3.3 Chromium (Cr) Addition to NiAl

Initially, research by Law and Blackburn [68] indicated that 5% Cr added to a polycrystalline, Ni-48.5Al alloy resulted in the existence of <111> dislocations. This observation was promising because activation of the <111> {112} slip system would result in five independent slip modes and should increase room temperature ductility. A subsequent study by Miracle et al. [98] confirmed the <111> dislocations in ahard-oriented single crystal alloy of the same composition after 0.5 and 1.5% compression. Although <111> dislocations were observed in both cases, their mobility was low and no significant increase in tensile ductility was seen.

The most thorough investigation to date of the effect chromium on NiAl was conducted by Cotton et al., and was published in his Ph.D thesis [51], and later in Intermetallics [99, 100]. Cotton looked at the effect of 1, 2, and 5% Cr additions on the mechanical properties, microstructure, and dislocation structure of NiAl. The effect of Ni:Al ratio was investigated by substituting Cr for Al, Ni, or both. The influence of processing method was considered with alloys being made by arc-melting and extrusion of vacuum-induction cast material. Results showed a solubility of approximately 1%, with slightly more in the nickel-rich case. Above 1% Cr addition, fine, coherent, α-chromium precipitates were found (10 to 25 nm). In many of the compositions, a bimodal precipitate distribution was noted with the small size being 10 to 25 nm and the large size being 250 nm. In addition to the chromium precipitates, chromium carbides ($Cr_{23}C_6$) were

40

found. Mechanical testing in compression at room temperature showed the stoichiometric NiAl to have the minimum yield strength and maximum ductility at 148 MPa and 12%, respectively, in the arc-melted and homogenized condition. Either deviation from the stoichiometric composition or any addition of chromium resulted in plastic strains less than 1% and failure by transgranular fracture. Substantial solid solution hardening was seen for chromium in aluminum- or nickel-rich compositions up to 1% (400 MPa for Ni:Al = 1, 543 for Ni:Al = 1.1). The hardening rate decreased for Cr additions over 1% with maximum hardening occurring when chromium was substituted for nickel. Dislocation analysis after deformation showed mainly <100> dislocations with some <110> in the extruded alloys which were said to be a result of <100> dislocation interactions. Only a few observations of <111> dislocations were made and not enough to accomplish significant deformation.

The precipitation of α-chromium in NiAl has been studies by Tian et al. using micro-hardness [101]. Tian confirmed some of the findings of Cotton with respect to precipitate size and nature. The majority of precipitation hardening was found to occur by small, coherent, α-chromium particles (200 nm). Although these particles are similar to those observed by Cotton et al., isothermal ageing was used by Tian et al. Ageing temperatures between 937 and 1173 K were employed. The strength was found to increase with ageing time to a defined peak, after which the strength decreased with further ageing. The peak in strength was found to correspond to the point just before dislocation looping was

41

seen (Orowan looping). In the majority of combinations of chromium concentration and temperature, Tian et al. also observed the most precipitation hardening from chromium being substituted for nickel.

Some of the most recent work on chromium addition to NiAl has been performed by Fischer et al. [59, 102, 103]. In this work, the evidence of <111> superlattice dislocations and an anti-phase boundary were detected using atom probe field ion microscopy. The suggestion was that chromium reduces the anti-phase boundary energy, allowing the <111> super-lattice dislocation to exist.

2.3.4 Processing

There are a number of processing methods used in NiAl research which can, at times, lead to difficulty in comparing results and findings. Almost all research done on NiAl has been with hot extruded material. The three common variations of this processing method are vacuum induction melting and extrusion [44, 48, 49, 51-53, 64, 70, 71, 75, 77, 99, 100, 104-106], powder compaction and extrusion [65, 69, 72], and arc-melting and extrusion [66, 78, 107]. Extrusion is a popular processing method because of the inherent difficulty in casting a material with little room temperature ductility. Thermal stresses can easily result in cracking of the alloy. The commonly reported tensile ductility of approximately 2% is only attainable in the extruded form [50]. Miracle suggests that this is likely due to the strong <111> texture that often results from extrusion. Another interesting point brought up is that material extruded from

42

powder is normally brittle. This may have something to do with the high interstitial content of nickel powders used [19].

One of the earlier studies on NiAl was by Grala [47], in which he employed vacuum induction melting. Although he was able to produce sound castings, no increase in ductility resulted. Arc-melting is a method that is used because of its low cost and high cleanliness. Westbrook [108] used arc-melting for studying temperature versus hardness effects. Zhou and Gou [79, 106] routinely use arc-melting to investigate various alloy additions to NiAl. The major drawback of arc-melting is that there is limited size of casting that can be created due to the copper hearth size. There are also extremely rapid cooling rates that require the specimen to be melted a number of times or homogenized at high temperature for long periods of time.

These different processing methods affect properties such as grain size, interstitial content, thermal vacancy concentration, dislocation density, and crystallographic texture. The proper parameters are often not reported in the literature, which makes confirmation or reproduction of results difficult, if not impossible.

2.4 Literature Review Summary

As outlined in the literature review above, the poor room temperature ductility of NiAl is the most limiting factor with respect to industrial application as a structural material. With a maximum reported tensile ductility of 4% [44] in the polycrystalline condition, and more routinely reported values being less than 2.5% [48, 49, 109], significant improvement is required. Although beneficial effects of micro-alloying with Fe, Mo, and Ga on single crystals have been seen [76], similar results on polycrystalline material have not been realized [97].

Chromium addition seems to hold the most promise for modification of the slip behaviour of NiAl. Although research by Law et al. [68] and Miracle et al. [98] showed the presence of <111> and <110> dislocations, exhaustive investigation by Cotton [51] showed no increase in ductility. Most recently, evidence of chromium atoms associated with the anti-phase boundary in a dissociated <111> dislocation has proven to be interesting [59].

The beneficial effect that ceria addition has on thermal sprayed coatings of NiAl is also interesting [84, 85]. The increase in coating adhesion and evidence of ductile wear in ceria-containing coatings provides motivation to study the effect of cerium/ceria on bulk NiAl.

Evidence of secondary slip vectors in NiAl from chromium addition, as well as the observed effects of ceria on NiAl coatings, has dictated the direction of this

44

research. Consequently, the approach taken was to investigate the combined

addition of chromium and cerium/ceria on the ductility of stoichiometric NiAl.

45

3.0 Experimental Procedure

This section will consist of a description of the material preparation procedure, thermal treatments, metallographic methods, mechanical testing equipment and procedure, and fractographic study techniques.

3.1 Material Preparation

Both the investment casting and arc-melting procedure are described, including post-casting chemical composition.

3.1.1 Investment Casting

Investment cast NiAl-based alloys were prepared in China at the Beijing Institute of Aeronautical Materials (BIAM) under the supervision of Dr. Chengbo Xiao. Master alloys were prepared with intentional addition of only nickel and aluminum by means of vacuum induction melting. Because of the mass of required alloy, two master batches had to be cast. Chemical analysis of the master alloys was performed at BIAM via inductively coupled plasma (ICP) analysis and the results are shown in Table 1.

Table 1: Master Alloy Chemical Composition

Element	Master Alloy 1		Master Alloy 2	
	(wt. %)	(at. %)	(wt. %)	(at. %)
Al	29.90	48.05	30.57	48.86
Fe	0.08	0.06	0.12	0.09
Si	<0.10	<0.154	<0.10	<0.154
Mn	<0.10	<0.079	<0.10	<0.079
C	0.018	0.065	0.010	0.036
S	0.001	0.001	0.001	0.001
P	<0.02	<0.028	<0.020	<0.028
Ni (balance)	69.78	51.56	69.08	50.80
Al/Ni fraction	n/a	0.93	n/a	0.96

46

The intent was to make a final product that possessed a 1:1 ratio of aluminum to nickel. Due to the high aluminum vapour pressure over molten NiAl, there is loss of aluminum during casting. An attempt was made to compensate for the predicted vaporization by addition of excess aluminum, but this was not successful. It can be seen in Table 1 that the fraction of aluminum to nickel was 0.93 for master alloy 1 and 0.96 for master alloy 2.

From the master alloys, eight different NiAl alloys were produced by addition combinations of Cr, Ce, and CeO_2. The final alloys were produced by alloying selected amounts of the aforementioned substances to the molten master alloy. The master alloy was melted under vacuum via induction heating. The alloying elements were then added to the melt at which point it was poured into pre-heated alumina crucibles. The crucibles were held at a temperature just below the freezing point (1640°C) of NiAl. The castings were then allowed to cool under an evacuated environment before the alumina crucibles were removed by sand blasting. Cast shapes included 10 mm diameter cylinders that were 200 mm long and 10 x 100 x 200 mm rectangular shapes as shown in Figure 7.
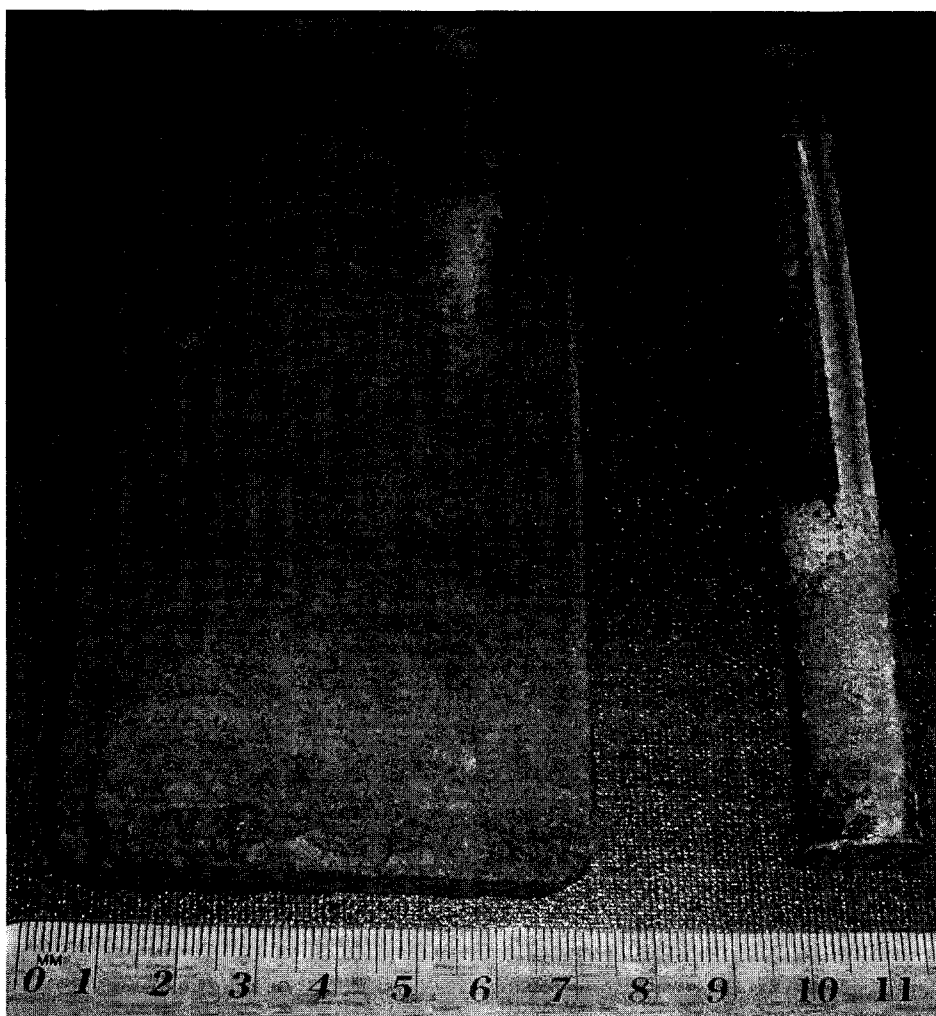
Figure 7: As-Cast Shapes

Chemical characterization of the cast alloys was performed again using ICP analysis. The results of the chemical analysis can be found in Table 2.

Table 2: Final Alloy Chemical Composition

Element	Alloy Chemical Analysis (converted to at%)							
	1	**2**	**3**	**4**	**5**	**6**	**7**	**8**
Al	47.49**	48.13	47.70**	49.32	48.56	48.09	48.53	48.31
Cr	0.00	2.25	0.00	0.00	0.00	2.35	0.00	2.15
Ce	0.00	0.02*	0.02	0.04	0.05	0.02	0.11*	<2ppm*
Ni (balance)	52.51	49.59	52.28	50.64	51.39	49.54	51.36	49.52
Al/Ni Fraction	0.90	0.97	0.91	0.97	0.95	0.97	0.94	0.98

* Indicates the addition of sub 1 μm sized CeO_2 instead of metallic Ce.
**Indicates that composition is an average of two analyses.

48

3.1.2 Arc-Melting

Due to excessive cracking and the presence of casting defects, it was decided that the investment cast material would have to be re-processed in order to continue investigation. To reduce cost and complexity, only alloys 1, 2, 3, 6, and 8 were re-melted.

The investment cast material was re-melted using an arc-melter as shown in Figure 8 (Materials Research Corporation, Series V-4, Orangeburg, New York). The process was conducted under an evacuated environment with a small amount of argon for ionization. To ensure no oxygen contamination during melting, the chamber was evacuated and then filled with argon three times before melting. In addition, a small piece of molybdenum was used as an "oxygen getter". Once the arc was struck, it was concentrated on the molybdenum in order to react all of the available oxygen in the chamber. Since the copper base is water-cooled, the material solidifies almost immediately after the arc is removed. This rapid solidification helped to minimize the loss of aluminum during melting. An example of the shape of the re-melted ingots can be seen in Figure 9, while a cross-section of an arc-melted ingot is shown in Figure 10. The chemical composition of the re-melted alloys is shown in Table 3. Composition was determined using ICP spectroscopy.

Reproduced with permission of the copyright owner. Further reproduction prohibited without permission.

Figure 8: Electric Arc-Melter

Table 3: Re-Melted Alloy Chemical Composition

Element	Alloy Chemical Analysis (converted to at%)				
	1	**2**	**3**	**6**	**8**
Al	49.80	48.68	49.64	49.67	49.37
Cr	0.00	2.04	0.00	2.11	2.09
Ce*	0.00	0.02	0.02	0.02	<2ppm
Ni	50.20	49.25	50.33	48.19	48.54
Al/Ni Fraction	0.99	0.99	0.99	1.03	1.02

* Ce composition from original investment casting assay.

50
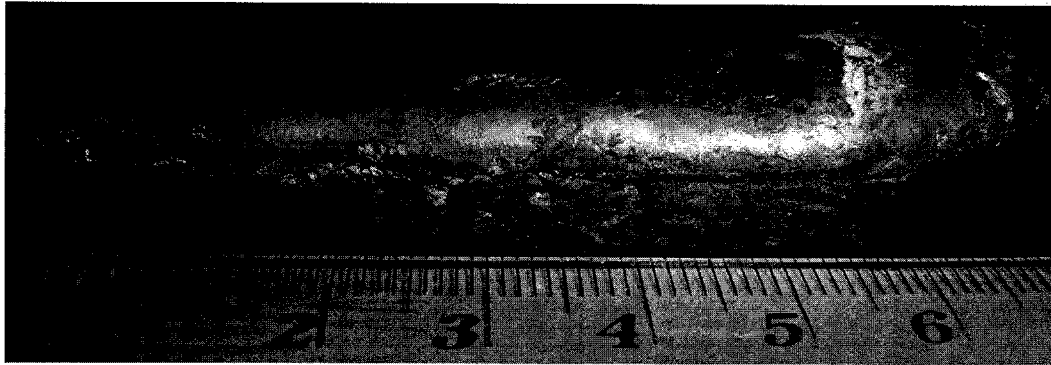
Figure 9: Re-Melted Ingot
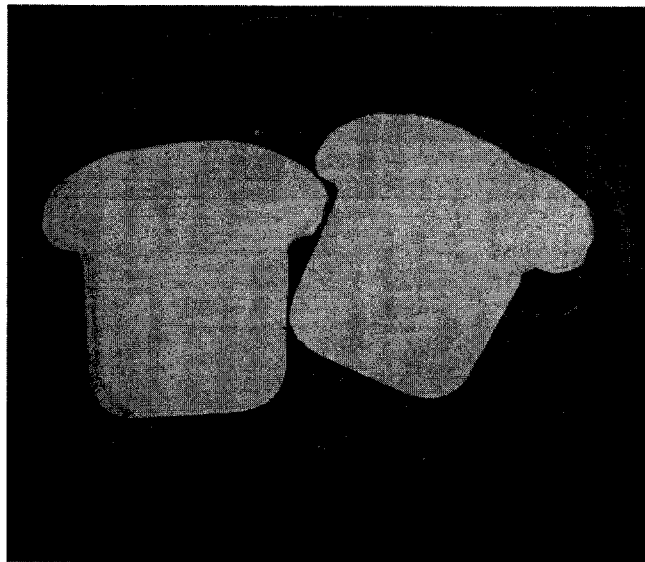
Figure 10: Cross Section of Re-Melted Ingot, in 1.25-inch Sample Puck

3.2 Thermal Treatment

There were two types of thermal treatment performed: homogenization and hot iso-static pressing (HIPing) treatments. The HIPing treatment was only performed on the investment cast material.

51

3.2.1 Homogenization

It was decided that a high temperature homogenization treatment would be performed in order to ensure a homogenous alloy. The homogenization treatment for the investment cast material consisted of a 1-hour ramp up to 750°C, with a 6-hour hold at that temperature, followed by a 0.5-hour ramp up to 1100°C, where temperature was maintained for 24 hours followed by furnace cooling (~4 hours). For the re-melted material, three different cooling rates were used at the end of the same homogenization treatment. In addition to the furnace cooling, forced air cooling as well as slow cooling (24 hours) were used. Figure 11 shows the time versus temperature plots of the treatments with the different cooling rates. Homogenization was performed under an air atmosphere. Although an inert atmosphere would have been preferable, such a furnace was not available. The homogenization temperature of 1100°C was selected based on the insufficient oxide stability at higher temperatures. The 750°C stage of the treatment was set below the melting point of metallic cerium (795°C) to allow for maximum solubility of the metal in the NiAl matrix.

52
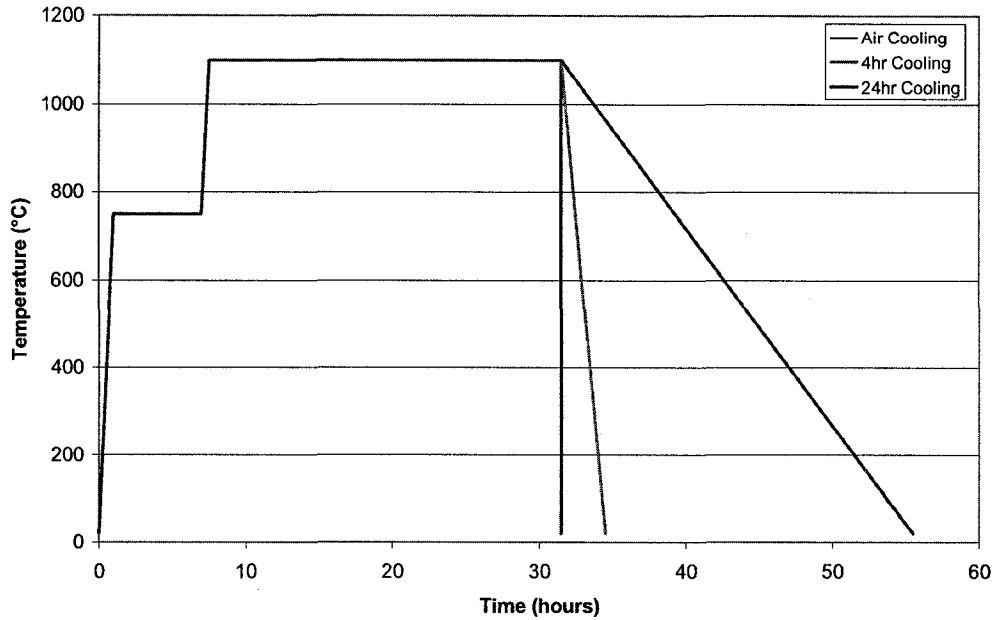
Figure 11: Homogenization Time versus Temperature Curves

3.2.2 Hot Iso-Static Pressing

The investment cast material was sent out for hot iso-static Pressing (HIPing) at

Pressure Technology Inc. in Warminster, Pennsylvania. The HIPing process was

performed at 150 MPa and consisted of a ramp up to 750°C, a hold similar to

that in the homogenization treatment, followed by a ramp up to 1250°C and a

hold for 3 hours followed by a furnace cool. The HIPing process and maximum

temperature was selected as it is commonly used to reduce porosity in nickel-

based superalloys.

3.3 Metallography

All metallographic samples were prepared using a diamond precision saw for

sectioning. Samples were mounted in Bakelite according to standard methods,

53

with the temperature kept below 150°C. Grinding consisted of 240, 320, 400, and 600 grit stages using either a manual polishing/grinding wheel or an automatic polisher. Final polish steps included 6-micron diamond suspension followed by 0.05-micron colloidal silica suspension. Etching was performed using a 3:2:1 mixture of lactic, nitric, and hydrochloric acids.

Microstructural characterization was performed using both a Hitachi S-2700 Scanning Electron Microscope Link eXL EDS System (SEM) and a JEOL 8900 microprobe (EMP) equipped with five wavelength dispersive spectrometers (WDS). For WDS analysis, 20 kV accelerating voltages and 1.04×10^{-7} amp probe currents were utilized. An Olympus PME 2 optical microscope was also utilized.

3.4 Mechanical Testing

Mechanical testing consisted of compression and hardness testing.

3.4.1 Hardness Testing

A Shimatzu micro-hardness indenter was used for hardness testing of all alloys. The indenter load was 1000g with a dwell time of 15 seconds.

3.4.2 Compression Testing

Compression specimens were prepared by means of electrical discharge machining (EDM). EDM was used in an attempt to avoid the introduction of cracks that might be expected from mechanical machining. Specimens were cut

to a size of 4 x 4 x 6 mm, after which all sides were sanded with 600-grit silicon carbide paper to remove the surface area affected by the EDM process. Figure 12 shows an image of a compression specimen after EDM cutting and grinding.

Testing was conducted under a constant cross-head speed of 0.360 mm/minute. Considering the nominal specimen length of 6 mm, this cross-head speed equated to a strain rate of ~1 x $10^{-3}s^{-1}$. A ball seat lower compression platen was used in order to ensure uniform pressure on the specimen. Figure 13 shows a schematic of the compression testing set-up.
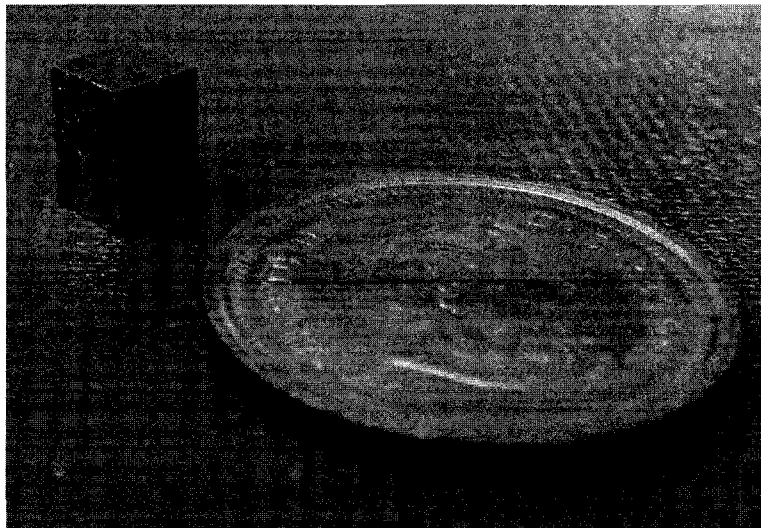
Figure 12: Compression Specimen after EDM Cutting and Grinding (with penny for size reference)
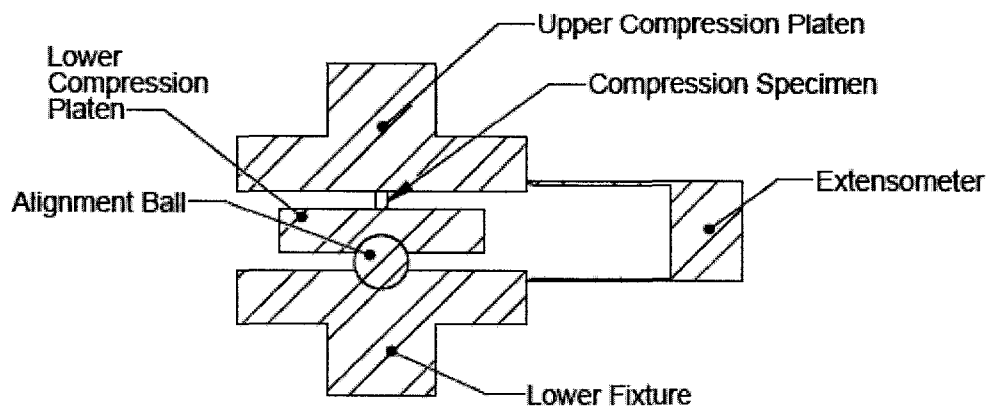
Figure 13: Compression Testing Set-Up

3.5 Fractographic Analysis

Fractographic analysis was conducted on the re-melted material. After failure of the specimens in compression, the fracture surfaces were examined using the SEM described previously to determine the fracture mode. Due to the varying fracture modes seen and the limited material left after compressive failure, only a few samples could be examined. Since it was not possible to properly examine the specimens after compressive failure, simulated failures were used.

In order to verify the fracture mode of the different alloys, samples were intentionally fractured and the surfaces were examined. This was done with each of the three cooling rate specimens for each of the alloys. The fracturing method is illustrated in Figure 14. Fracture surfaces were examined via an SEM where a determination of the fracture mode (intergranular, transgranular, or mixed) was made.

56
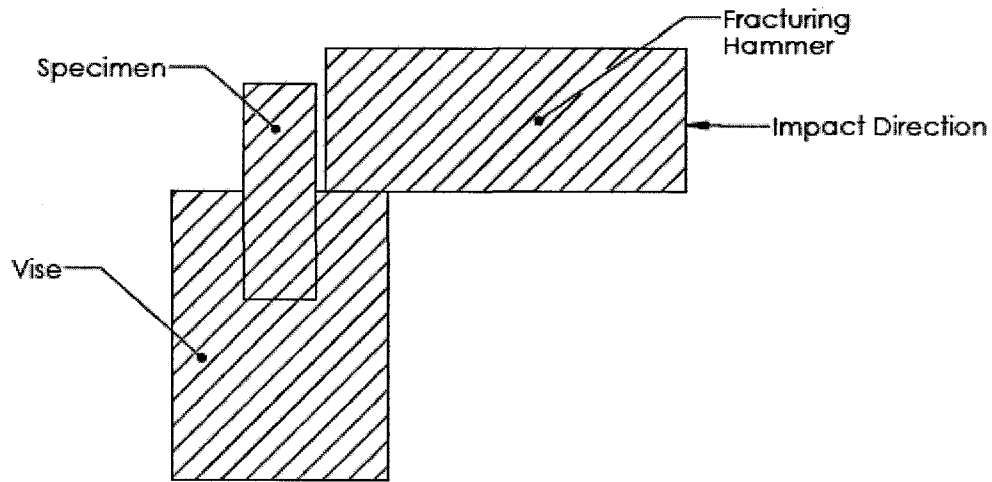
Figure 14: Fracturing Set-Up

In another attempt to verify the fracture mode of the different alloys, samples were compressed to loads just below critical load. After specimens were removed from the testing machine, they were mounted in Bakelite and ground until half of the sample was removed. After grinding, the specimen surface was polished and the fracture paths were viewed using an optical and scanning electron microscopy.

4.0 Results and Discussion: Investment Cast Material

Results and discussion from the investment cast material will consist of metallography, hardness and compression testing, and a final summary.

4.1 Metallography

Upon examination of all eight alloys, five were selected for the full range of characterization and testing (Table 4).

Table 4: Selected Alloys

Alloy	Al/Ni Fraction	at.% Cr	at.% Ce
1	0.90		
2	0.97	2.25	0.02 (CeO_2)
3	0.91		0.02
6	0.97	2.35	0.02
8	0.98	2.15	<2 ppm (CeO_2)

Alloy 1 was selected as a control because it had no intentional additions other than nickel and aluminum. Alloy 2 was selected due to the addition of both ceria and chromium. Alloys 3, 4, and 5 all contained metallic cerium additions, but alloy 3 had similar cerium content to alloys 2, 6, and 8; therefore, alloy 3 was selected, while alloys 4 and 5 were not. Alloy 6 was also selected because it contained both metallic cerium and chromium. Alloy 7 was omitted because of evidence of heavy oxidation on the grain boundaries. Finally, alloy 8 was selected as it had similar chromium content to alloys 2 and 6, but with less cerium.

58

Results of the metallographic study on the selected five homogenized alloys generally showed an equiaxed grain structure, with grain sizes varying between approximately 150 and 550 microns for alloys 6 and 1, respectively. Figure 15 shows the grain structure of the five selected alloys in the homogenized condition. The differences in grain size could be a result of many variables including melt temperature, alumina mould temperature, grain pinning action by alloy elements, and proximity of presented area from the mould interface. An attempt was made to present areas of equal distance from the mould interface but no guarantee of this can be made. Thus, it is difficult to make any substantive statements about the variation in grain size.

59
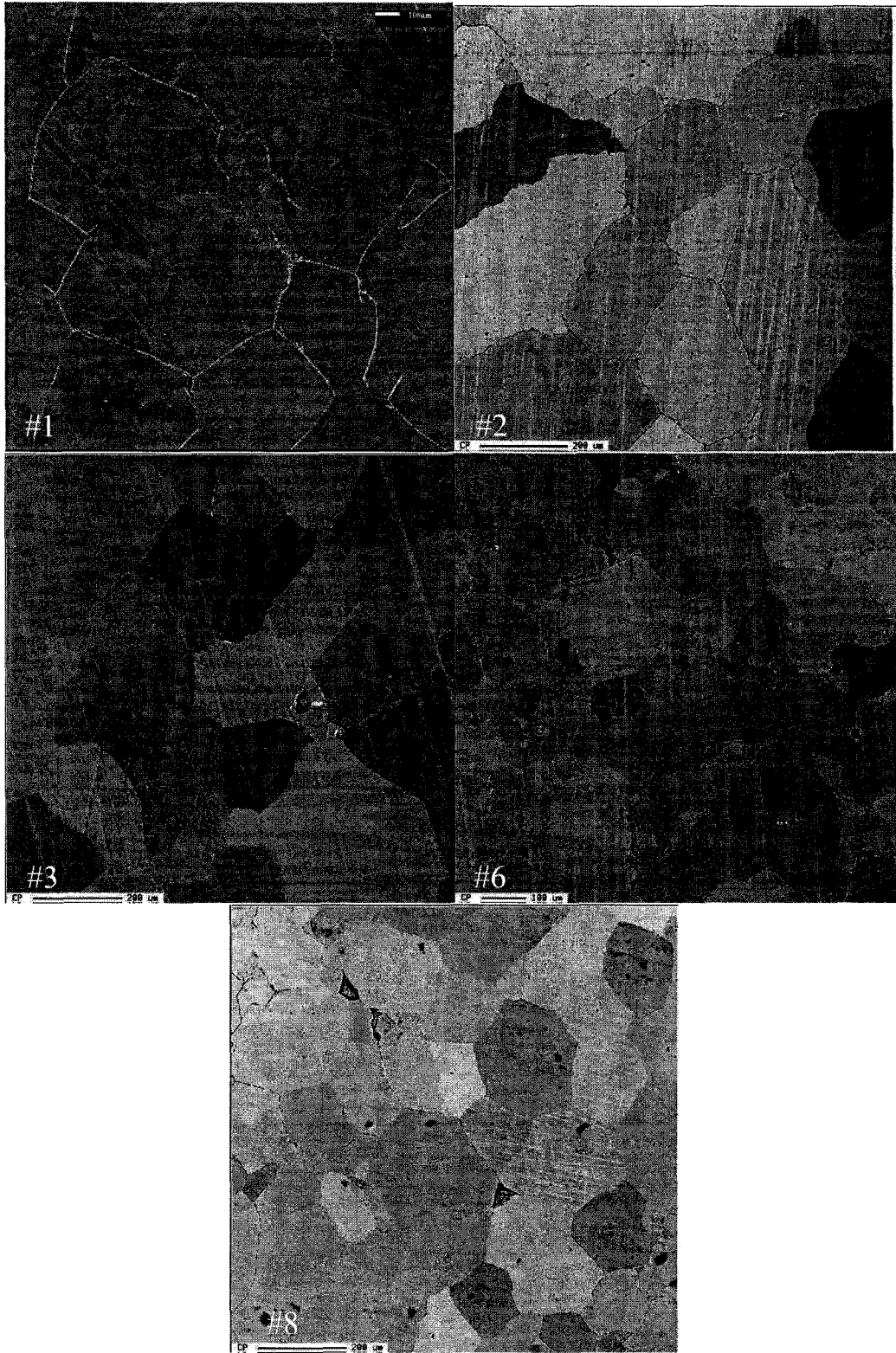
Figure 15: SEM Images of Homogenized Alloy Grain Structures: Alloy 1 (NiAl); Alloy 2
(NiAl+CeO$_2$+Cr); Alloy 3 (NiAl+Ce); Alloy 6 (NiAl+Ce+Cr); and Alloy 8 (NiAl+ CeO$_2$+Cr)
(SE)

60

Upon examination at higher magnification, the commercially pure NiAl (alloy 1) showed a single phase structure. This was to be expected as there were no tertiary or quaternary alloy additions. At 7000X magnification, alloys 2, 6, and 8, all containing chromium and cerium, showed very small precipitates inside the grains (Figure 16). These precipitates were of the 200-nm size and thus were too small to analyze for elemental presence. Much larger precipitates were found in the grain boundaries of alloys 2, 6, and 8. These precipitates were around 1 micron in size and were found via EDX to be chromium-containing (Figure 17). It is quite possible that the larger grain boundary precipitates are inter-dendritic chromium that did not fully dissolve during the homogenization treatment. An interesting marble-like pattern was found under high magnifications in all of the alloys. No similar indication of a marbled pattern could be found in the literature and it is likely a result of etching. Figure 16 shows both the precipitates and marbling pattern in alloy 2. Although the chemistry of the 200-nm precipitates cannot be definitively determined with the utilized methods, it can be assumed that they are mainly chromium-containing. This assumption is further supported by Tian et al. and Miracle et al. [50, 101] who found chromium precipitates of 600 and 200 nm with additions of 5 and 6 at.% Cr, respectively. In both of these cases, the precipitates were found to be α-chromium via TEM.

61
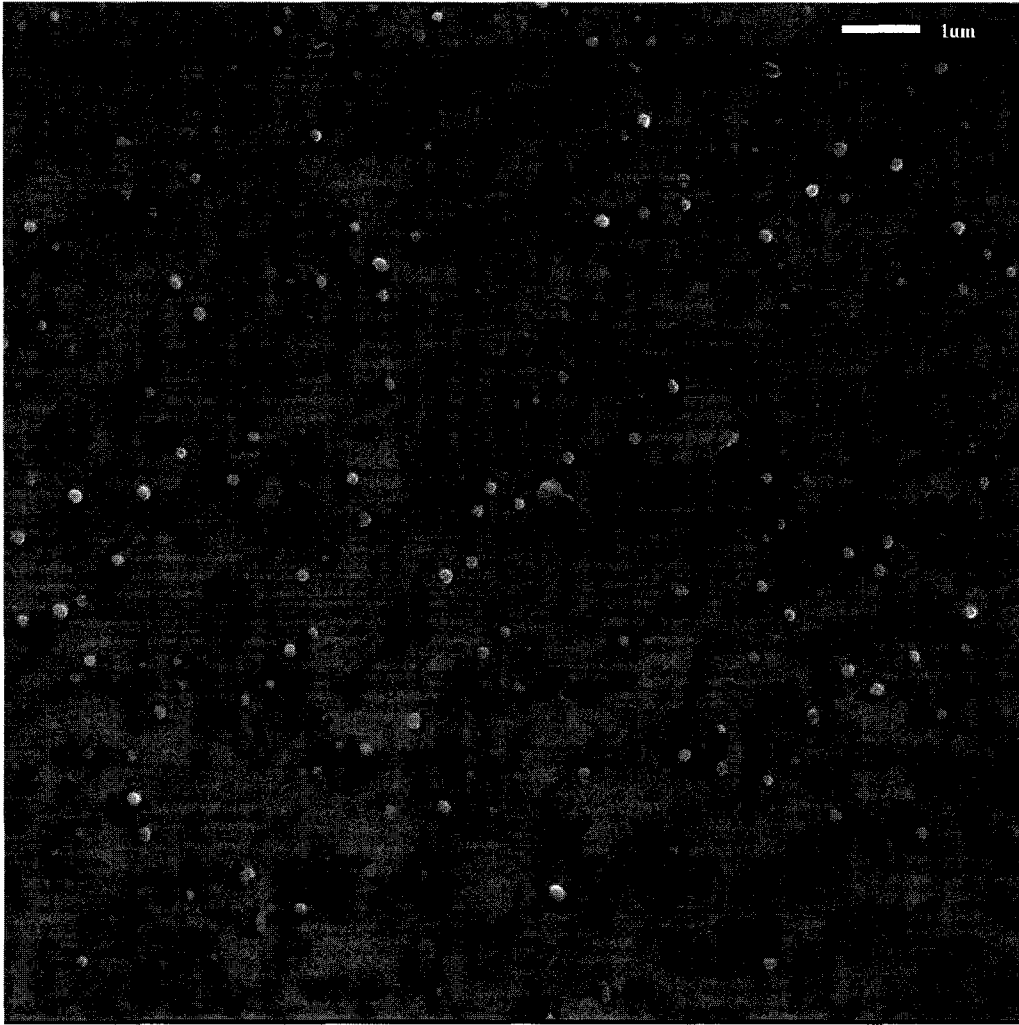
Figure 16: SEM Image of Alloy 2 (NiAl+CeO$_2$+Cr) Showing Precipitates and Marbling Pattern (SE)

62
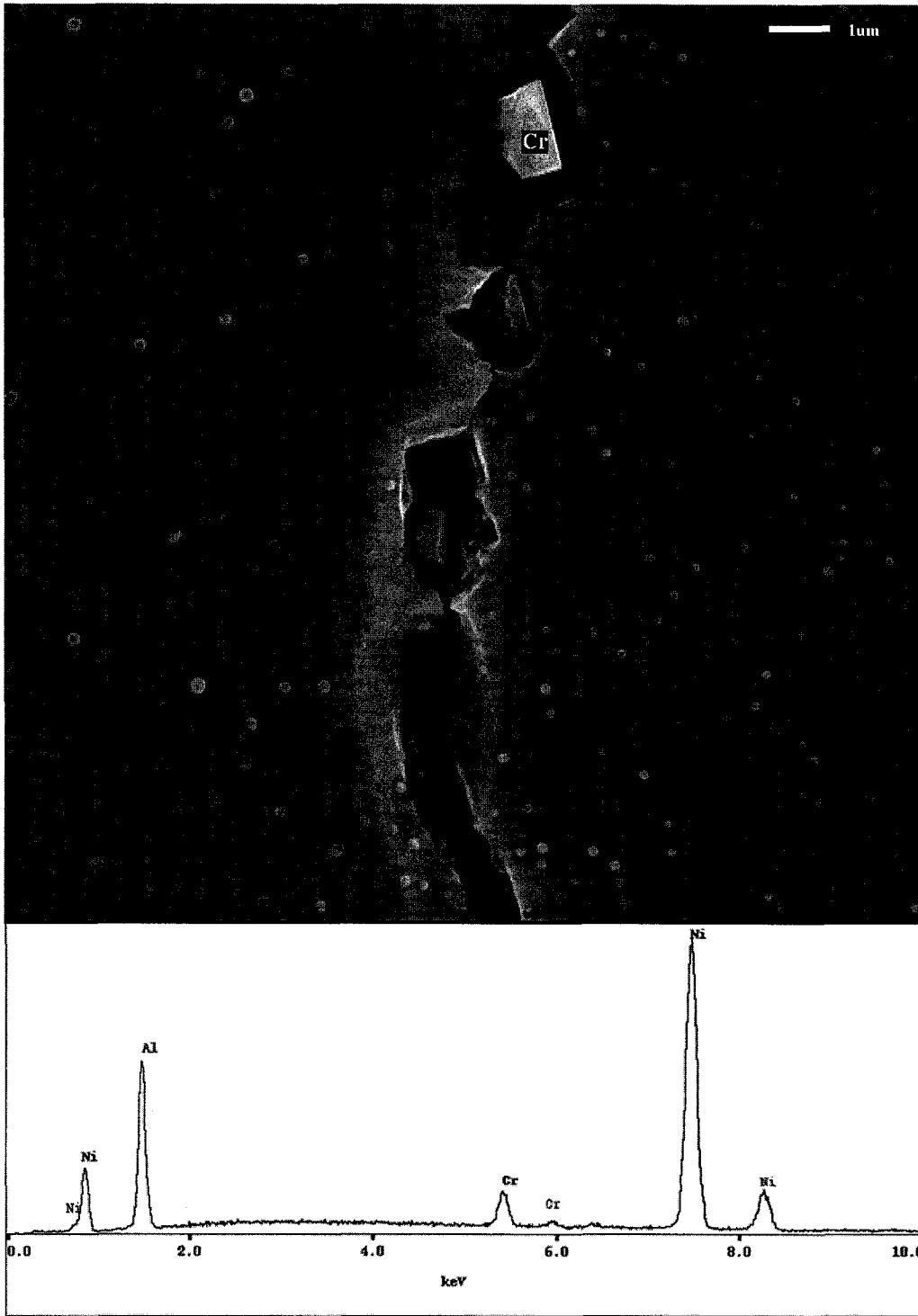
Figure 17: SEM Image of Chromium Indication on Grain Boundary of Alloy 6 (NiAl + Ce + Cr) with EDX Spectra (SE)

63

When looking at Figure 18, it can be seen that there are also larger rod-shaped precipitates present. These precipitates were found by EDX to contain high chromium content. Because of the small size, it is impossible to determine whether the nickel and aluminum present are from the precipitate or the matrix. Similar precipitates were found by Fischer et al. [103] in a study with 2 at.% Cr addition. Through TEM analysis, Fischer et al. determined that these elongated precipitates were Cr_7C_3. Although the elongated precipitates seen here cannot be positively identified, they are similar in shape and size to those mentioned above.
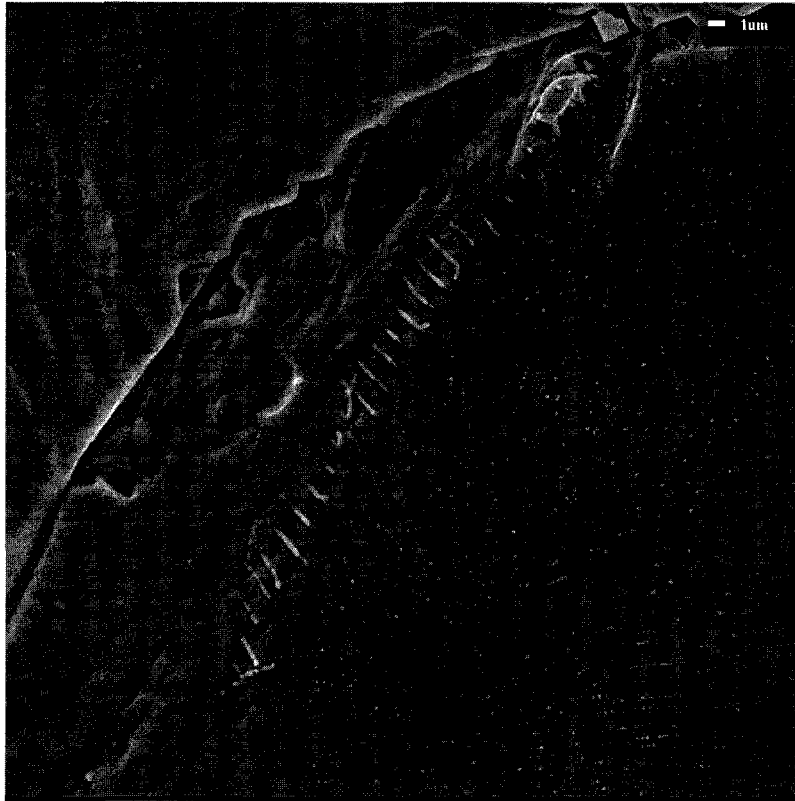
Figure 18: SEM Image of Elongated Precipitates in Alloy 6 (NiAl+Ce+Cr) (SE)

Metallic cerium additions were made to alloys 3 and 6. The evidence of this was seen mainly on the grain boundaries in alloy 3, while very little cerium could be

64

found in alloy 6. Figures 19 and 20 show WDS maps indicating cerium in alloys

3 and 6, respectively. No significant amounts of cerium indications could be

found in alloys 2 and 8.

Figure 19: WDS Map of Alloy 3 (NiAl + Ce) Indicating Cerium

65
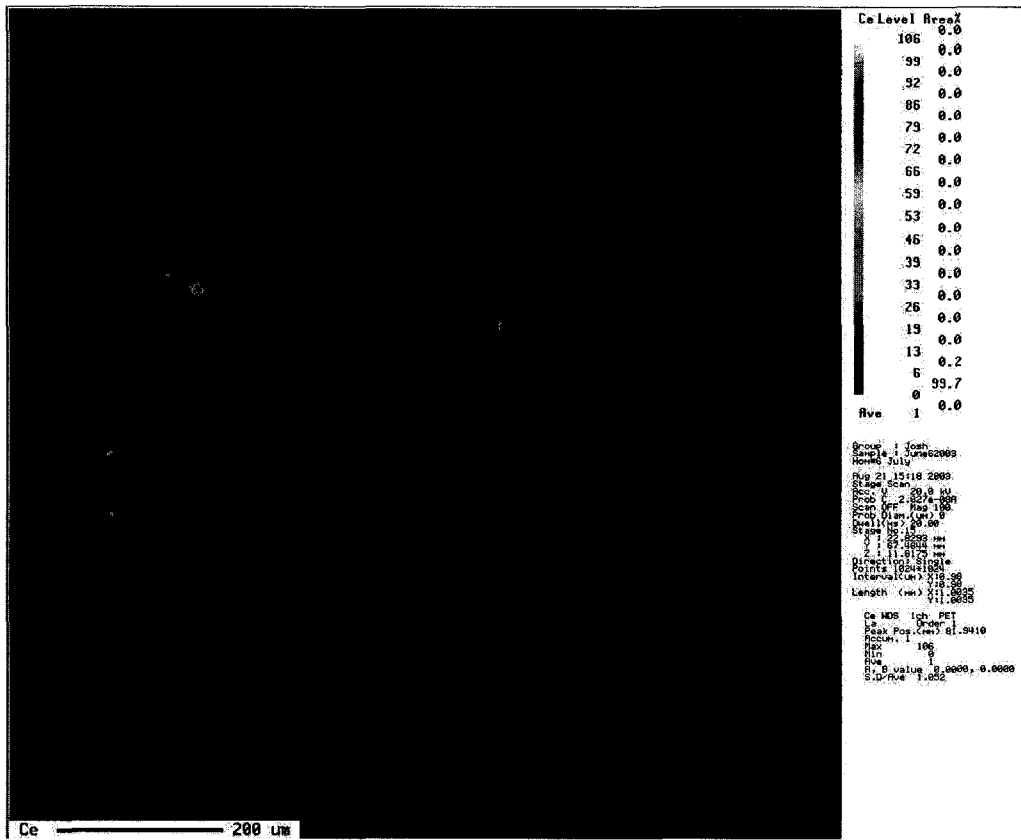
Figure 20: WDS Map of Alloy 6 (NiAl + Ce + Cr) Indicating Cerium

66

4.2 Hardness and Compression Testing

Hardness testing results on the homogenized alloys are shown in Figure 21.
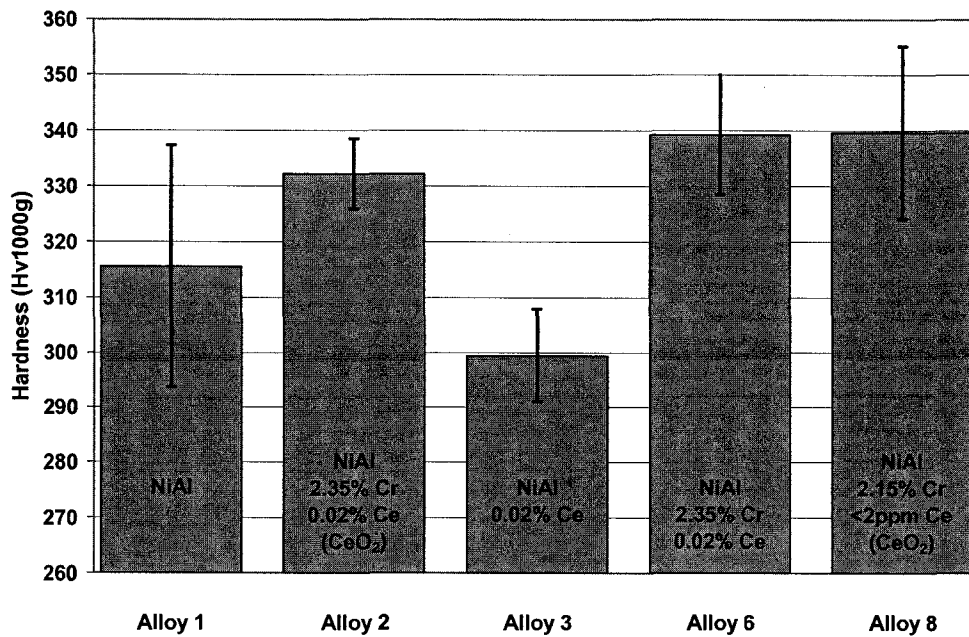
Figure 21: Homogenized Hardness

The hardness of the non-alloyed material (alloy 1) agrees reasonably well with some other reported studies. Baker and Nagpal [104] obtained a hardness value of 320 for the stoichiometric composition after furnace cooling, while Tian et al. [101] and Cotton [51] found hardness values of 260 and 270, respectively, for the same composition. The hardness of alloy 3 appears to be lower than that of alloy 1. No obvious hardening or softening effect would be expected from the addition of cerium due to its lack of solubility and its existence mainly in the grain boundaries, which were avoided during hardness testing. As anticipated, the chromium-containing alloys are harder than the ones without. In solid solution, it is generally agreed that chromium occupies the aluminum sub-lattice for the nickel-rich and stoichiometric conditions [60, 110, 111] and, thus, results

67

in the generation of nickel vacancies to conserve order. Up to around 1 at.%, chromium will be in solid solution, and with greater chromium content, the formation of small coherent precipitates will occur [101-103, 112]. In the case of alloys 2, 6, and 8, both solid solution and precipitation hardening should contribute to the hardness and strength as they possess greater than 3 at.% Cr. Tian et al. and Cotton [51, 101] reported hardness values of 350 and 340, respectively, when chromium was substituted for aluminum at a concentration of 2%.

Characteristic compression testing results of the homogenized material as well as the homogenized and HIPed material are shown in Figures 22 and 23.
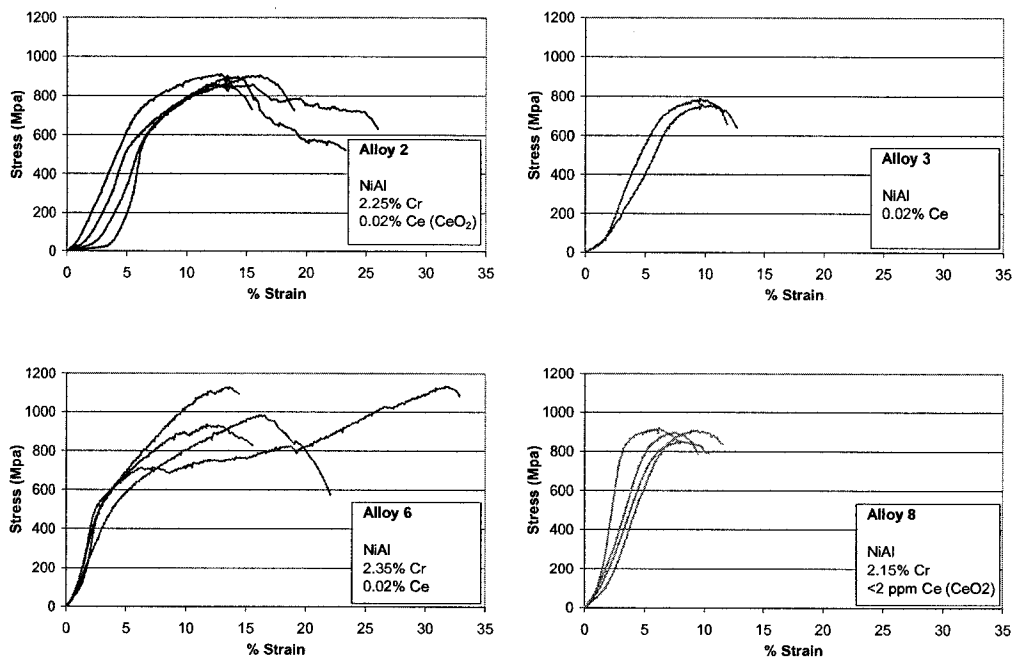
Figure 22: Un-HIPed Compression Testing Results

68
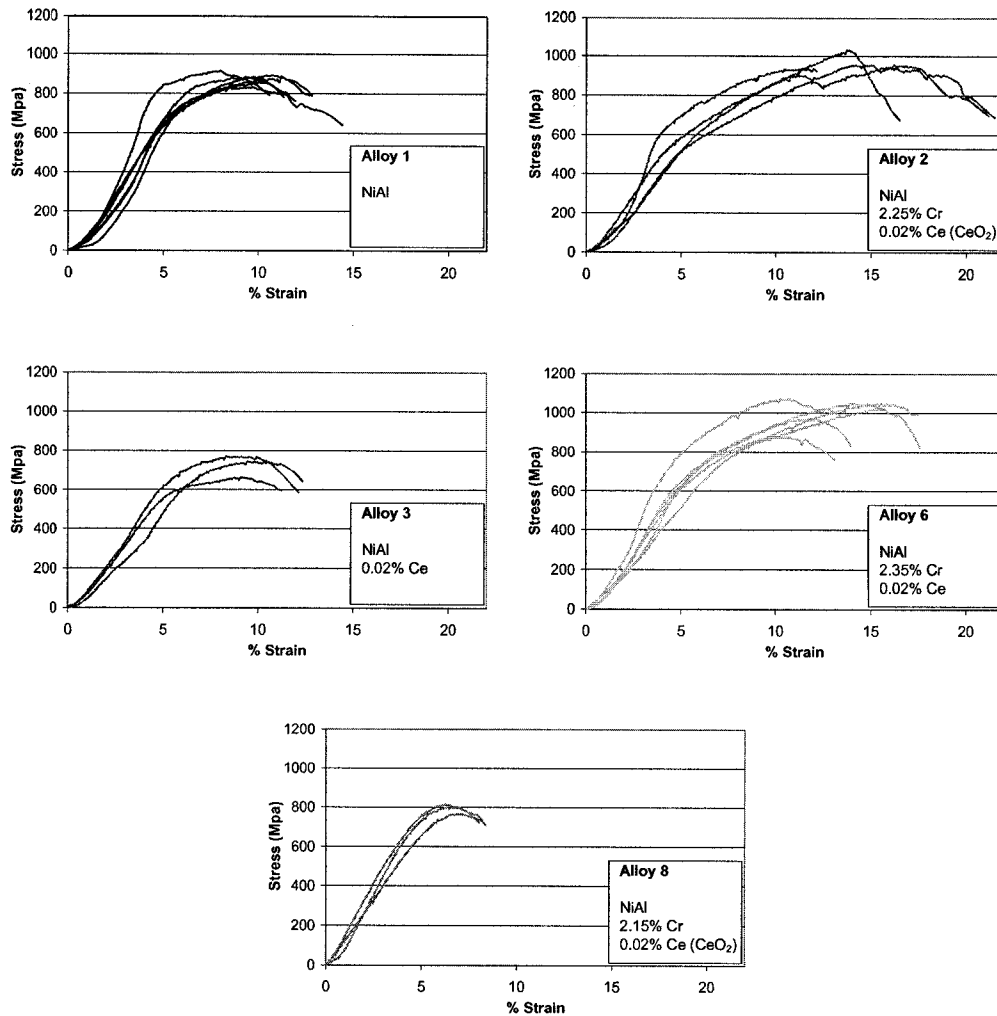
Figure 23: HIPed Compression Testing Results

Looking at Figures 22 and 23, it is clear that the elastic slopes of the different alloys are not consistent. The noticeable non-linearity of the initial portion of the curves, from about 0 to 150 MPa, is a result of the self-aligning compression platen. After this point, it would be expected that the elastic slope of the curves would be close to the theoretical value of 193 GPa. In fact, the stiffness values are nearly an order of magnitude lower than expected. The high, apparent compliance of the samples is in part due to the compression test set-up. The 2-

69

inch extensometer used to measure displacement spanned a number of interfaces as well as the alignment bearing. In order to obtain the most accurate measure of post-yield deformation, strain was calculated as the extensometer displacement over the specimen length. A result of this is an inaccurate strain reading in the initial loading regions where the interfaces are settling. By the time yield has occurred, all of these interfaces would be tight. Variations in stiffness can also be accounted for by continued rotation of the platen during testing. Depending on the direction of rotation with respect to the location of the extensometer, the stiffness can be increased or decreased. Another possible contributor to a decreased elastic stiffness is a reduction in the load-carrying area due to cracking.

Looking at portions of the compression curves at higher magnification (Figure 24) variations in both the load (vertical) and displacement (horizontal) directions can be seen. This roughness could not be the result of electrical noise as it deviates from the curve in directions not purely horizontal or vertical. The behaviour seen in Figure 24 would most likely be due to crack growth during loading. If small cracks were to form or grow, it would result in both load drops and displacement jumps. After one of these rapid events, the self-aligning fixture could rotate bringing the path of the curve back on its original course. The same serrated behaviour is seen in all compression curves over the entire loading range. If cracking were to occur early in the test during the fixture alignment, it

70

is possible that some decreased portion of the material would experience the compressive load for the remainder of the test.
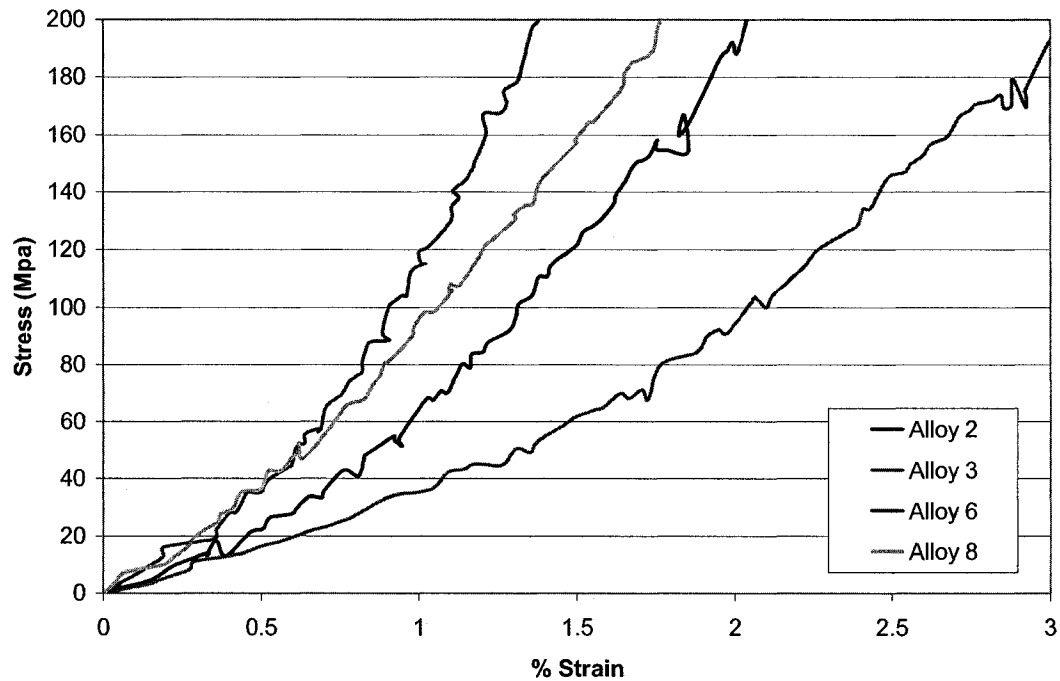
Figure 24: Un-HIPed Compression Tests at Close Range.

Due to the suspicion of crack growth and lack of consistent linearity in the compression curves, yield strength determination is not possible. However, visual examination of the general curve shapes shows a significant difference between alloys 2 and 6 and the rest of the compositions as far as peak strength is concerned. Alloy 2 has cerium oxide and chromium additions, while alloy 6 has metallic cerium and chromium. Looking at the peak stress summary in Figure 25, alloys 2 and 6 have higher maximum stress than the others in the HIPed condition. In the un-HIPed condition, the strength of alloy 2 is similar to alloys 1 and 8, while alloy 6 is still significantly higher.

71

A comparison of the hardness testing results with the peak compression behaviour is shown in Figure 26. Hardness testing involves penetration of a pyramid-shaped diamond indenter into the surface of the material. This indentation requires permanent deformation and is therefore relative to a point in between the yield and tensile peak of the stress versus strain curve. Considering this, a relation between the hardness and peak compressive strength might be expected. Looking at Figure 26, a linear trend can be envisioned in alloys 1, 3, and 6. Alloys 2 and 8 deviate significantly from this hypothetical trend. What must be considered is that no hardness indents generated cracks, while it is possible that compression testing results include fracture propagation.

Another key observation is that alloys 2 and 6 appear to have significantly higher ductility prior to loss of load-bearing capacity. Since the deformation after peak stress most likely includes significant crack growth, peak strain will be used for a ductility comparison. Figures 27 and 28 show the peak stress versus peak strain results from the un-HIPed and HIPed compression tests, while Figures 29 and 30 show the peak strain comparisons. Alloy 1 (NiAl) has a maximum peak strain of approximately 11%, whereas alloys 2 (NiAl + CeO_2 + Cr) and 6 (NiAl + Ce + Cr) show strains as high as 16 and 15%, respectively, for the HIPed condition. The un-HIPed compression testing results for alloy 6 (Figure 22) contain a very unusual behaviour. Since the curve shape is significantly different from the others and the strain to failure is nearly double, this result is not included in the peak strain analysis. After omitting the abnormal test result, the peak strains of

72

alloys 2 and 6 in the un-HIPed conditions are quite similar to those of the HIPed

alloys. What is surprising is that alloy 8 does not display similar compressive

behaviour. Maximum peak strains of 9 and 7% were obtained from the un-HIPed

and HIPed alloys, respectively. Looking back at Table 2, the aluminum-to-nickel

ratios of alloys 2, 6, and 8 are virtually identical. With no obvious difference in

composition, the drastically different compressive behaviour is noteworthy.
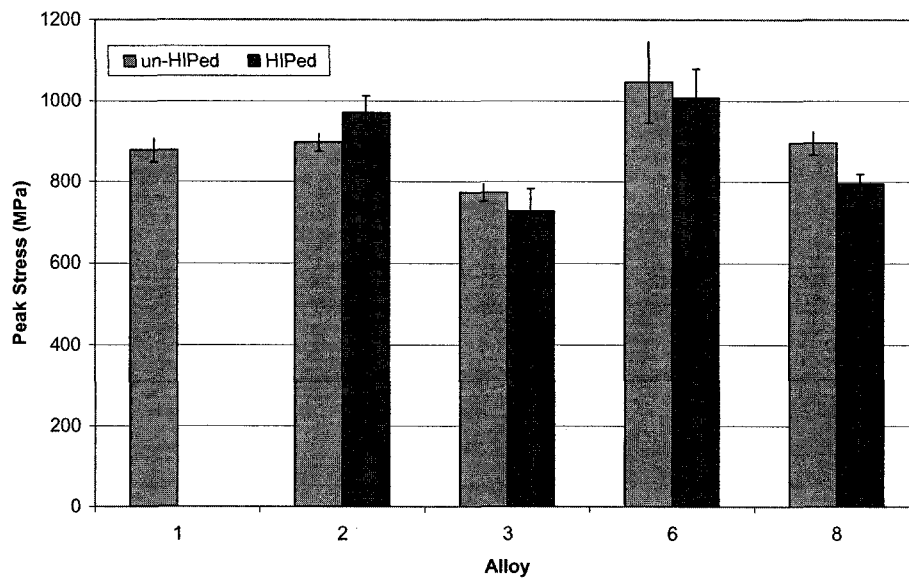
Figure 25: Compression Testing Peak Stress Summary

73
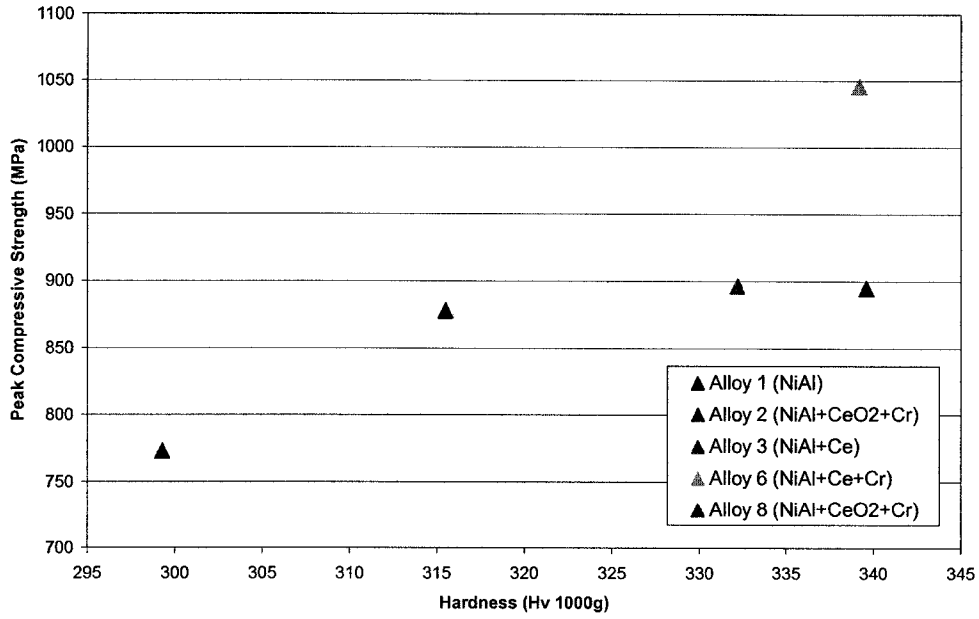
Figure 26: Hardness versus Peak Compressive Strength
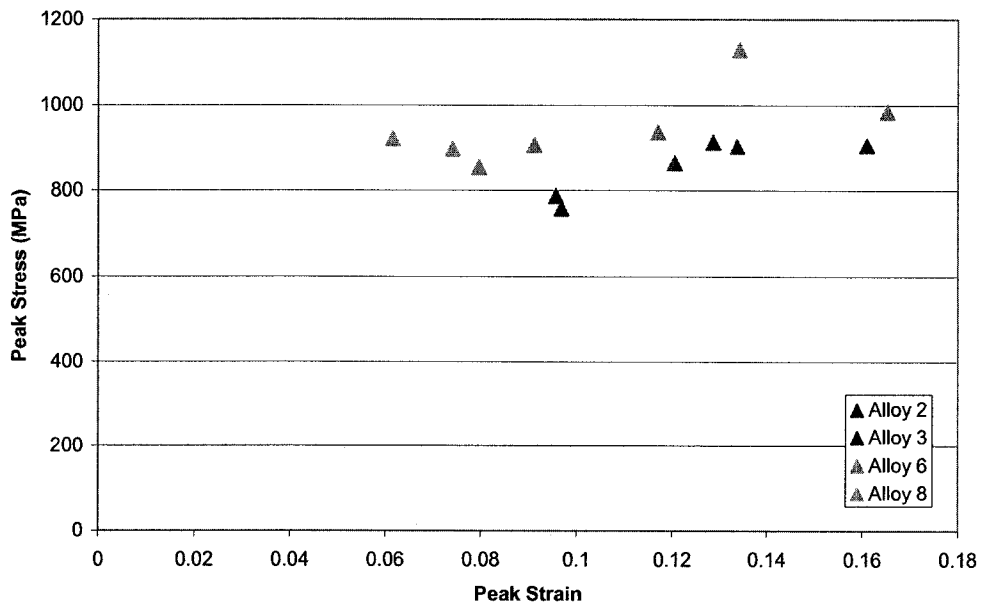
Figure 27: Un-HIPed Peak Stress versus Peak Strain

74
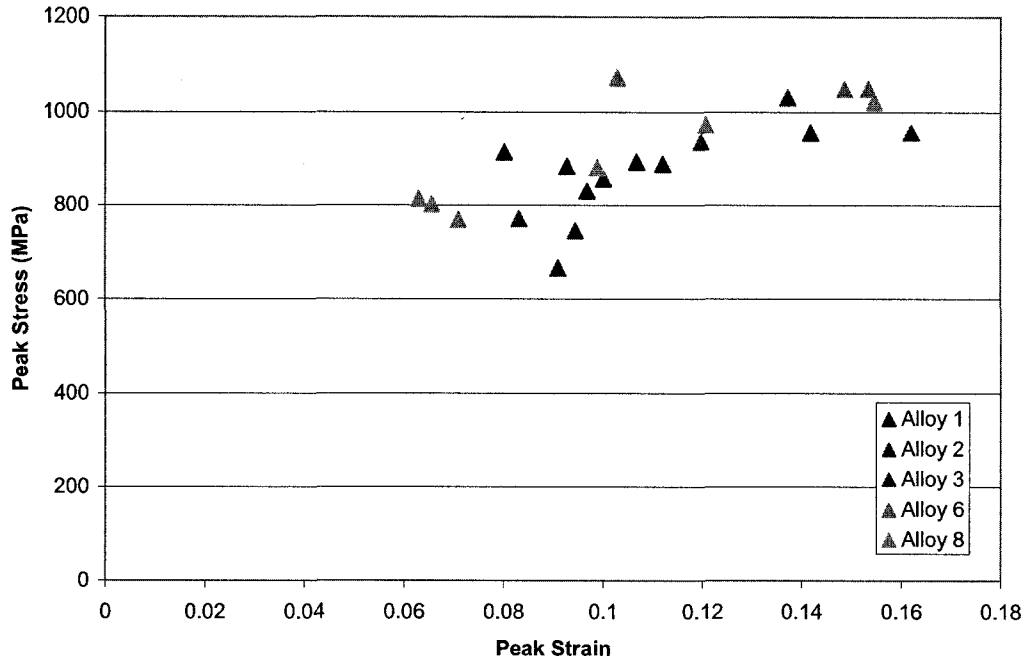
Figure 28: HIPed Peak Stress versus Peak Strain
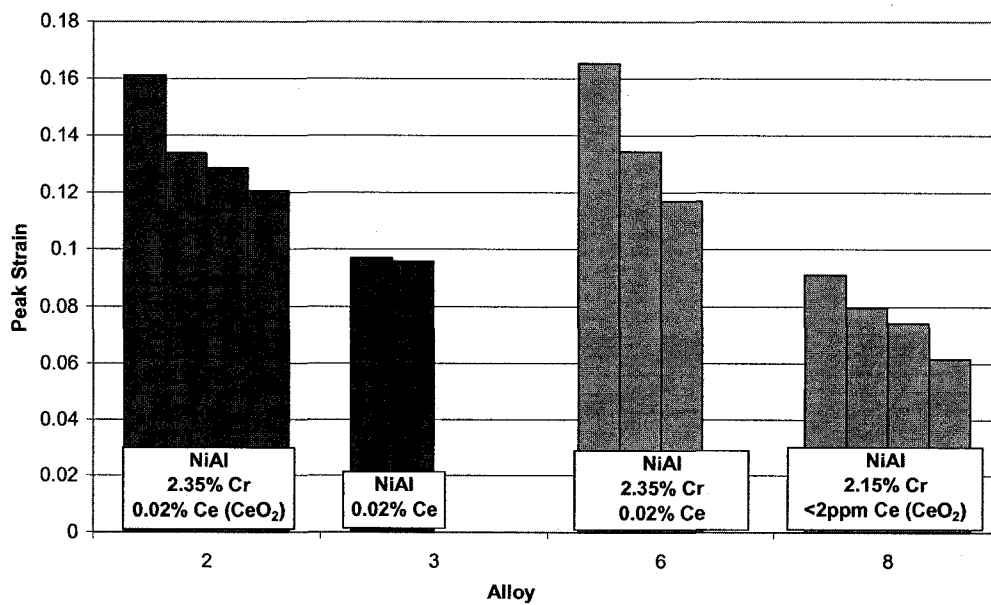
Figure 29: Un-HIPed Peak Strain Comparison

75
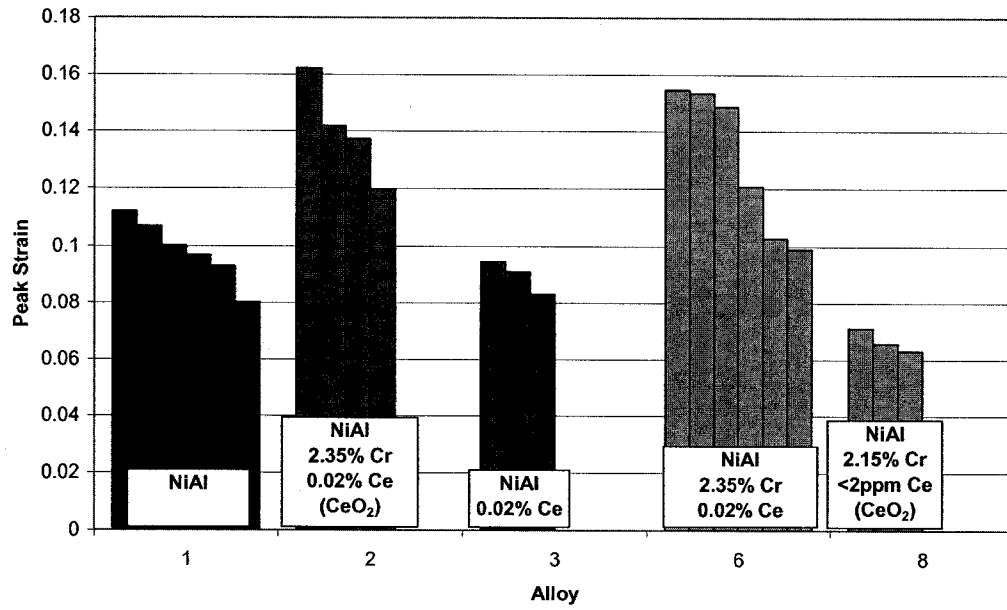
Figure 30: HIPed Peak Strain Comparison

76

4.3 Summary

The results of metallography and mechanical testing have yielded some interesting results that may indicate a combined effect of chromium and cerium on NiAl. The compressive curves of alloys 2 and 6 show substantially more deformation prior to failure than is seen in alloy 8. The only clear difference between alloy 8 and alloys 2 and 6 is that the former had no detectable cerium (<2 ppm) upon chemical analysis. Further investigation of this phenomenon is necessary, with specific attention being paid to the fracture mode of the alloys during compression testing.

Unfortunately, the investment cast material contained substantial cracking from the thermal stresses of casting and was not suitable for continued mechanical testing. In order to continue with the investigation of these alloys, the material was re-melted via arc-melting as described in Section 3.1.2. This method of melting is rapid and therefore should conserve the chemical composition of the alloys.

77

5.0 Results and Discussion: Arc-Melted Material

In general, the attempt to re-process the investment cast material was successful. It was possible to produce small castings without cracking. However, there were significant casting defects from shrinkage of the molten metal upon solidification. Figure 31 shows casting defects found intersecting fracture surfaces in both the investment cast and arc-melted material. The investment cast image shows a tunnel type pore while the re-melted material exhibits a lack of grain boundary fusion. The residual stresses in the ingots after arc-melting was extremely high and impact, such as dropping on the floor, resulted in cracking. After homogenization, the material was much tougher and more durable.

Figure 31: SEM images of a Tunnel-type Pore in the Investment cast material (left), and Lack of Grain Boundary Fusion in the Arc-Melted Material (right) (SE)

5.1 Metallography

Results of the metallographic investigation will be presented first, followed by a separate discussion of these results.

5.1.1 Metallography Results

The resultant grain structures produced from arc-melting the original alloys can be seen in Figure 32. There is a large difference in grain structure and size. Alloys 2 and 3 mainly consist of equiaxed grains, while alloys 1, 6, and 8 show evidence of epitaxial growth from the mould wall. Although an attempt was made to ensure that arc-melting was done in a similar manner for each alloy, different grain structures still resulted. The investment cast material had a more consistent grain structure and size.

79
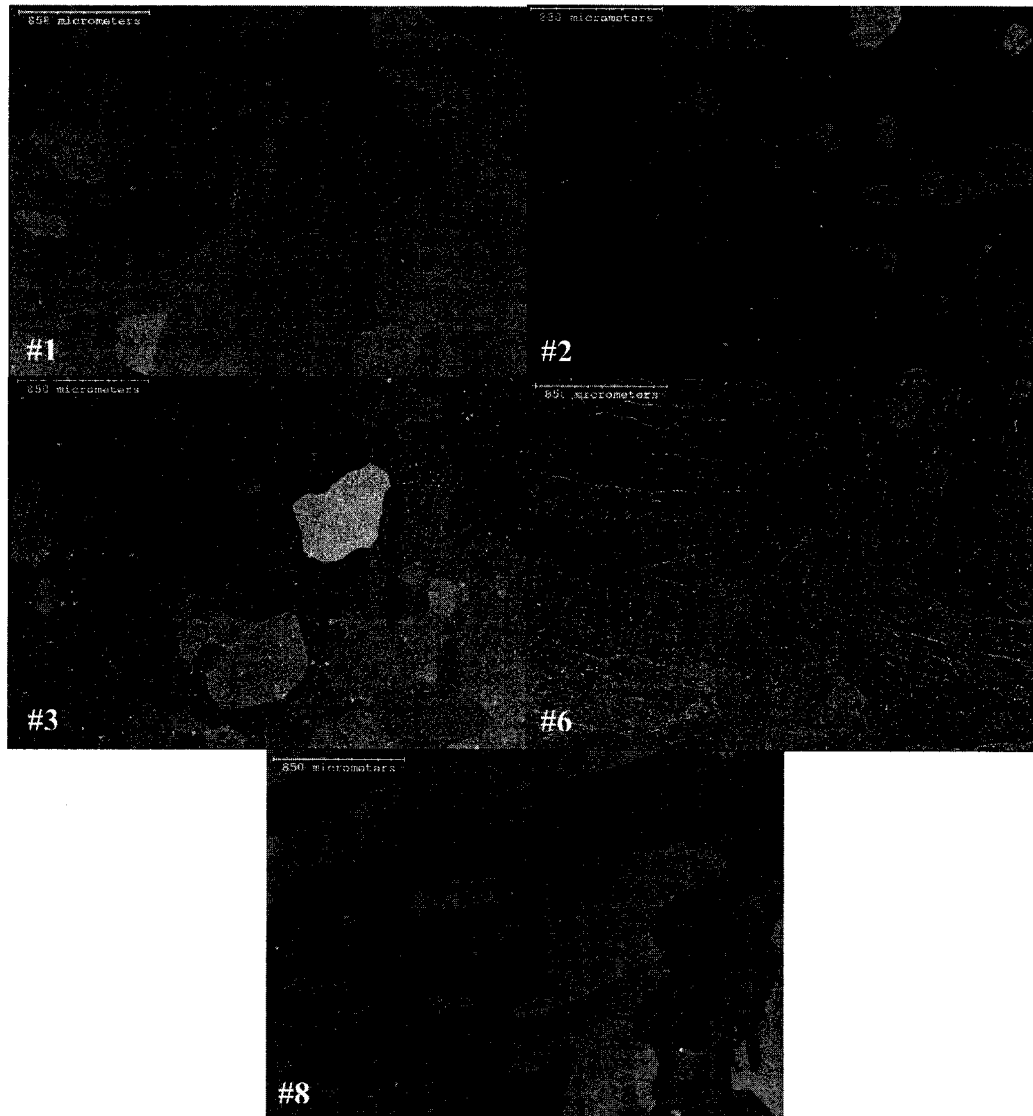
Figure 32: SEM Images of the Re-Melted Alloy Grain Structures: Alloy 1 (NiAl); Alloy 2 (NiAl + CeO_2 + Cr); Alloy 3 (NiAl + Ce); Alloy 6 (NiAl + Ce + Cr); and Alloy 8 (NiAl + CeO_2 + Cr) (SE)

High magnification examination and comparison were reserved for the homogenized material and is presented below.

80

5.1.1.1 Alloy 1: NiAl

Alloy 1 displayed a single phase microstructure under all magnifications. Figure 33 shows a representative image of the microstructure. There was no noticeable effect of cooling rate on the microstructure.
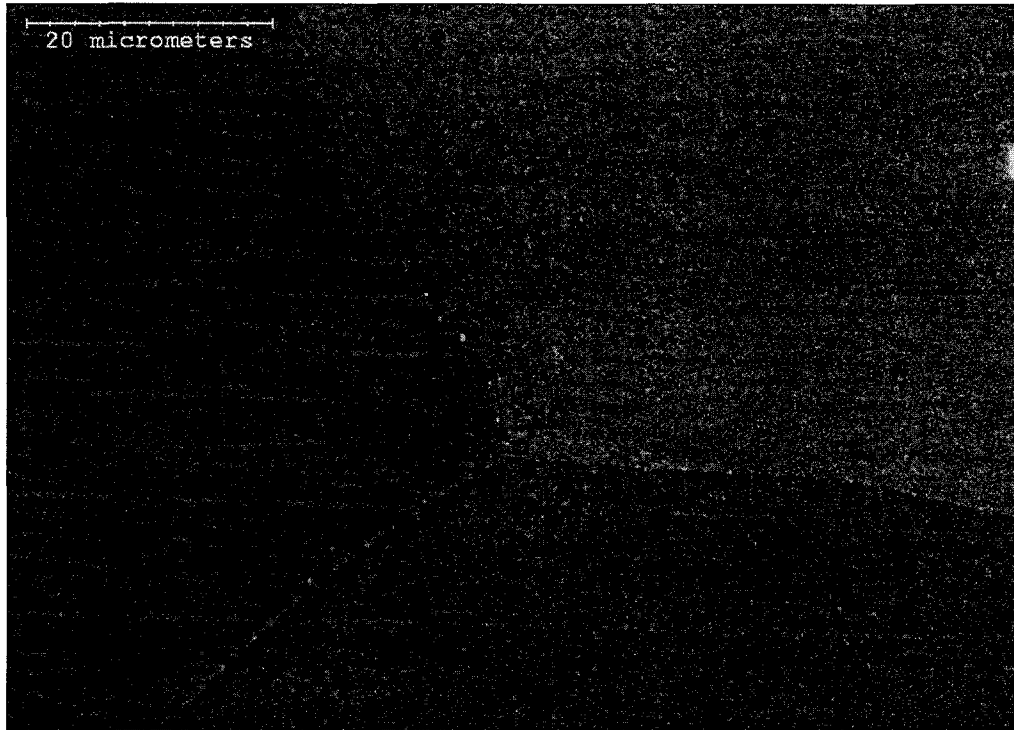
Figure 33: SEM Image of Alloy 1 under High Magnification (SE)

5.1.1.2 Alloy 2: NiAl + Cr + CeO₂

Metallographic examination of alloy 2 revealed a microstructure consisting of chromium precipitates in the 1-μm range scattered through the grains and large cerium-containing particles at the grain boundaries and in the grain interior. Figures 34, 35, and 36, show microstructures of the air, 4-hour, and 24-hour cooled conditions, respectively. Large, irregularly-shaped chromium particles could be seen in all cooling conditions. Judging from the size of these particles,

81

they are most likely undissolved chromium. In addition to the approximately 1-µm chromium precipitates seen in all three of the cooling conditions, very fine precipitates were seen in the 24-hour cooled alloy (Figure 37). EDX Analysis of an area of the matrix containing these fine precipitates yielded elevated chromium levels. In light of the EDX analysis, these precipitates are assumed to be α-chromium.
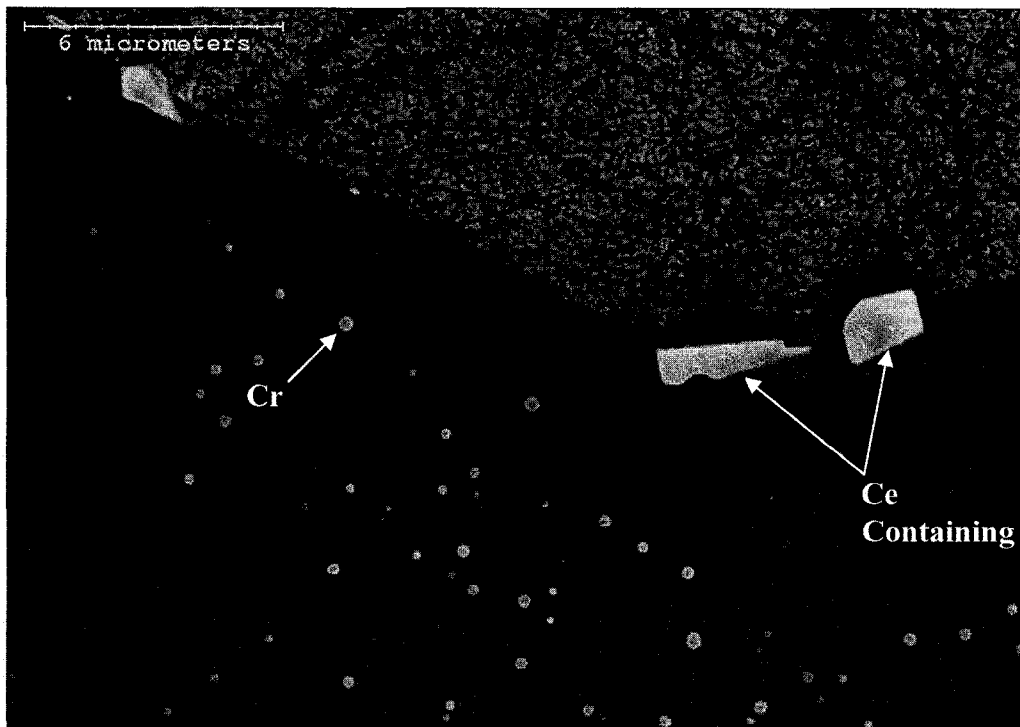
Figure 34: SEM Image of Alloy 2 (air cooled) (SE)

82
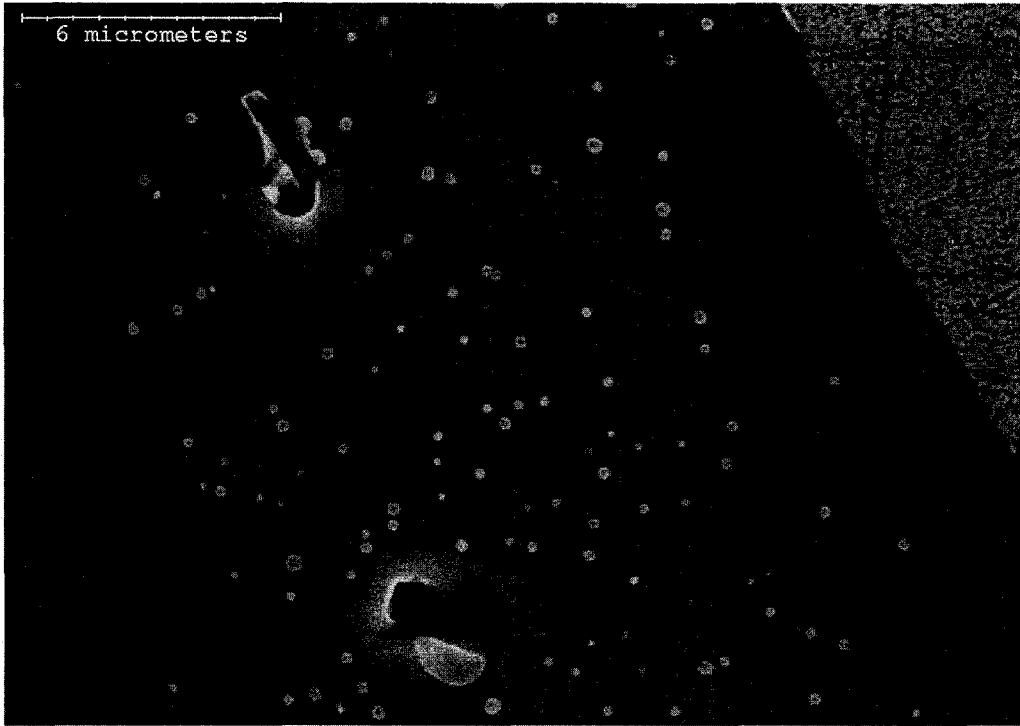
Figure 35: SEM Image of Alloy 2 (4-hour cooled) (SE)
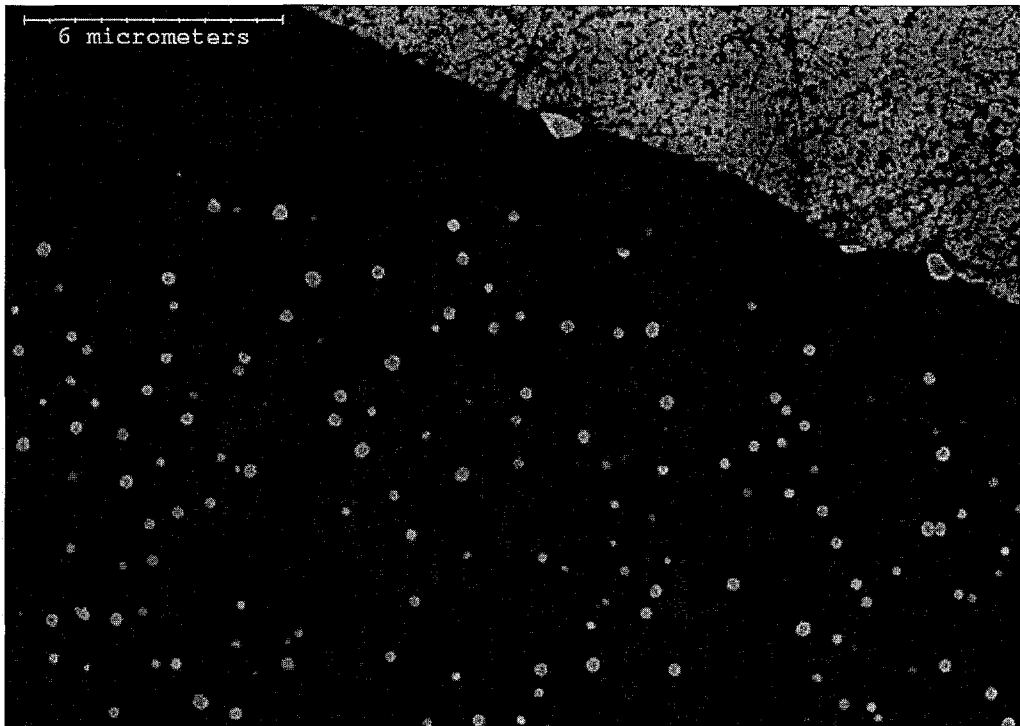
Figure 36: SEM Image of Alloy 2 (24-hour cooled) (SE)

83
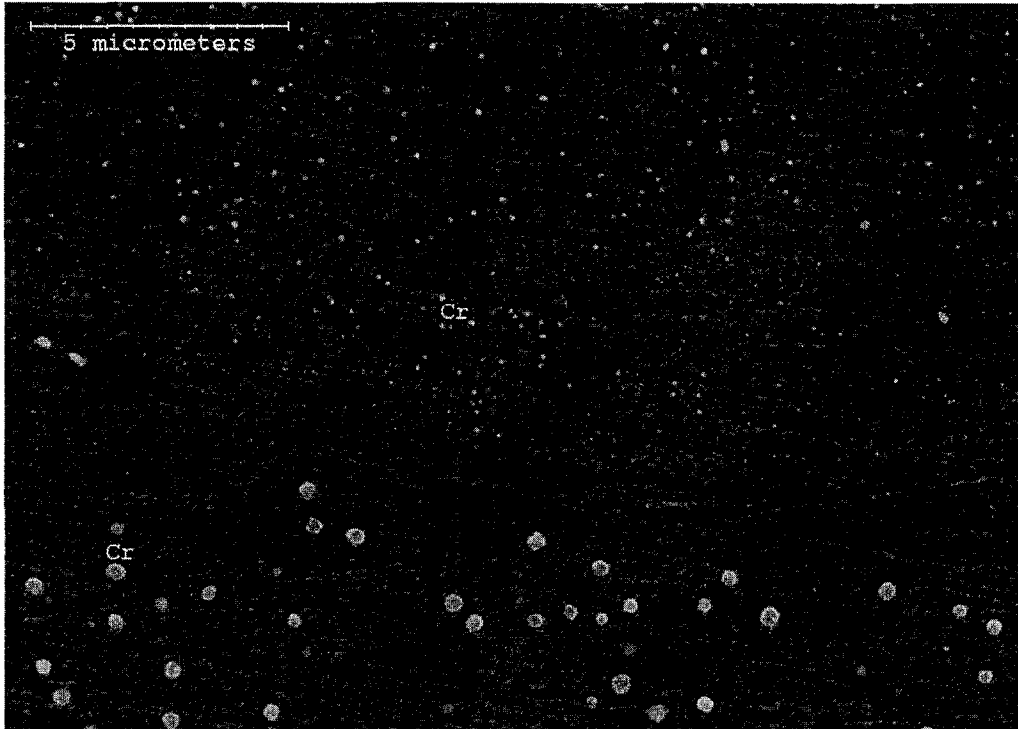
Figure 37: SEM Image of Bimodal Sizes of Chromium Precipitate in Alloy 2 (24-hour cooled) (SE)

5.1.1.3 Alloy 3: NiAl + Ce

SEM examination of alloy 3 revealed a microstructure with voids along the grain boundaries and in the grain interiors under all three cooling condition. Figure 38 shows alloy 3 in the homogenized and air cooled condition. This figure is also representative of the 4-hour and 24-hour cooled states. Alloy 3 had additions of metallic cerium, which would be expected to be visible. It is, therefore, reasonable to assume that the voids are the remnants of cerium particles removed during polishing or etching. Figure 39 shows some white particles remaining along the grain boundary, which were found to be cerium-containing via EDX analysis.

Figure 38: SEM Image of Alloy 3 Homogenized and Air Cooled (SE)
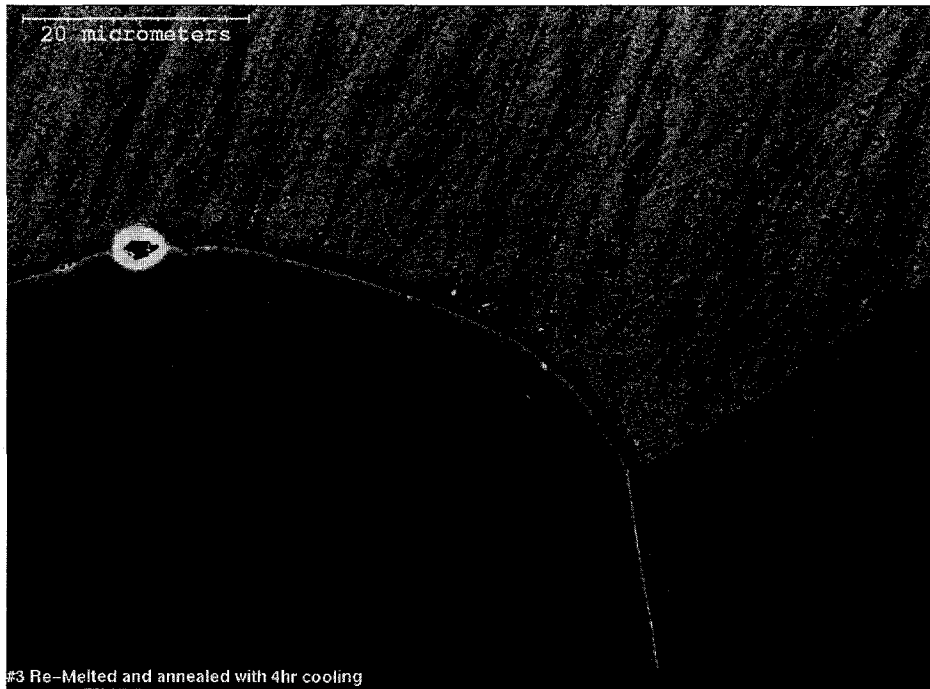
Figure 39: SEM Image of Alloy 3 Homogenized and 4-hour Cooled (SE)

85

5.1.1.4 Alloy 6: NiAl + Cr + Ce

Looking at alloy 6 in the SEM, a microstructure similar to alloy 2 can be seen. Figures 40, 41, and 42, show the microstructure in the air, 4-hour, and 24-hour cooled states, respectively. Large chromium precipitates can be seen in all three conditions. As in the case of alloy 2, large, irregular chromium particles were seen in all cooling conditions. In Figure 40 (air cooled), only the large-size precipitates are visible, while in Figure 41 (4-hour cooled), much smaller precipitates can be seen in the background matrix. The fine background precipitates are still more noticeable in Figure 42 (24-hour cooled). A large piece of either cerium or cerium oxide can be seen in the 4-hour cooled image (Figure 41), while a much smaller one can be seen in the 24-hour cooled specimen (Figure 42).

Figure 40: SEM Image of Alloy 6 Homogenized and Air Cooled (SE)

86
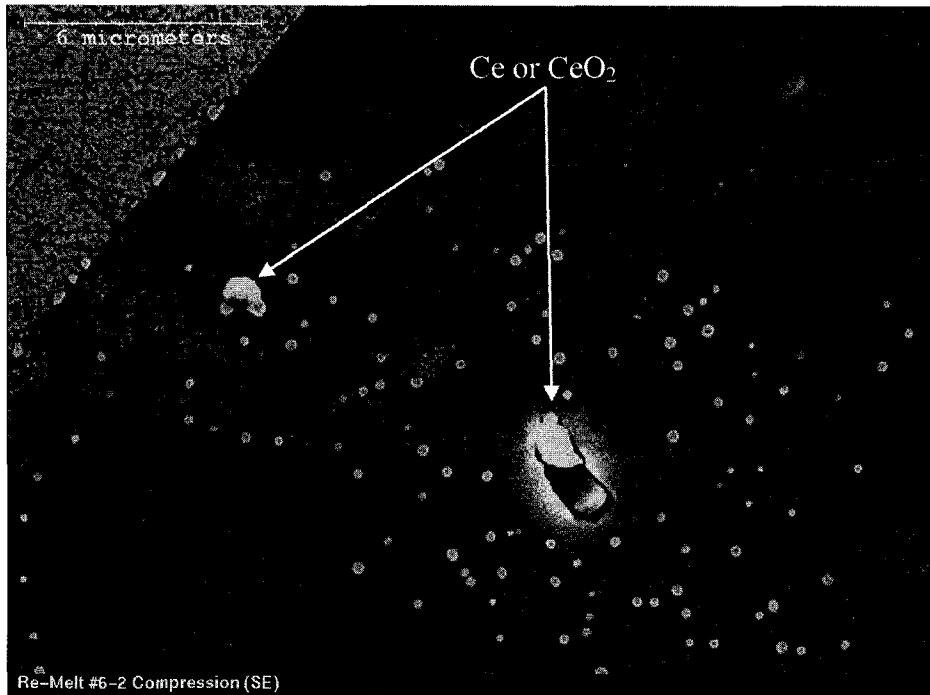
Figure 41: SEM Image of Alloy 6 Homogenized and 4-hour Cooled (SE)
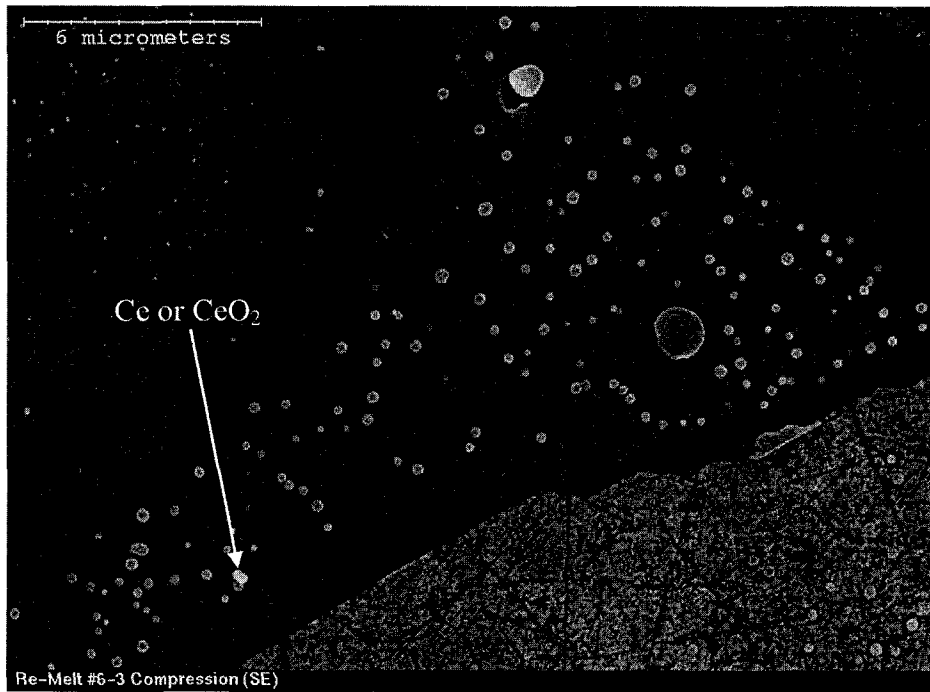
Figure 42: SEM Image of Alloy 6 Homogenized and 24-hour Cooled (SE)

87

5.1.1.5 Alloy 8: NiAl + Cr + CeO$_2$

Figures 43, 44, and 45, show the microstructure of alloy 8 in the air, 4-hour, and 24-hour cooled conditions. In general, the appearance of the microstructure is in agreement with alloys 2 and 6 for the 4- and 24-hour cooled conditions. There are large chromium precipitates as well as finer precipitates that are visible in the 24-hour cooled sample. Large pieces of undissolved chromium can also be seen in Figure 44. The microstructure of the air cooled condition (Figure 43) appears to be less defined compared with the other two. Small precipitates can be seen, but they have a faded appearance. It is possible that the SEM image became unstable during capture. Still, evidence of the chromium precipitates can be seen.

Figure 43: Alloy 8 Homogenized and Air Cooled

88
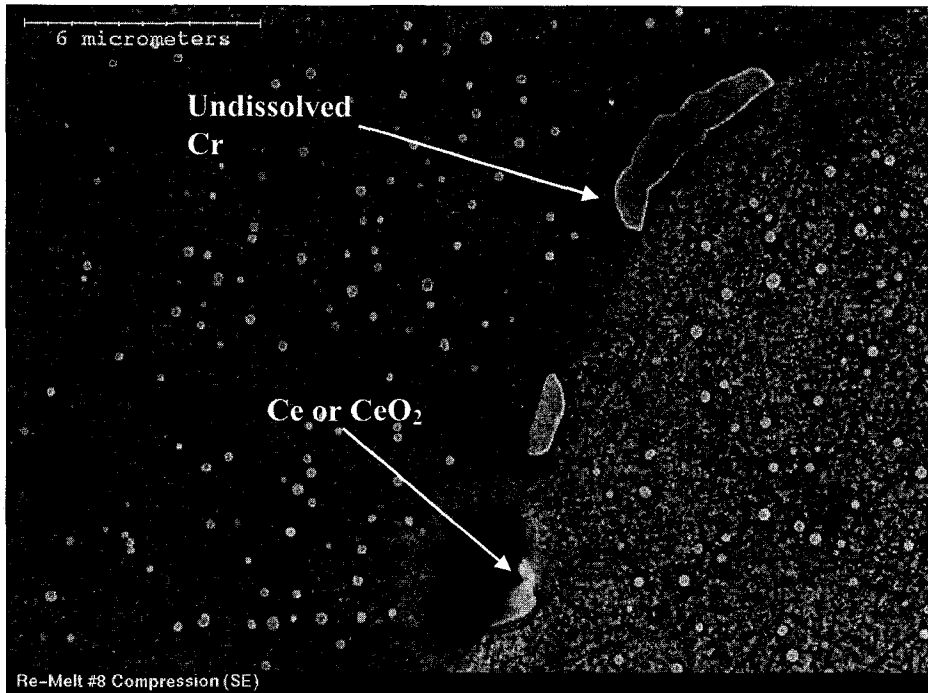
Figure 44: SEM Image of Alloy 8 Homogenized and 4-hour Cooled (SE)

Figure 45: SEM Image of Alloy 8 Homogenized and 24-hour Cooled (SE)

89

5.1.1.6 Metallography Results Summary

A summary of the metallographic features seen in the re-melted alloys has been tabulated in Table 5 below.

Table 5: Re-Melted Alloy Metallographic Summary

Alloy	Cooling	Ce / CeO_2	Cr	Comments
1 Al/Ni = 0.99	Air	None	None	Single phase microstructure
	4-hour			
	24-hour			
2 Al/Ni = 0.99 0.02% Ce, 2.04% Cr	Air	Particles at grain boundaries and in grains	~1 µm	Large undissolved chromium particles seen
	4-hour			
	24-hour		~1 µm and fine	
3 Al/Ni = 0.99 0.02% Ce	Air	Particles at grain boundaries and in grains	None	Voids with small Ce particles left
	4-hour			
	24-hour			
6 Al/Ni = 1.03 0.02% Ce 2.11% Cr	Air	Particles at brain boundaries and in grains	~1 µm	Large undissolved chromium particles seen
	4-hour		~1 µm and fine	
	24-hour			
8 Al/Ni = 1.02% < 2 ppm Ce 2.09% Cr	Air	Particles at brain boundaries and in grains	~1 µm	Large undissolved chromium particles seen
	4-hour			
	24-hour		~1 µm and fine	

5.1.2 Metallography Discussion

The metallographic discussion will be separated into two sections relating to the effects of cerium and chromium, respectively.

5.1.2.1 Effect of Cerium

Large voids could be seen in alloy 3 (metallic cerium addition only), whereas alloy 1 (commercially pure) showed no indications. These voids were found on the grain boundaries and in the grains, with a few voids containing some remnant cerium. Due to its large atomic size, cerium is not expected to be soluble in the NiAl matrix; thus, it is no surprise to find it in large particles. Metallic cerium

90

was also added to alloy 6 along with chromium. In this alloy, large cerium-containing particles were found and in one case, a void around the particle was formed as well. As was hypothesized previously, these voids could either be from the polishing procedure physically removing the particle or from the etchant dissolving it.

Alloys 2 and 8 both had additions of cerium oxide powder of approximately 9-nm size distribution. Similar to alloys 3 and 6, larger particles of cerium-containing compound were found scattered both at the grain boundaries and in the grain interior. Considering the size of the particles seen, they must be agglomerations of smaller ceria particles. The heat of the melting arc could have even sintered these particles together. Since the ceria added to alloys 6 and 8 was of an average size of 9 nm, there are most likely small ceria particles scattered through the matrix that are too small to be visible.

In a number of cases, cerium was found along with chromium. In general, it was common to find what little cerium or ceria was visible with chromium, as seen in Figures 41, 42, and 44. This may simply be a result of precipitation occurring on the cerium or ceria particle or else chromium may have some affinity for cerium (or visa versa). Further investigation would have to be performed to verify this.

91

5.1.2.2 Effect of Chromium

The precipitates seen in the three chromium-containing alloys were expected since more than the accepted solubility limit of 1 at.% was added. Similarly-sized α-chromium precipitates between 500 and 1000 nm have been seen in NiAl when additions over 2 at.% were made [102, 103, 112]. These precipitates were found to be round and considered too large to be coherent in nature.

The smaller particles seen in the 24-hour cooled condition of all three alloys, as well as the 4-hour cooled condition of alloy 6, have also been observed before. A similar bimodal size distribution was seen by Cotton et al. [99] in a NiAl alloy with 5 wt.% Cr added. Cotton et al. observed precipitates of the 10- to 25-nm and the 500-nm size range, but the larger were often bulky and irregularly shaped. As a result of this irregular shape, it was assumed by Cotton et al. that they were undissolved chromium. In contrast, the particles seen here are very round in shape and appear to be precipitates. Bimodal chromium precipitation has been noted by other authors as well [102, 103, 112]. Fischer et al. [88] has recently indicated that there may be three phases resulting from as little as 2 at.% Cr addition. Fischer et al. found evidence of large α-Cr particles (~1 micron), as well as smaller x-phase particles (<100 nm), which were determined to be Cr_2Al.

From their abundant presence, it seems that the large chromium precipitates grow quickly such that even rapid cooling did not seem to affect precipitation. This observation is in agreement with research conducted by Tian et al.[101]

92

who found that even quenching in water could not suppress the precipitation of coarse α-chromium particles. The size and number of large precipitates vary little from the air cooled to 24-hour cooled conditions; conversely, the fine precipitates seem to develop much slower as was also found by Tian et al. No evidence of the second size distribution can be seen in the air cooled condition, but the size appears to increase from the 4-hour to 24-hour cooled state. Tian suggests that these fine precipitates are coherent in nature and are mainly responsible for second phase hardening.

5.2 Mechanical Strength

The mechanical testing section will be split into three parts consisting of hardness testing results, compression testing results, and discussion of both the hardness and compression testing results together.

5.2.1 Hardness Testing Results

Figure 46 shows a hardness summary of the re-melted alloys. The error bars shown on the graph are simply plus/minus the standard deviation of the averaged number set.

From Figure 46, there are a few noticeable trends. The hardness of the chromium-containing alloys (alloy 2, 6, and 8) is higher than that of the cerium containing alloy (alloy 3). The hardness of the commercially-pure NiAl alloy (alloy 1) is nearly equivalent to the chromium-containing alloys.

93
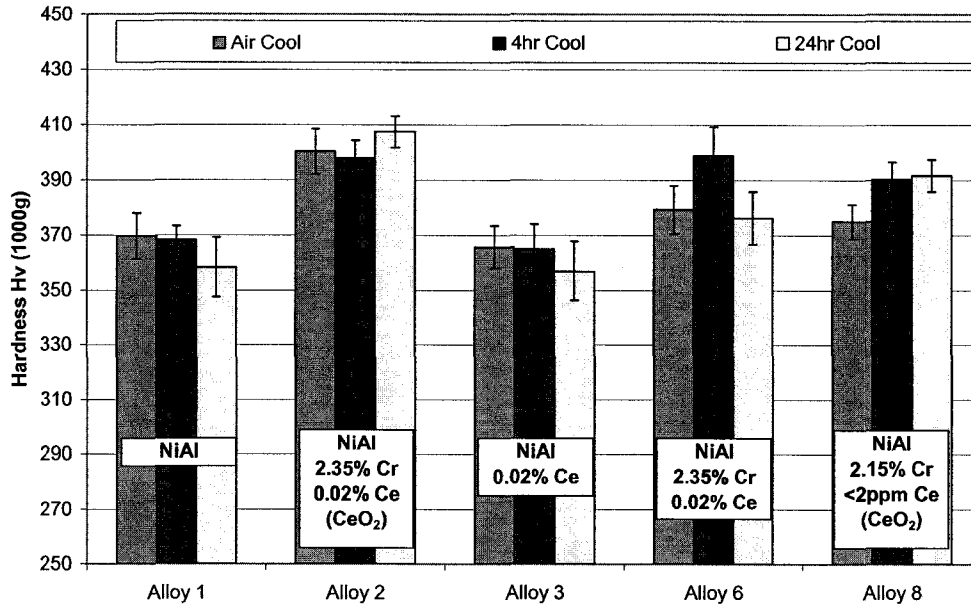
Figure 46: Re-Melted Hardness Summary (1000-g load)

94

5.2.2 Compression Testing Results

The stress-strain curves of the re-melted alloys still exhibited serrated behaviour through the entire loading range. Figure 47 shows the re-melted material, while Figure 48 shows the investment cast material for comparison purposes. The re-melted material appears slightly different but it is still not smooth as desired.
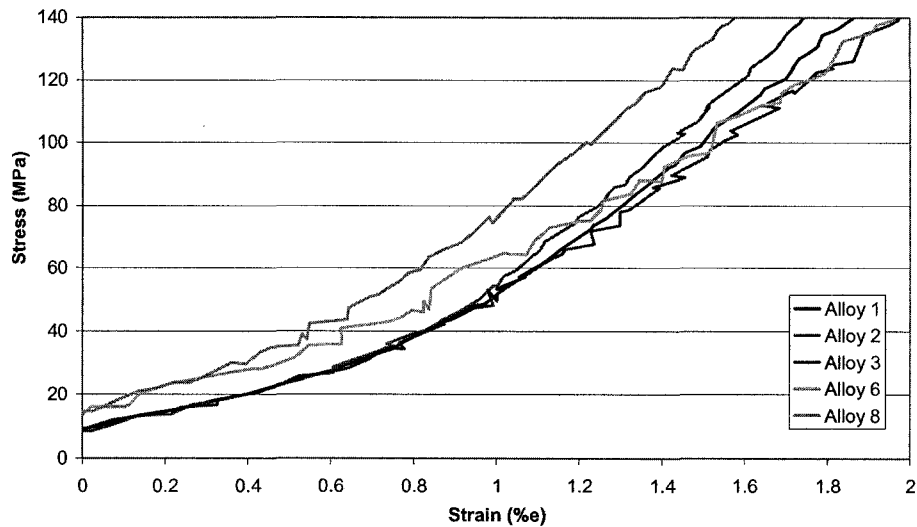
Figure 47: Re-Melted Compression Behaviour (close range)
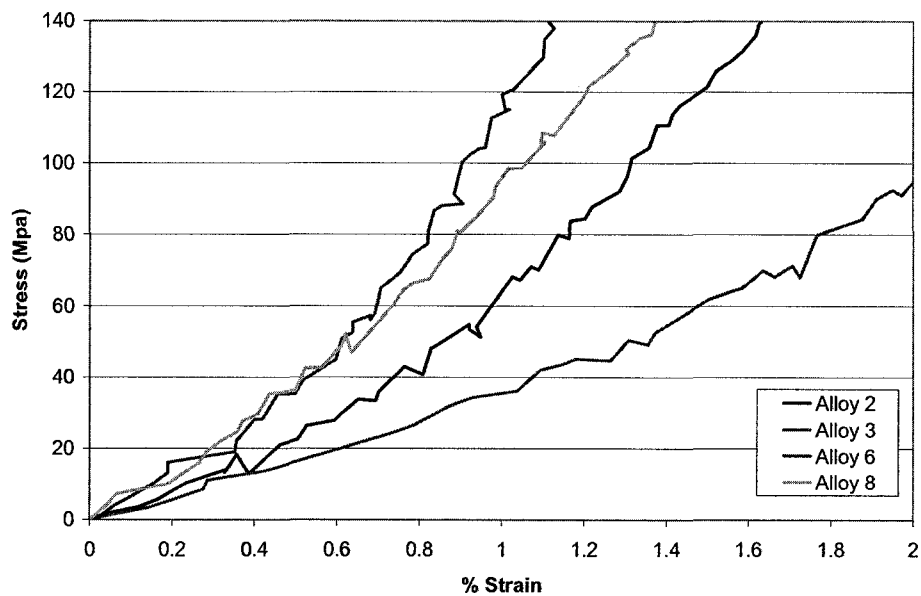
Figure 48: Un-HIPed, Investment Cast, Compression Behaviour (close range)

95

Compression testing curves for the 4-hour cooled condition are shown in Figure 49. Figures 50 and 51 show a comparison of the compression curves for the three different cooling conditions for alloys 2 and 6, respectively. A maximum compressive stress comparison is presented in Figure 52, with the data listed in Table 6. Since it appears that the majority of the alloys fail after peaking with a relatively consistent shape, values were omitted if the compression behaviour was drastically different from this. Error bars in Figure 52 are plus/minus the standard deviation listed in Table 6.

In the 4-hour cooled compression curve summary shown in Figure 49, all of the alloys except three have similar behaviour. Alloy 3 (NiAl + Ce) only reaches about half of the stress and strain of the others before failure. As with the hardness values, the compression behaviour of the commercially-pure NiAl alloy (alloy 1) is similar to that of the chromium-containing alloys with an almost identical peak stress. Figures 50 and 51 compare the compression curves for alloys 2 (NiAl + CeO_2 + Cr) and 6 (NiAl + Ce + Cr), respectively, in the three different cooling conditions. It can be seen that the 4-hour cooled condition for alloy 2 clearly reaches higher stress before failure than the air or 24-hour cooled curves, which is in agreement with the hardness results. Looking at the peak compressive stress summary in Figure 52, the standard deviation of the peak stress in the 4-hour cooled case is significantly higher that the apparent difference in peak stress. As a result of the high standard deviation, no comment

96

can be made with respect to the effect of cooling rate on the peak compressive

stress.
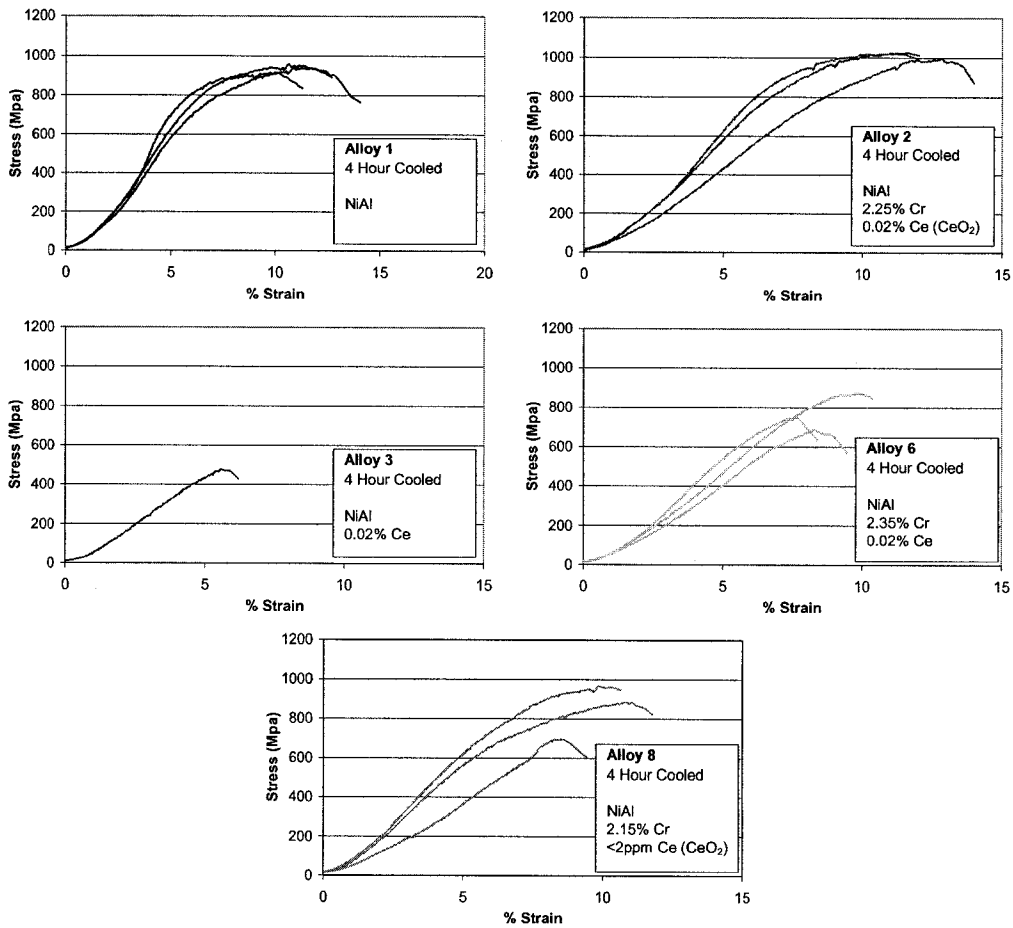
Figure 49: Compression Test Summary (4-hr cooled)

97
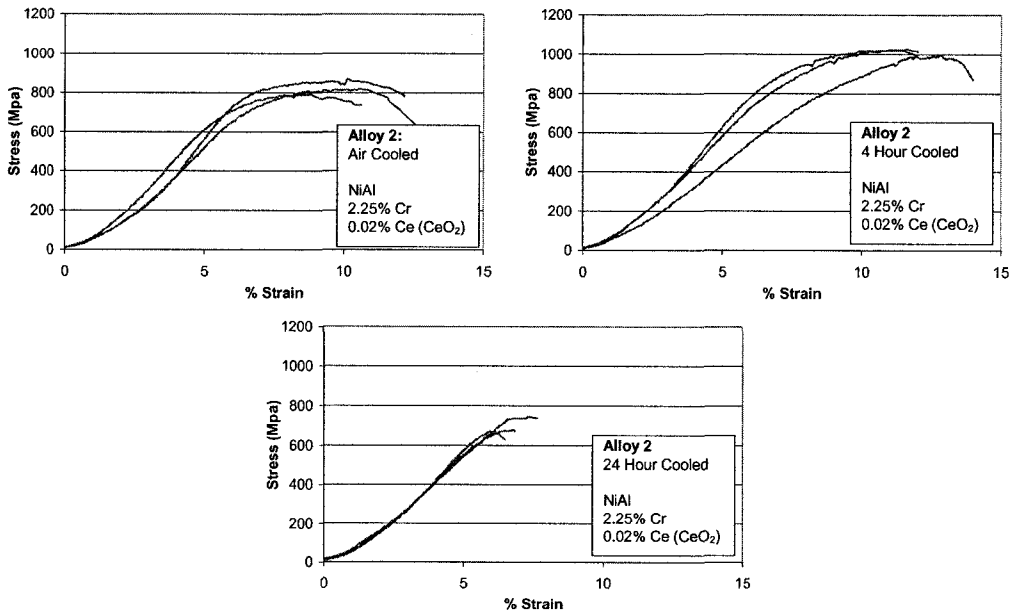
Figure 50: Alloy 2 Compression Test Summary
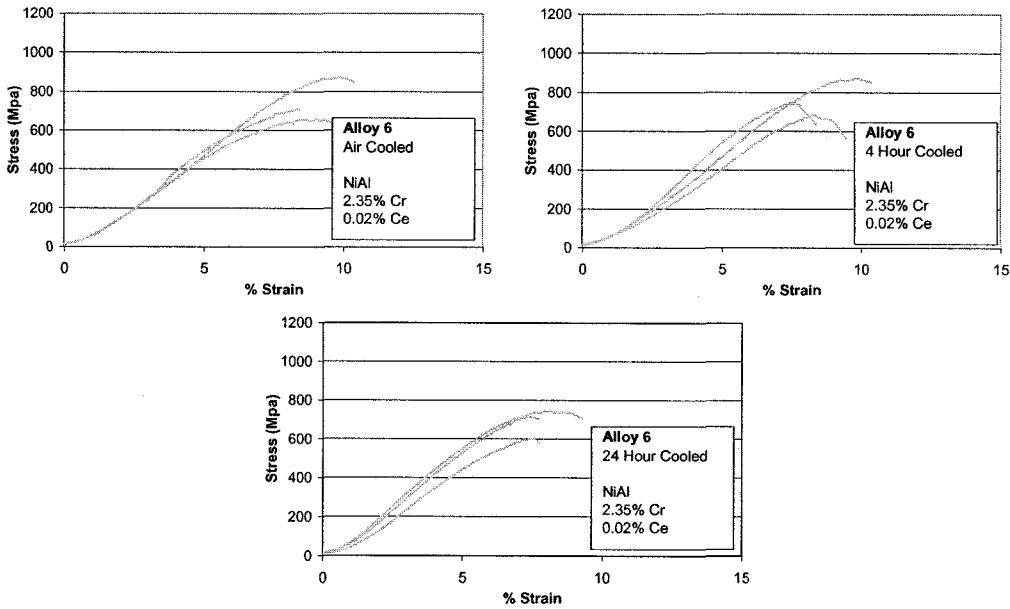
Figure 51: Alloy 6 Compression Test Summary

98

As in the case of the investment cast material, peak strain will be used as a quantitative measure of the ductility. Figure 53 presents the peak stress versus peak strain plot; Figure 54 shows a comparison of the peak strains. From the peak strain comparison, alloy 1 (NiAl) agrees well with the tests from the investment cast condition, while alloys 2, 3, and 6 have decreased peak strain. Although the 4-hour cooled peak strain of alloy 2 (NiAl + CeO_2 + Cr) appears to have decreased, it is still higher than that of the commercially-pure NiAl, suggesting some effect of chromium and/or ceria. There were only two successfully cut compression specimens from alloy 3 (NiAl + Ce). The first test specimen failed before any sign of yielding and the second only reached 5.6% strain before peak, which is down from values between 8 and 9% for the HIPed investment cast material. The peak strain values for alloy 6 (NiAl + Ce + Cr) are significantly lower than that of the 4-hour cooled condition in the HIPed material. Values fell from between 9.9 and 15.5% for the HIPed material to between 7.6 and 9.8% for the re-melted material in the 4-hour cooled state. Peak strains for the un-HIPed investment cast material were even higher, residing between 11.7 and 16.5%. Alloy 8 peak strain results are higher in the re-melted conditions compared with either of the investments cast materials. The peak strain values for the HIPed and un-HIPed material were between 6 and 9%, while the re-melted material in the 4-hour cooled condition had peak strains between 8.5 and 10.8%.

99
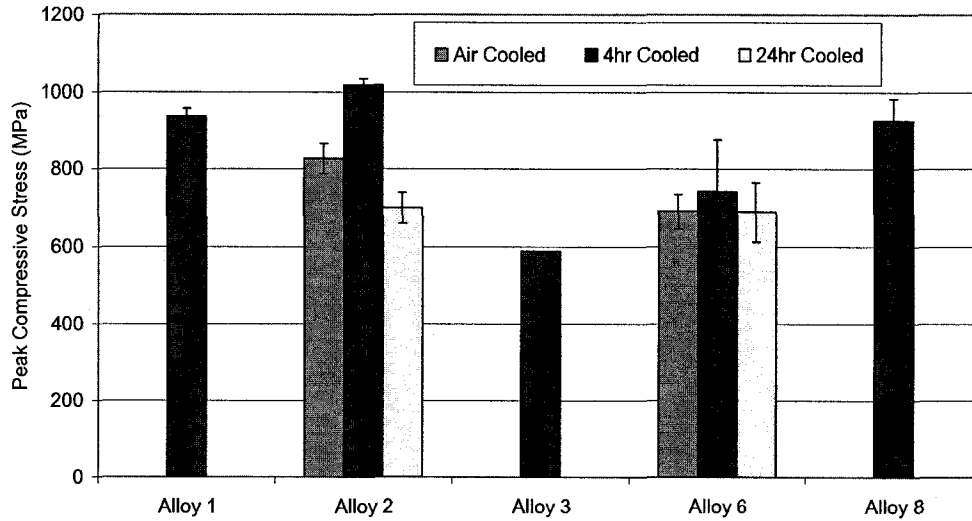
Figure 52: Peak Compressive Stress Comparison

Table 6: Peak Compressive Stress

Alloy	Cooling	Test Results (MPa)			Average (MPa)	Standard Deviation
1	4-hour	916	955	940	937	19.7
2	Air	793	870	818	827	39.3
	4-hour	1027	977	1029	1018	17.9
	24-hour	674	745	679	699	39.6
3	4-hour	588	No data	No data	588	n/a
6	Air	721	659	No data	690	84.5
	4-hour	873	747	604	741	134.6
	24-hour	604	749	714	689	75.7
8	4-hour	884	966	No data	925	58.0
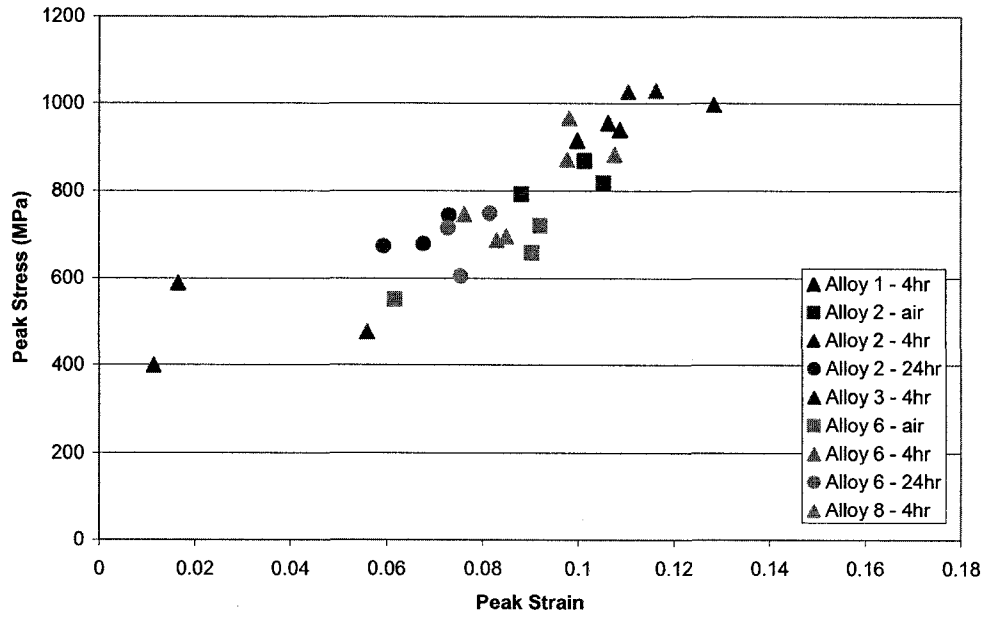
Figure 53: Re-Melted Peak Stress versus Peak Strain Plot
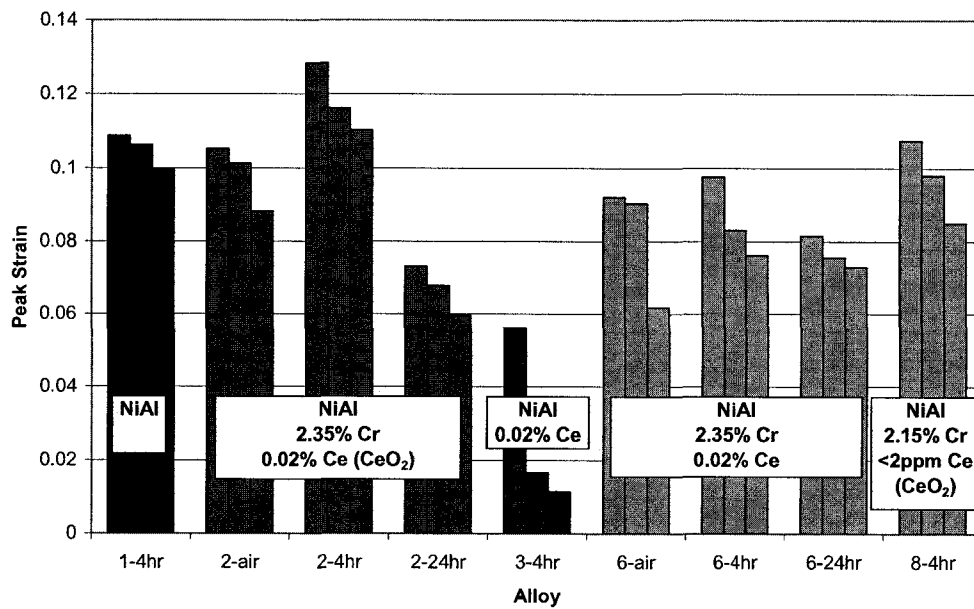
Figure 54: Re-Melted Peak Strain Comparison

101

5.2.3 Discussion of Results: Hardness and Compression Testing

The re-melted hardness values were slightly higher than those of the investment cast material. One possible reason for this could be error in measurement, although this would be unlikely since calibration blocks were used before hardness testing. Another possibility is that the aluminum to nickel fraction is just slightly lower due to aluminum loss during melting. A lower aluminum-to-nickel fraction would result in hardening by nickel anti-site defects. For this to be the case, the ICP analysis would be in error.

Similar to the investment cast alloys, cracking was apparent during all stages of compression testing. As a result, qualitative comparison of yield strength will not be made. The compressive yield strength of stoichiometric NiAl has most recently been reported to be between 148 and 834 MPa and the compressive fracture strength between 468 and 867 MPa, both depending on the aluminum-to-nickel fraction [99]. In a qualitative comparison to the re-melted data presented here, it is evident that all the test results are significantly elevated. What is also noticeable is that after the compression curve is clearly non-linear, there is substantial work hardening behaviour.

Detailed discussion of the mechanical test results will be separated into a number of sections to follow.

5.2.3.1 Elevated Strength of Chromium-Containing Alloys

The high hardness and compression strength for the chromium-containing samples (Alloys 2, 6, and 8) could be a result of either constitutional defects or solid solution and second phase hardening effects of the chromium. Alloy 2 was determined to have an aluminum-to-nickel fraction of 0.99 after re-melting, while the fractions for alloys 6 and 8 were 1.03 and 1.02, respectively. According to Noebe et al. [19], who summarized relevant research, the hardening rates for stoichiometric deviations are 120 and 350 MPa/at.% for nickel- and aluminum-rich sides, respectively. This would result in the following hardening rates (with respect to yield strength): of approximately 35 MPa for alloys 1, 2, and 3; 265 MPa for alloy 6; and 146 MPa for alloy 8. The solid solution hardening potential of chromium atoms has been reported to result in a 258-MPa yield strength increase per at.% Cr addition up to 1 at.% [19]. This finding was based on addition to stoichiometric NiAl. Although only an increase in yield strength was reported, it is likely that the flow stress of the material would also increase due to the interaction of dislocation stress fields, with the stress imparted on the matrix by the chromium atom. The effect of chromium addition on the strength of NiAl is known to be composition dependent. Cotton et al. [99] found that the addition of chromium shifts the compositional strength minima from Al/Ni = 1 to 0.98 for 1% Cr, 0.96 for 2% Cr, and 0.90 for 5% Cr. Chromium additions of 1% to the stoichiometric composition resulted in a yield strength of 403 MPa and a fracture strength of 457 MPa. The same additions to Al/Ni = 0.98 and 1.02 alloys resulted in yields of 450 and 461 MPa and fracture

103

strengths of 534 and 514 MPa, respectively. Additions of 2% to the stoichiometric composition result in yield and fracture strengths of 440 and 560 MPa, respectively. The same additions to Al/Ni = 0.96 and 1.02 alloys resulted in yields of 461and 571 MPa and fracture strengths of 500 and 599 MPa, respectively. Further addition of 5% Cr to the stoichiometric composition resulted in slightly more hardening, with yield and fracture strengths of 463 and 608 MPa, respectively. From this, we can see that at most, little more than 570 MPa yield strengths and 600 MPa fracture strengths could be expected from the chromium additions used in alloys 2, 6, and 8.

As mentioned in Section 5.1, small precipitate particles were barely noticeable in SEM images. These are similar in appearance to particles found by Tian et al. [101] in NiAl alloys with chromium additions between 4 and 8 at.%. These precipitates were observed to be coherent in nature and contribute significantly to precipitation hardening. Tian et al. found that upon ageing, an increase in hardness was first observed, followed by a peak and subsequent decrease that corresponded to the loss of precipitate-matrix coherency. Dislocation looping was found to occur at a particle size of approximately 300 nm. Cotton et al. and Fischer et al. [99, 103] also observed coherent chromium particles that were less than 100 nm in size. The precipitation study by Tian et al. employed quenching from a high temperature, followed by ageing at temperatures of 700, 800, and 900°C. In contrast, the alloys investigated here were cooled at a certain rate from high temperature. This approach would also allow precipitation, but the time at

104

temperature required for over-ageing would be difficult to determine and a function of the time spent in certain temperature varies during cooling.

Considering the strength contributions of constitutional hardening mixed with the solid solution and precipitation hardening of chromium, as well as the possible strain rate effects, the peak stresses seen in the chromium-containing alloys still seems high. The strain rate used by Cotton et al. [51] was 1.3×10^{-4} which is nearly an order of magnitude lower than that used here. The strength of NiAl is known to increase with increasing strain rate, but not enough to explain the peak stress values here [19, 50]. The fracture strengths listed above are, by definition, the stress at the point of the onset of fracture. Peak loads in these tests were the maximum load obtained before final failure. Because it seemed that fracture began shortly after the onset of loading, it was not possible to discern a fracture stress. Due to this, it is understandable that the peak stresses in Table 6 could be higher than fracture stresses reported in the literature. The NiAl matrix material would probably still have significant strain hardening potential after the onset of fracture.

5.2.3.2 Elevated Strength of the Commercially Pure NiAl (Alloy 1)

The observation of the commercially-pure NiAl (alloy 1) being nearly as hard as the chromium-containing alloys and having a similar compression behaviour is noteworthy. Pure NiAl would be expected to be much weaker than NiAl with chromium addition. More recent research has reported the compressive yield and

105

fracture strengths of cast and homogenized NiAl as 148 and 468 MPa, respectively, in the stoichiometric composition. Based on the compositions in Table 3, some constitutional defect hardening could be expected (approximately 35 MPa) based on the aluminum-to-nickel fraction of 0.99. This does not nearly account for the apparent strength of alloy 1. Another factor that must be considered is the effect of interstitial solid solution hardeners.

The solid solution hardening effects of both boron and carbon were investigated by George and Liu [66]. It was found that the compressive yield strength of NiAl could be increased at a rate of 1500 MPa/at.% by the addition of boron and at a rate of 1700 MPa/at.% by the addition of carbon Both the boron and carbon hardening potentials were based on addition of approximately 1100 at. ppm. Although no boron was detected in the master alloy prior to investment casting, at least 360 at. ppm carbon was analyzed. There is little reason to believe that carbon would be removed during investment casting and there is a good probability that small amounts could have been introduced during arc melting. Assuming 360 ppm carbon, an approximately 60-MPa increase in yield strength might be expected. If both the apparent constitutional and interstitial hardening potentials are combined, a 95-MPa yield increase would be justified. If the same increase were added to the fracture stress, values of 243 and 563 MPa might be expected for the yield and fracture stresses, respectively. Looking at the stress versus strain curves in Figure 49, the alloys strength seems to be significantly higher than this. Table 6 lists the average peak stress for alloy 1 to be 937 MPa,

which is much higher than the approximations made based on composition. It should be mentioned that a 2% aluminum deficiency resulting in an aluminum-to-nickel ratio of 0.92 can increase the yield strength of NiAl by 550 MPa [19]. The relevance of this comment is that compositional point defects can easily account for the increased strength of the commercially-pure NiAl alloy (alloy 1). In light of this, the accuracy of the chemical composition in Table 6 may be in question.

5.2.3.3 Low Strength of Alloy 3 (Metallic Cerium Addition)

Some explanation directed at the strength and hardness of alloy 3 (NiAl + Ce) is warranted. One reason for the low strength and hardness could be that the aluminum-to-nickel ratio is closer to 1:1, which offers the least resistance to dislocation motion. The measured composition points to an aluminum-to-nickel fraction of 0.99, which should only provide up to 35 MPa of hardening. The resultant strength levels seen in the compression curve are in line with accepted strength levels of un-alloyed NiAl.

5.2.3.4 Effect of Cooling Rate

Still to be discussed is the apparent effect of cooling rate from the homogenization temperature on the hardness and compressive strengths. There appears to be a subtle effect of cooling rate on some of the mechanical properties. The hardness of alloy 2 (Figure 46) shows a maximum in the 4-hour cooled condition. The compression curves for alloy 2 show similar behaviour as

107

do the peak stress, and strain at peak stress summaries (Figures 52 and 54). Unfortunately, cooling rate effects on compression properties were not investigated for alloy 8. Since it has virtually the same composition as alloy 2 ($NiAl + CeO_2 + Cr$), comparative results would be desirable.

The reasons for the apparent effect of cooling rate on the mechanical properties of alloy 2 are unclear. The effect could possibly be explained with a simple precipitate aging phenomenon but without further investigation, any additional discussion would be purely speculative.

5.2.3.5 Ductility

In the investment cast material, alloys 2 ($NiAl + CeO_2 + Cr$) and 6 ($NiAl + Ce + Cr$) showed a noticeably higher peak strain than the others. In the re-melted material (4-hour cooled condition), alloy 2 still has a higher peak strain than the commercially-pure NiAl (~10%), but alloy 6 is reduced to an average peak strain of approximately 9%. Only one of the three compression specimens for alloy 3 ($NiAl + Ce$) failed after yield at 5.6%. This peak strain value is down from that of the investment cast material which was over 9%. Alloy 8 ($NiAl + CeO_2 + Cr$) has an average peak strain of approximately 9.5%, which is increased compared to the investment cast value of approximately 7%. This places alloy 8 just less than the peak strain of the commercially-pure NiAl alloy (alloy 1).

108

In general, these results are not too remarkable since the maximum compressive strain attained is 12.8% (alloy 2). This is not significantly different than any of the compressive strain to failure for NiAl published in literature [51, 52, 99]. What may be significant is that the ductility of NiAl is normally reduced by chromium additions, whereas here it appears to increase. The cooling rate effect on hardness and strength is also apparent in the peak strain values for alloy 2, but not alloy 6. Since the phenomenon is seen in the hardness data, it is most likely due to flow stress instead of fracture. Reasons why alloys 6 or 8 do not show the same trend are unclear. Alloy 8, having similar composition, would be expected to demonstrate similar behaviour.

5.2.3.6 Discussion Summary

It appears that some of the behaviours seen can be justified with proven theory or previous findings, but others are not readily explainable. The high strength of the chromium-containing alloys is possible, but the similar strength of the commercially-pure alloy is unexpected. Error in the compositional analysis of the alloys could explain the high strength. If the analyses were in error and the aluminum contents were lower than reported, hardening from nickel anti-site defects would be higher.

Peak strain data still show a slightly increased value for alloy 2 as well as a cooling rate effect. The difference between the peak strains of alloys 2 and 8 is still unexplained, even though the compositions are similar. In addition, the fact

109

that chromium addition seems to increase the ductility of NiAl, based on peak strain, may be significant.

A major parameter that has not been considered is the fracture behaviour. As was mentioned at the beginning of this section, cracking was evident right from the onset of compressive loading. Thus, the peak load and strain could be heavily dependent on fracture mode. Differences in fracture mode could justify the compression results observed. For this reason, it is important to compare the fracture behaviour of the different compositions in order to fully characterize the effect of the alloy additions made. A different fracture mode might explain why alloy 2 shows a trend with cooling rate in both hardness and compression tests and alloy 6 does not. It may also shed light on the different behaviour of alloy 8 compared with that of alloy 2. The next section will address the topic of fracture.

110

5.3 Fracture

As mentioned in Section 5.2, it is suspected that the compressive behaviour observed could be a result of both plastic deformation and fracture propagation. Thus, a study to investigate the fracture behaviour of the different alloys including cooling rate effects was undertaken. The results and discussion of this study are contained in the following sections.

5.3.1 Results

As described in Section 3.0, cast and homogenized samples were fractured and the surfaces were examined via scanning electron microscopy. Compression specimens were also tested to some pre-determined loads followed by sectioning and examination with both optical and scanning electron microscopy.

5.3.1.1 Alloy 1 (Commercially-Pure NiAl)

The fracture surface of alloy 1 in the 4-hour cooled condition is shown in Figure 55. It is apparent that the fracture mode is mainly trans-granular with very little evidence of intergranular fracture. The polished sections shown in Figures 56 and 57 also indicate transgranular fracture. These compression specimens were loaded to 600 and 750 MPa respectively. Figure 58 shows a higher magnification image of the fracture surface of an air cooled specimen. Fracture surfaces from all three cooling conditions were examined, but no differences were found in fracture behaviour. As a result, only select images are shown here.
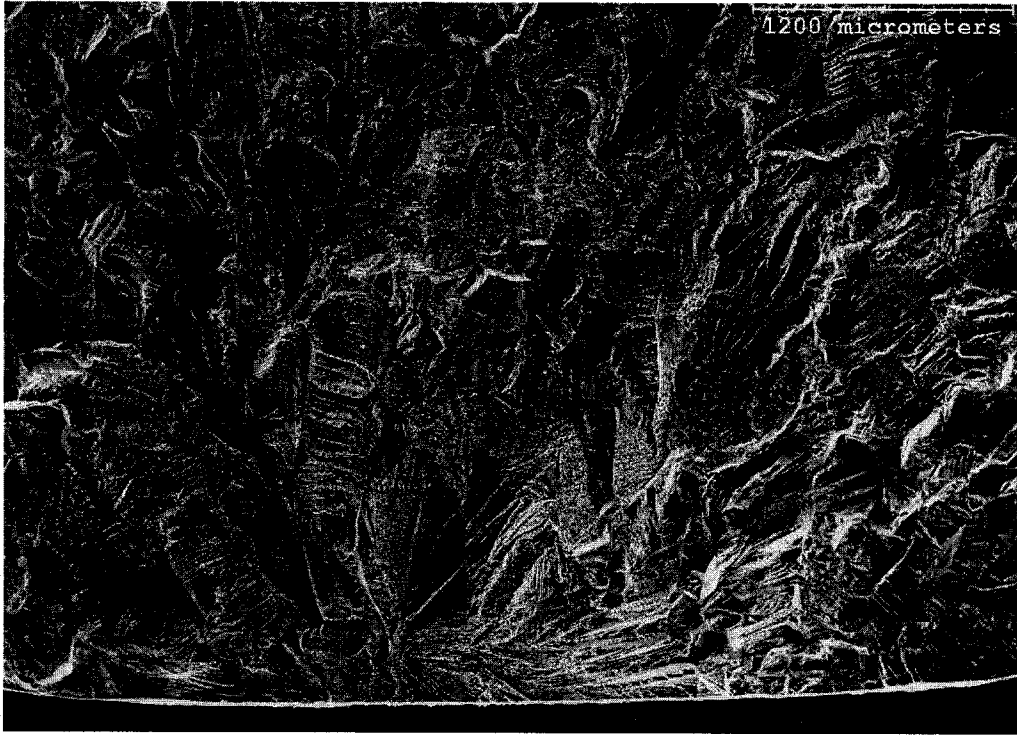
111

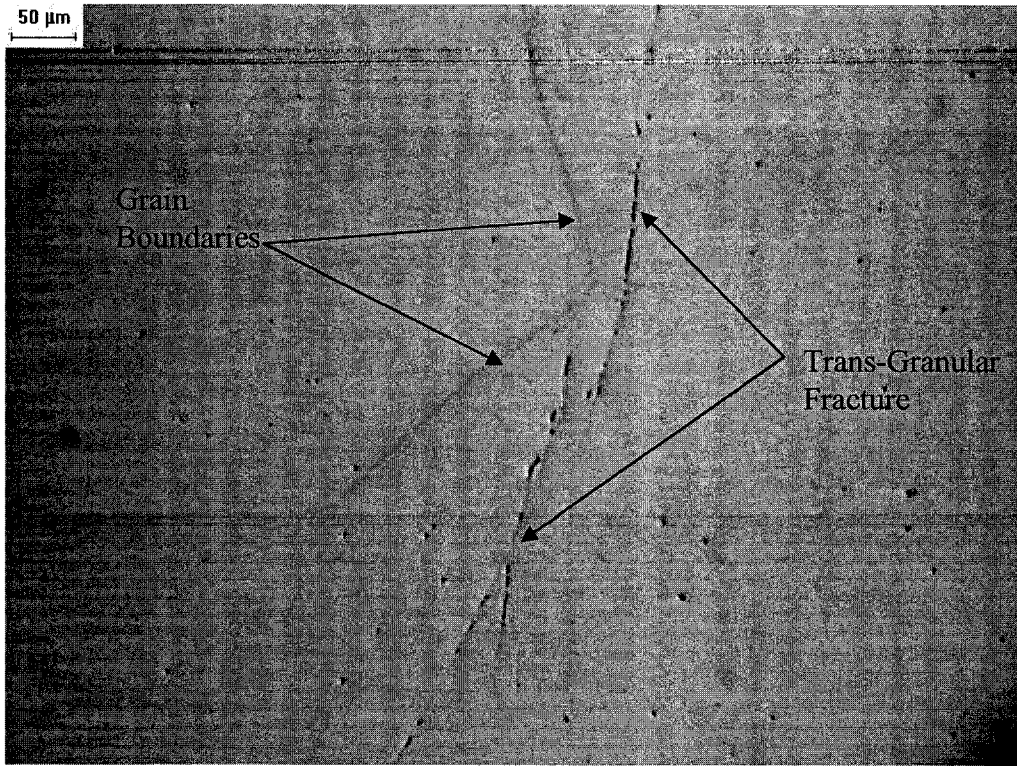**Figure 55: SEM Image of Alloy 1 Fracture Surface (4-hour cooled) (SE)**

112

Figure 56: Optical Microscope Image of Alloy 1, 600 MPa Compression (4-hour cooled) (Polished)
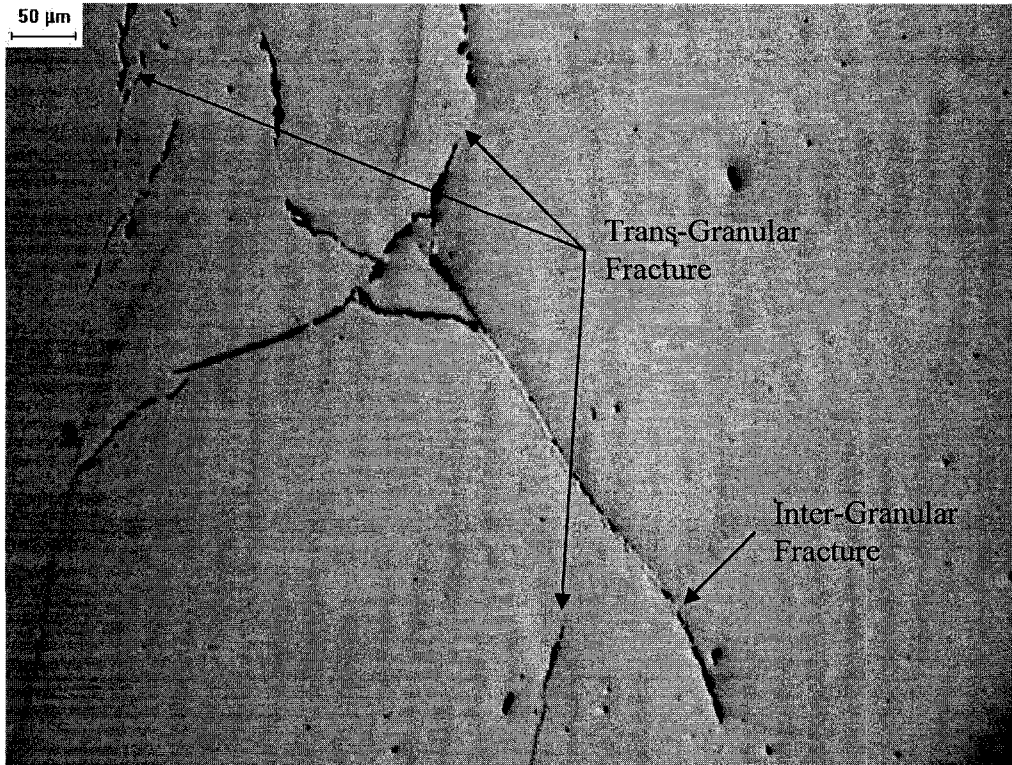
113

Figure 57: Optical Microscope Image of Alloy 1, 750 MPa Compression (4-hour cooled) (Polished)
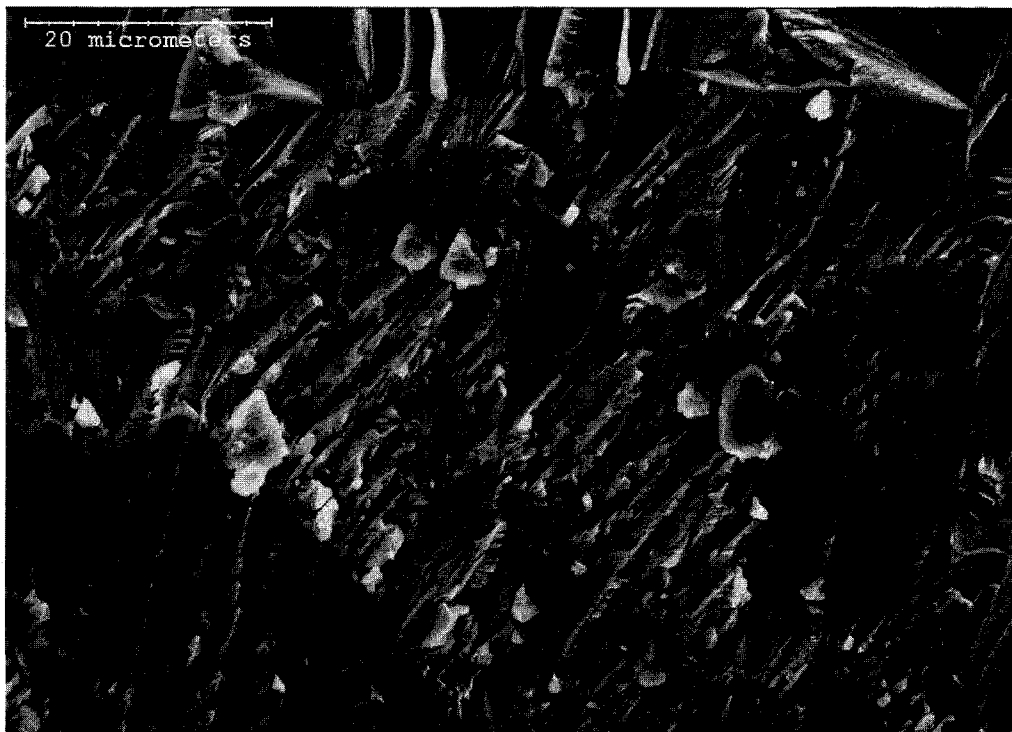
Figure 58: SEM Image of Alloy 1 Fracture Surface (air cooled) (SE)

114

5.3.1.2: Alloy 2 (NiAl + Cr + CeO$_2$)

Looking at the fracture surfaces in Figures 59, 60, and 61, it can be seen that the fracture behaviour goes from almost entirely intergranular in the 4-hour cooled case to about half intergranular in the air and 24-hour cooled cases. Figures 62 through 65 show cross-sections of partially compressed specimens containing cracks. In all of the figures, intergranular behaviour can be seen. One notable observation can be made when comparing Figure 62 and Figure 63. The first of these figures shows a cross-section compressed to 490 MPa, which shows grain boundary cracking almost exclusively. The second figure shows the same alloy after application of 520 MPa and along with the grain boundary cracking, transgranular cracks can be see. Figure 64 shows intergranular cracking in the 4-hour cooled alloy, while Figure 65 indicates both intergranular and transgranular cracking in the 24-hour cooled alloy.

Intergranular fracture faces are shown in Figures 66 though 70. In general, the intergranular fracture faces show both ceria and chromium as identified with EDX. The chromium seems to be associated with triangular prism-type protrusions from the grain surface, while the ceria is randomly scattered. Figure 68 shows heavy deposits of large-sized ceria particles.

115

Figure 59: SEM Image of Alloy 2 Fracture Surface (4-hour cooled) (SE)

Figure 60: SEM Image of Alloy 2 Fracture Surface (air cooled) (SE)

116

Figure 61: SEM Image of Alloy 2 Fracture Surface (24-hour cooled) (SE)

Figure 62: SEM Image of Alloy 2, 490 MPa Compression (air cooled) (SE, polished)

117

Figure 63: SEM Image of Alloy 2, 520 MPa Compression (air cooled) (SE, polished)

Figure 64: SEM Image of Alloy 2, 690 MPa Compression (4-hour cooled) (SE, polished)

118

Figure 65: SEM Image of Alloy 2, 670 MPa Compression (24-hour cooled) (SE, polished)
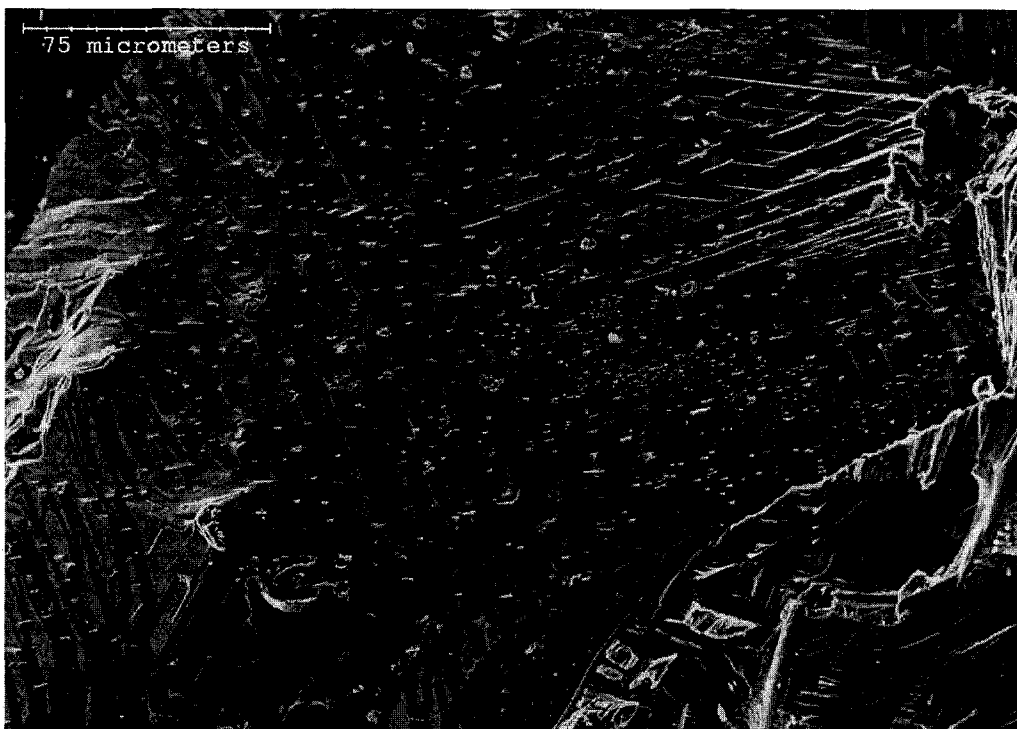
Figure 66: SEM Image of Alloy 2 Intergranular Fracture Surface (24-hour cooled) (SE)

119
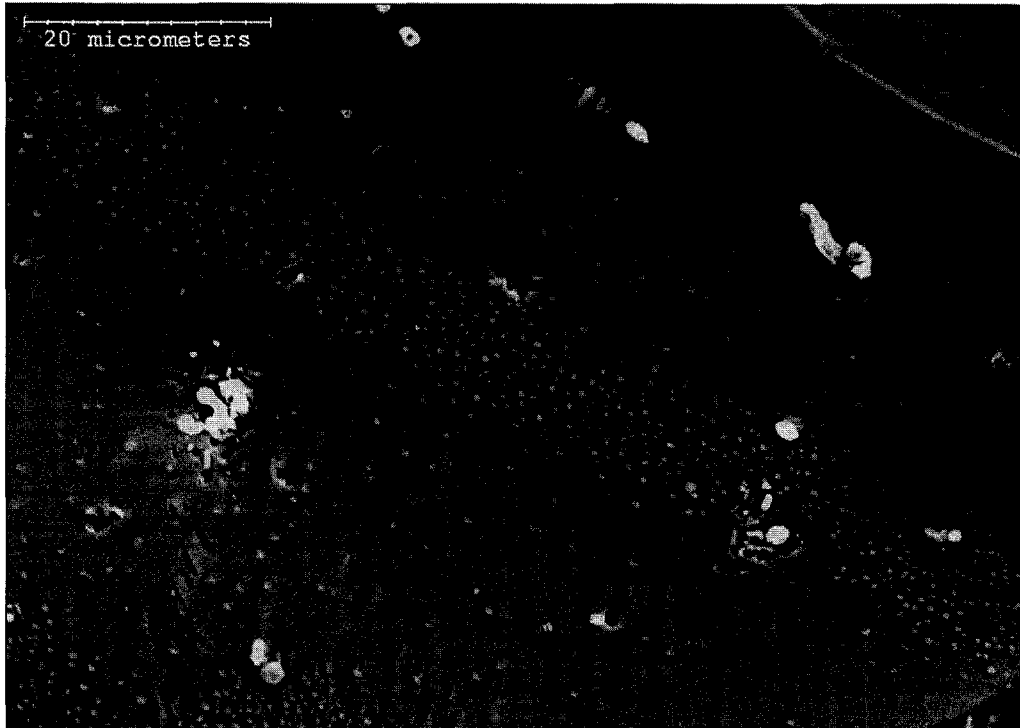
Figure 67: SEM Image of Alloy 2 Intergranular Fracture Surface (air cooled) (BSE)

Figure 68: SEM Image of Alloy 2 Fracture Surface with Ceria (air cooled) (BSE)

120

Figure 69: SEM Image of Alloy 2 Fracture Surface with Ceria and Chromium (4-hour cooled) (SE)
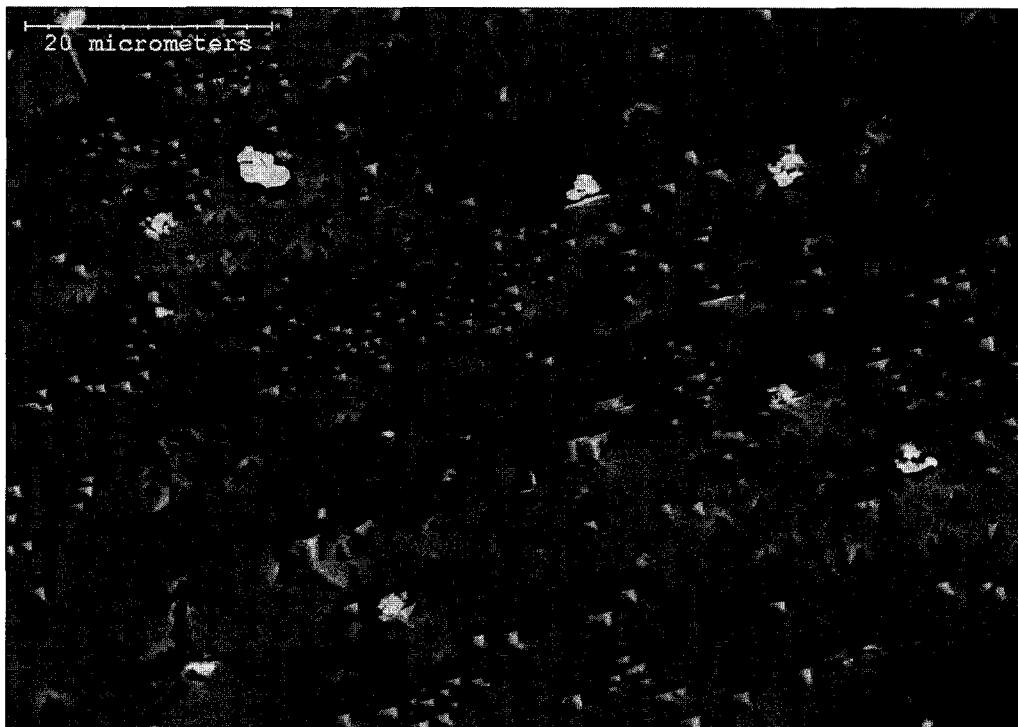
Figure 70: SEM Image of Alloy 2 Fracture Surface with Ceria and Chromium (24-hour cooled) (BSE)

121

5.3.1.3 Alloy 3 (NiAl + Ce)

Fracture faces for the air, 4-hour, and 24-hour cooled alloys are shown in Figures 71 to 73, respectively. A mix of intergranular and transgranular fractures are seen with the air cooled specimen exhibiting more intergranular mode than the 4 and 24-hour cooled conditions. Figure 74 shows a section of the 4-hour cooled alloy after 358 MPa of compression was applied. The intergranular preference at this load level is clearly shown with the crack making a nearly 90° turn from one grain boundary to another. Cerium or ceria deposits were found on all intergranular faces. Figure 75 shows an example in the air cooled specimen.

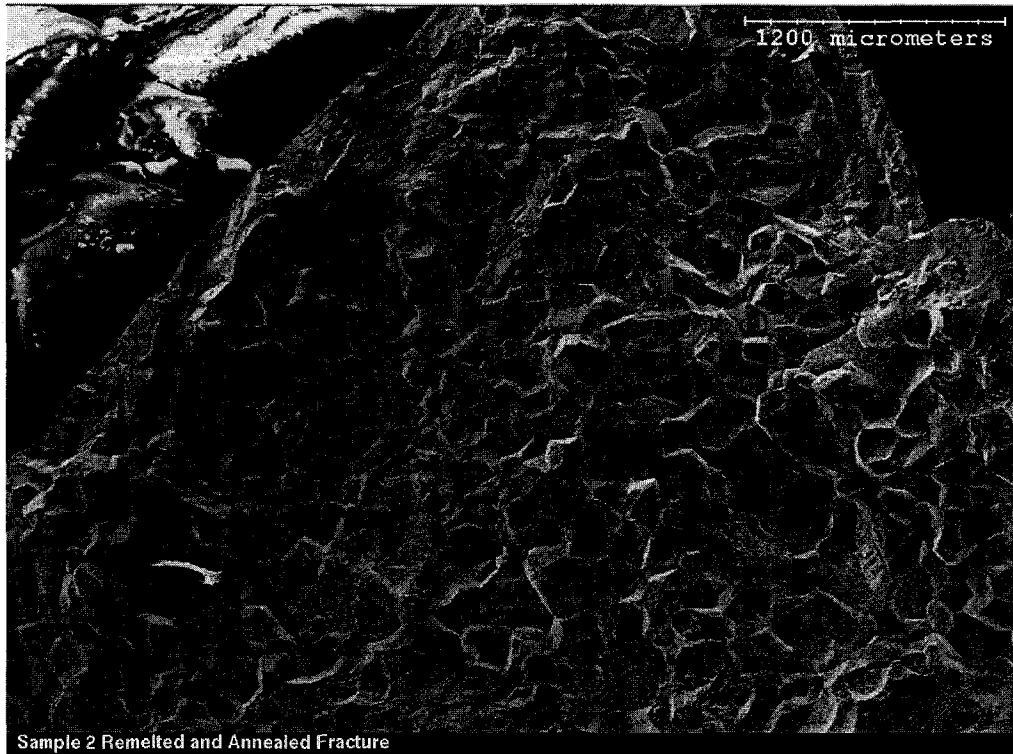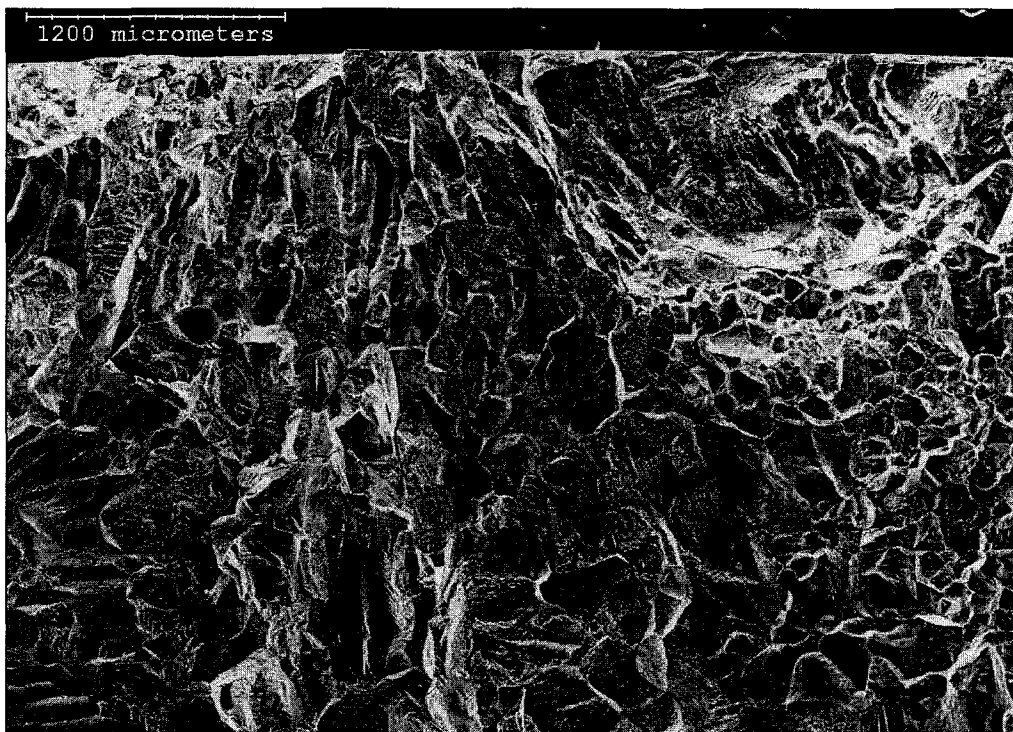**Figure 71: SEM Image of Alloy 3 Fracture Surface (air cooled) (SE)**

122

Figure 72: SEM Image of Alloy 3 Fracture Surface (4-hour cooled) (SE)

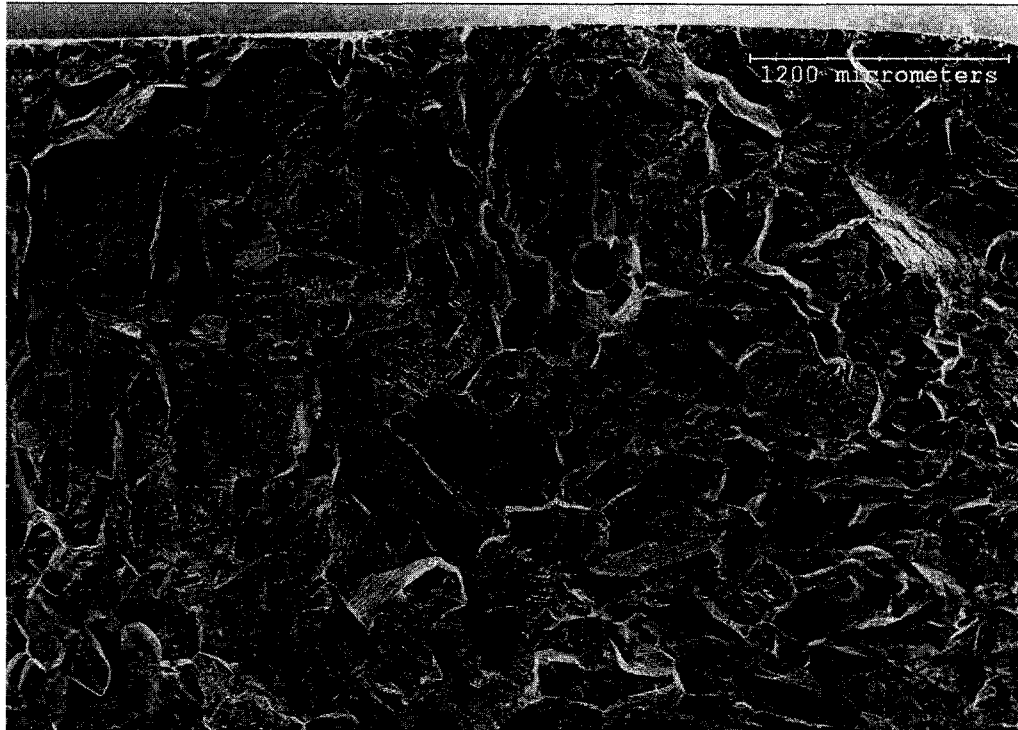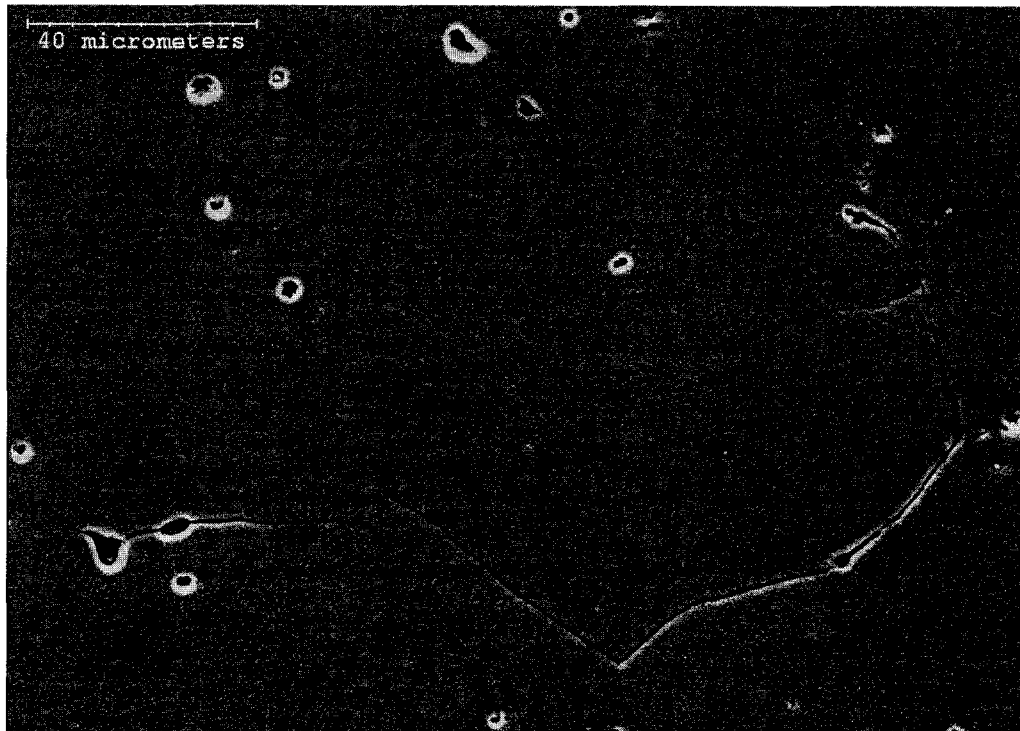**Figure 73: SEM Image of Alloy 3 Fracture Surface (24-hour cooled) (SE)**

123

Figure 74: SEM Image of Alloy 3, 358 MPa Compression (4-hour cooled) (SE, polished)
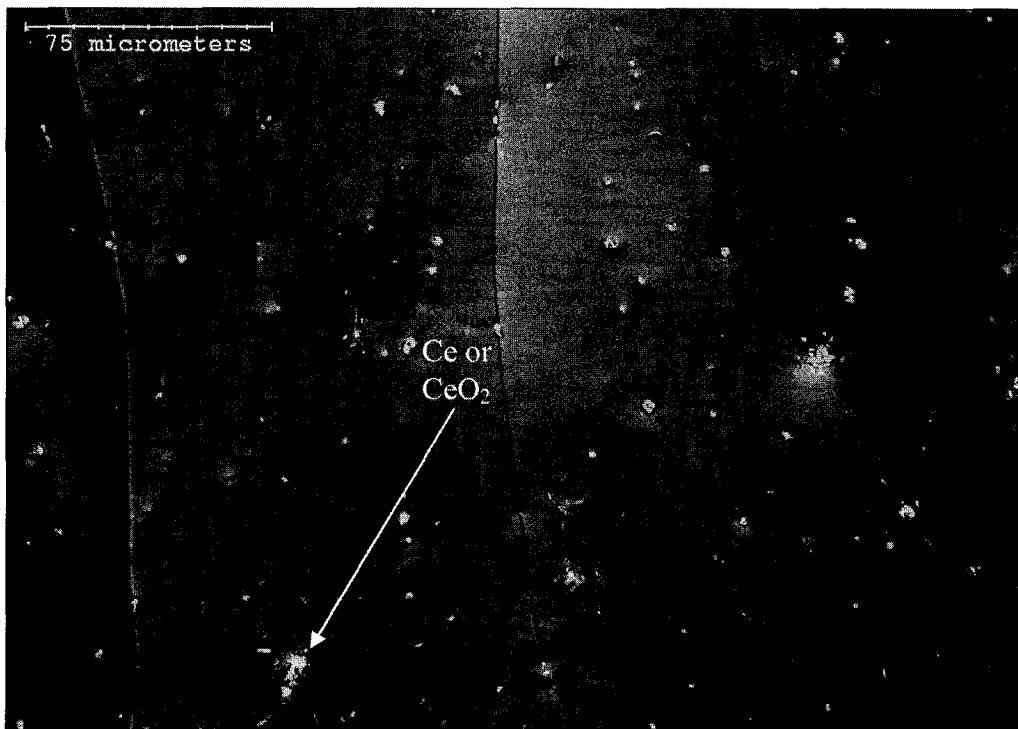
Figure 75: SEM Image of Alloy 3 Intergranular Fracture Surface (air cooled) (BSE)

124

5.3.1.4 Alloy 6 (NiAl + Cr + Ce)

Fracture faces are shown in Figures 76 to 78. Almost complete intergranular fracture behaviour can be seen in all conditions. Sections of the partially compressed specimens (Figures 79 though 81) also show almost exclusively intergranular fracture propagation. Higher magnification images of the intergranular surfaces, in Figure 82 through Figure 84 reveal high concentrations of chromium precipitates along with cerium or ceria on the grain boundary surfaces. There appears to be a higher concentration of chromium precipitates on the grain surface in the 24-hour cooled condition Figure 84 compared to the air-cooled alloy (Figure 82). In general, there appear to be higher concentrations of precipitates on the intergranular surfaces of alloy 6 than seen in alloy 2.
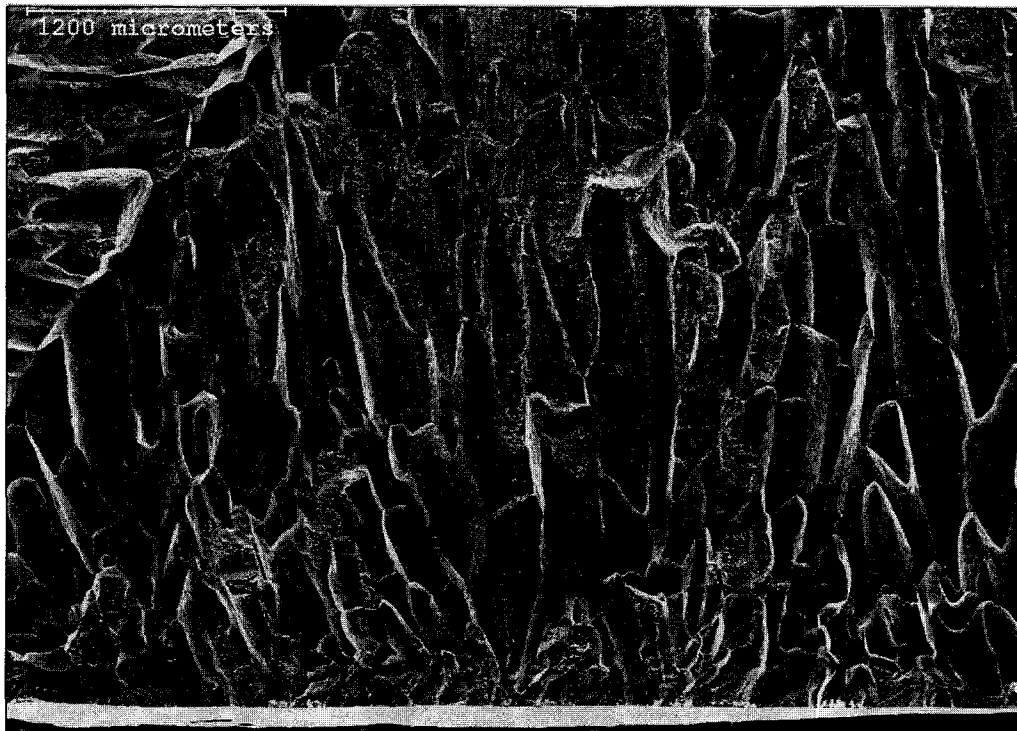
Figure 76: SEM Image of Alloy 6 Fracture Surface (air cooled) (SE)

125
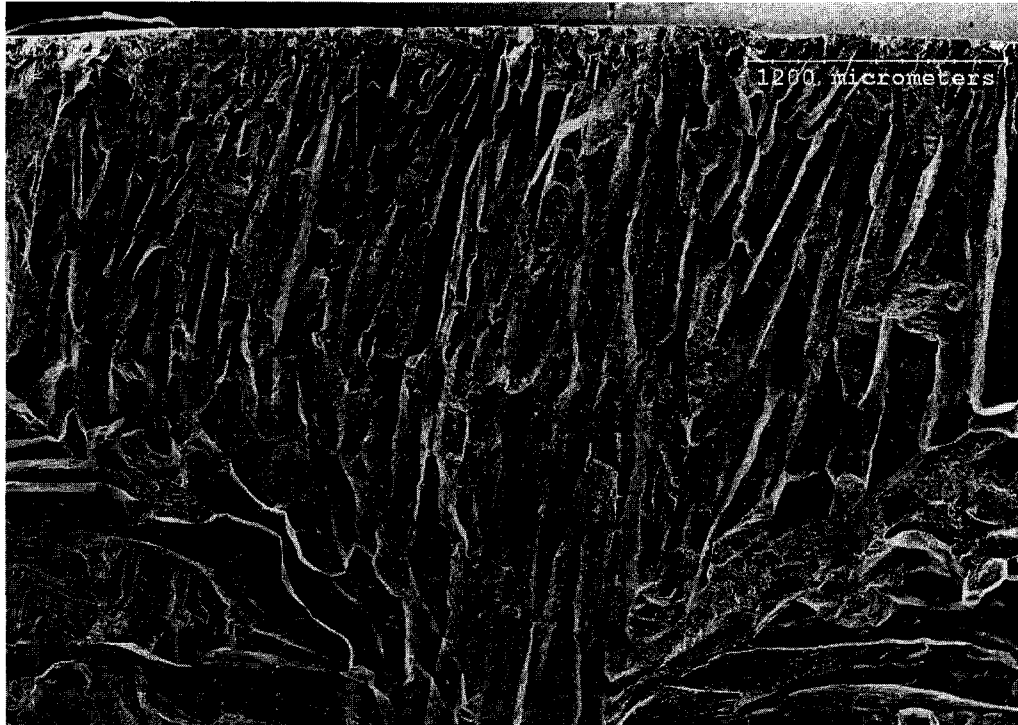
Figure 77: SEM Image of Alloy 6 Fracture Surface (4-hour cooled) (SE)

Figure 78: SEM Image of Alloy 6 Fracture Surface (24-hour cooled) (SE)

126

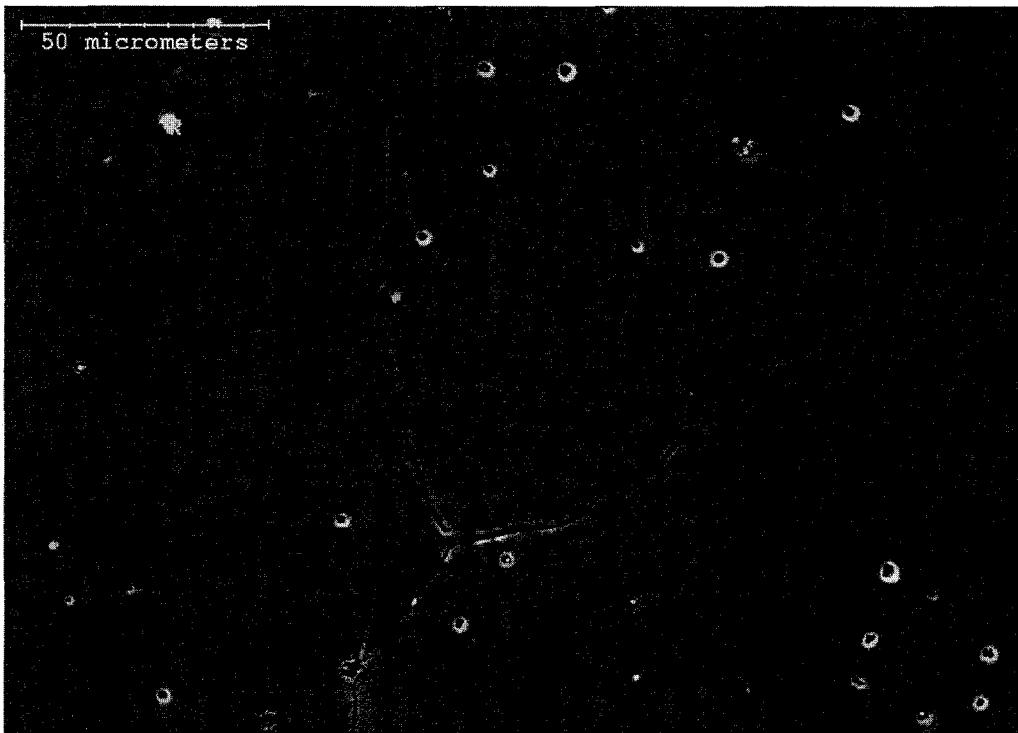**Figure 79: SEM Image of Alloy 6, 753 MPa Compression (air cooled) (SE, polished)**
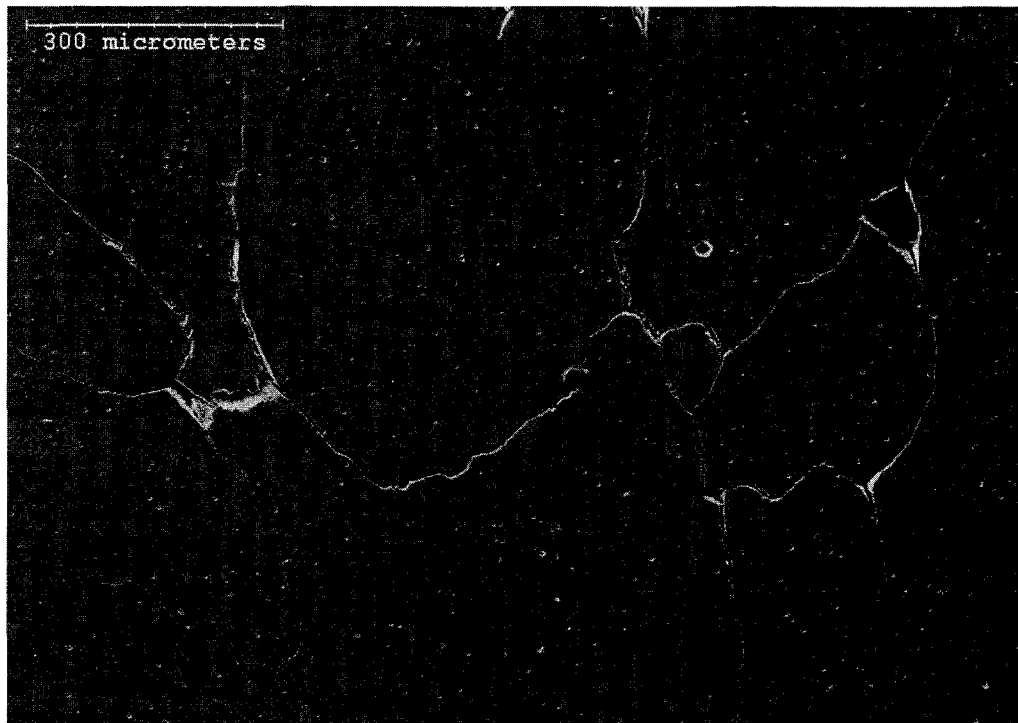
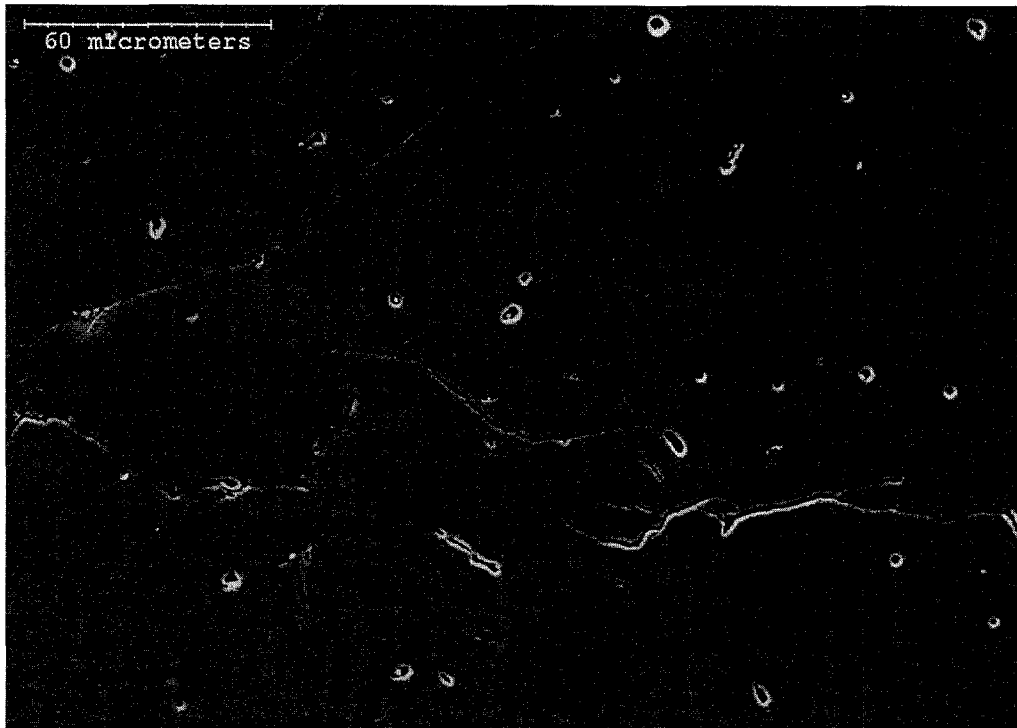**Figure 80: SEM Image of Alloy 6, 504 MPa Compression (4-hour cooled) (SE, polished)**

127
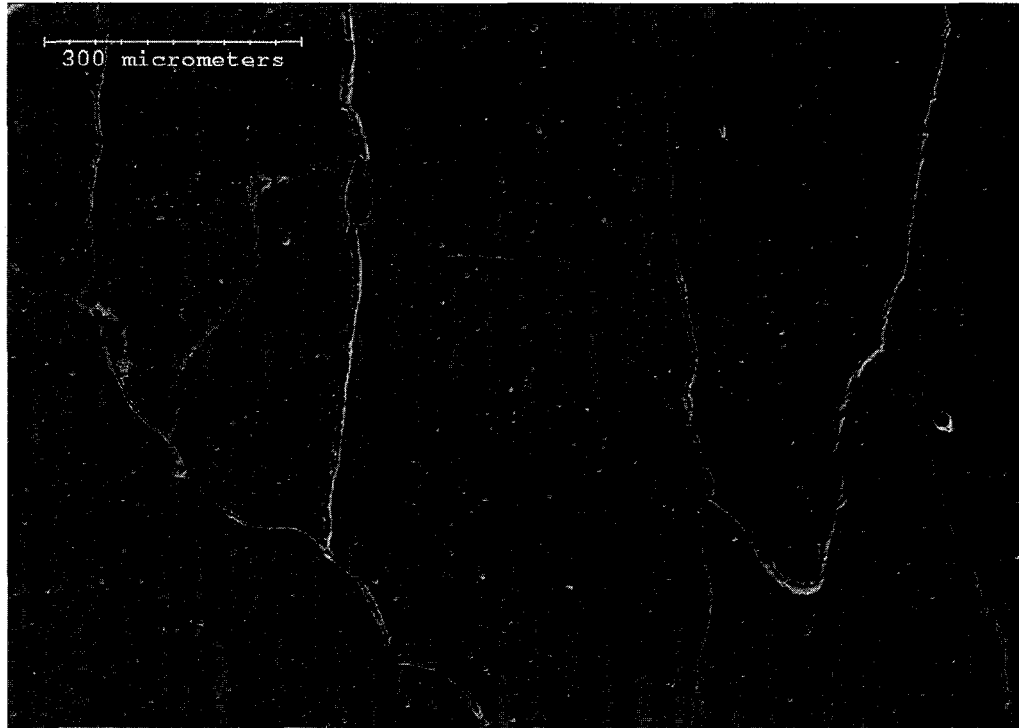
Figure 81: SEM Image of Alloy 6, 640 MPa Compression (24-hour cooled) (SE, polished)
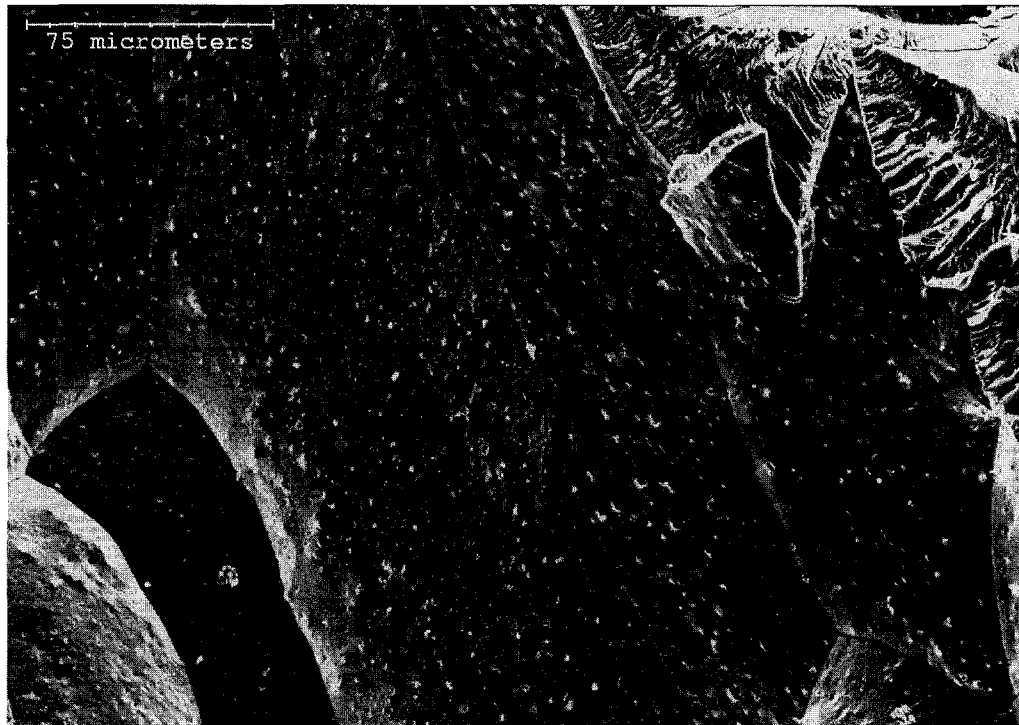
Figure 82: SEM Image of Alloy 6 Intergranular Fracture Surface (air cooled) (SE)

128
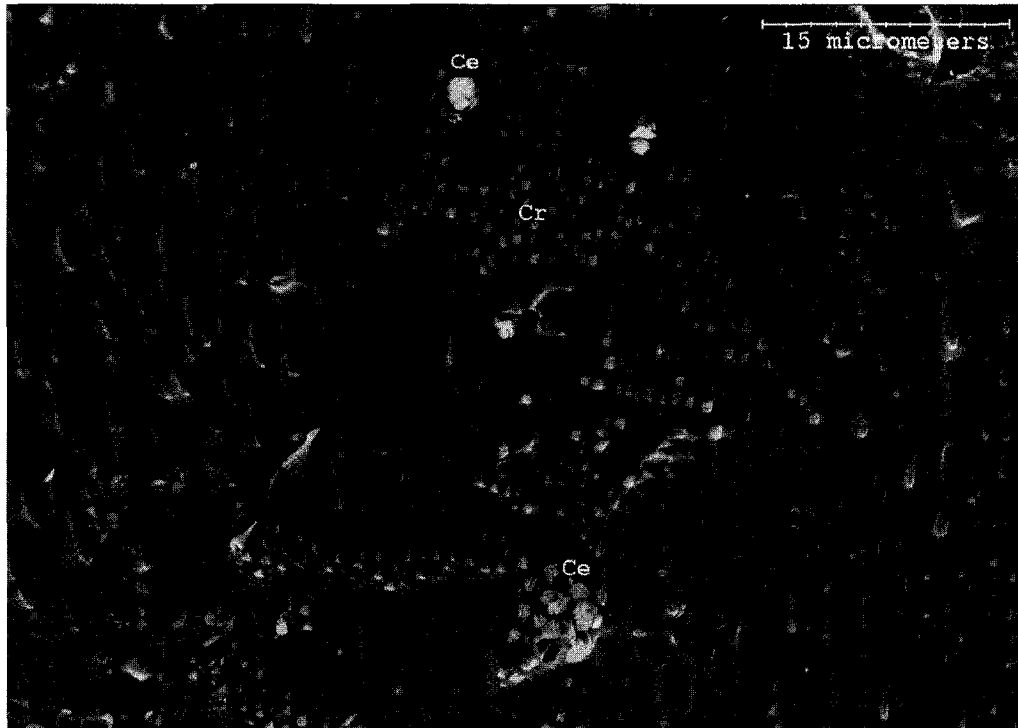
Figure 83: SEM Image of Alloy 6 Intergranular Fracture Surface (4-hour cooled)
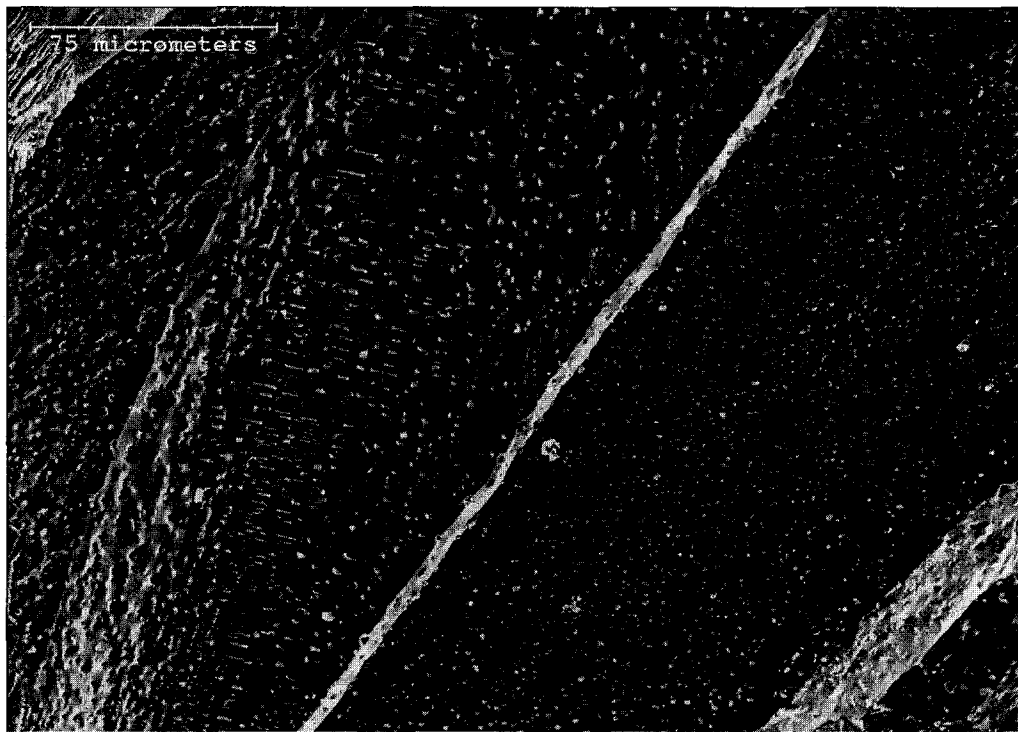
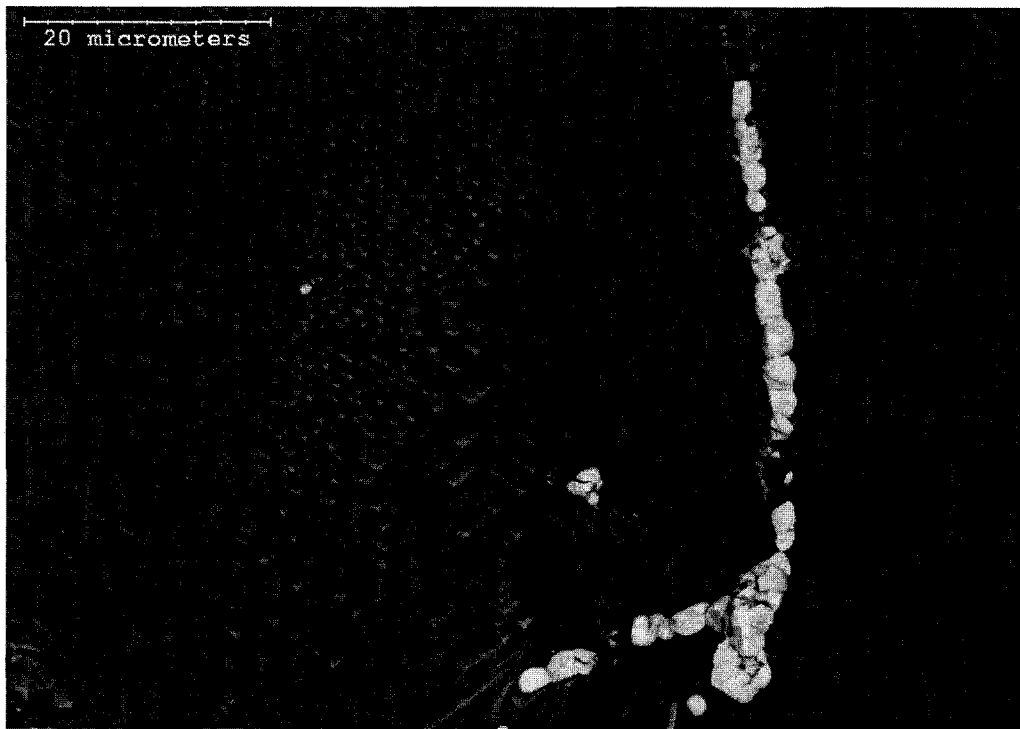**Figure 84: SEM Image of Alloy 6 Intergranular Fracture Surface (24-hour cooled) (SE)**

129

5.3.1.5 Alloy 8 (NiAl + Cr + CeO₂)

Fracture surfaces of the air, 4-hour, and 24-hour cooled alloys are shown in Figures 85 to 87, respectively. Transgranular fracture behaviour can be seen in all three cases with some secondary cracks intersecting the primary crack face. The polished section in Figure 88 shows a combination of intergranular and transgranular fracture paths. Of note are the long transgranular cracks that are aligned vertically. This section is of a 4-hour cooled alloy compressed to 812 MPa. Small portions of intergranular fracture surface were located in all three of the alloys and are displayed in Figures 89 though 91. These intergranular surfaces contain chromium precipitates as well as ceria particles similar to alloys 2 and 6. Figure 92 shows an intergranular fracture surface in the 24-hour cooled alloy at intermediate magnification for comparison with images of alloys 2 and 6. There appear to be much finer precipitates on the intergranular surfaces of alloy 8 compared with alloys 2 and 6.
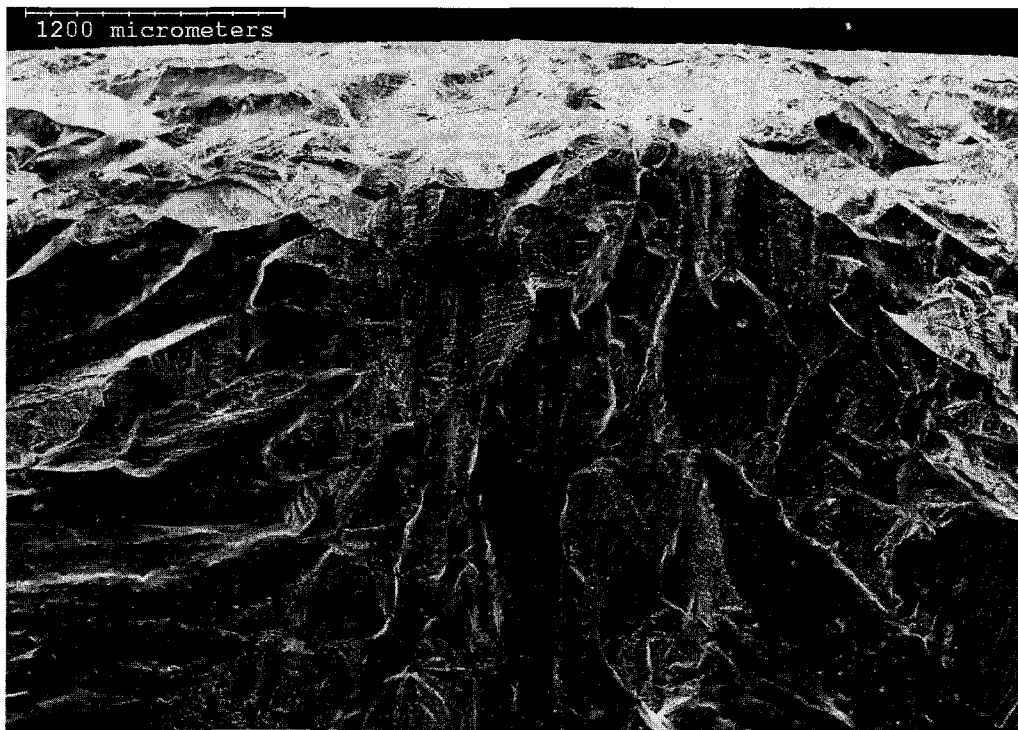
130
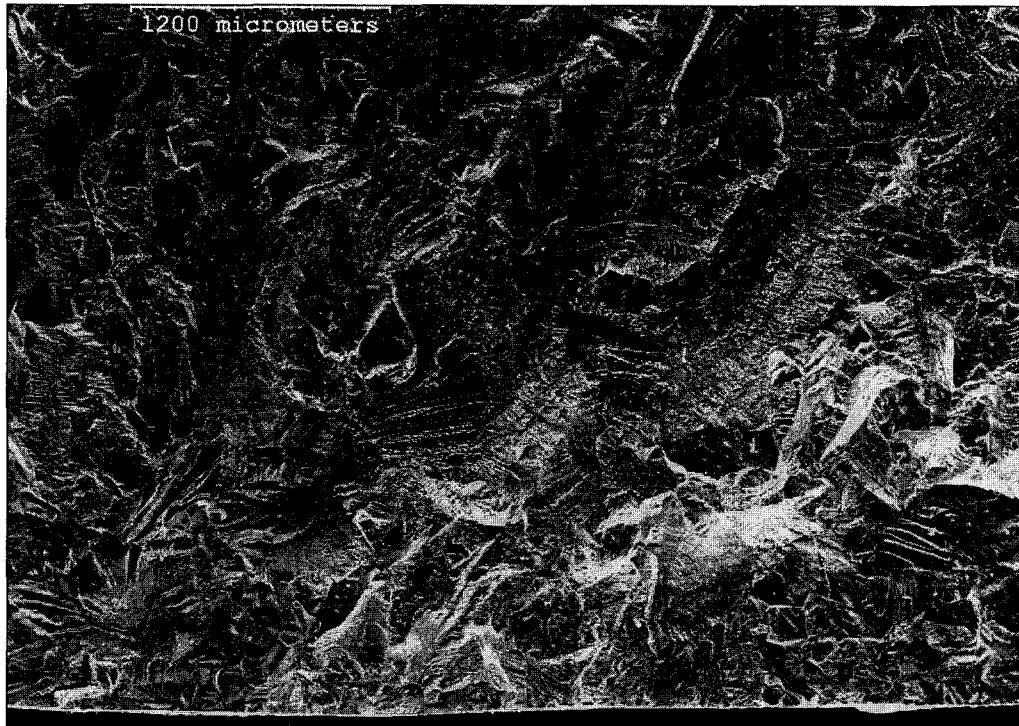
Figure 85: SEM Image of Alloy 8 Fracture Surface (air cooled) (SE)
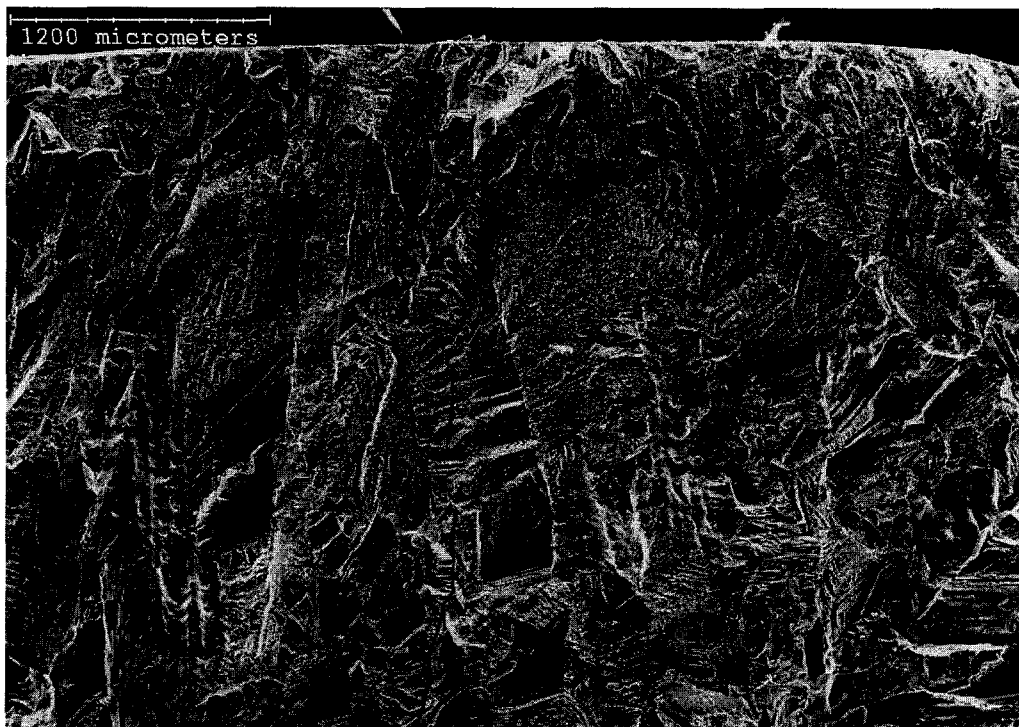
Figure 86: SEM Image of Alloy 8 Fracture Surface (4-hour cooled) (SE)
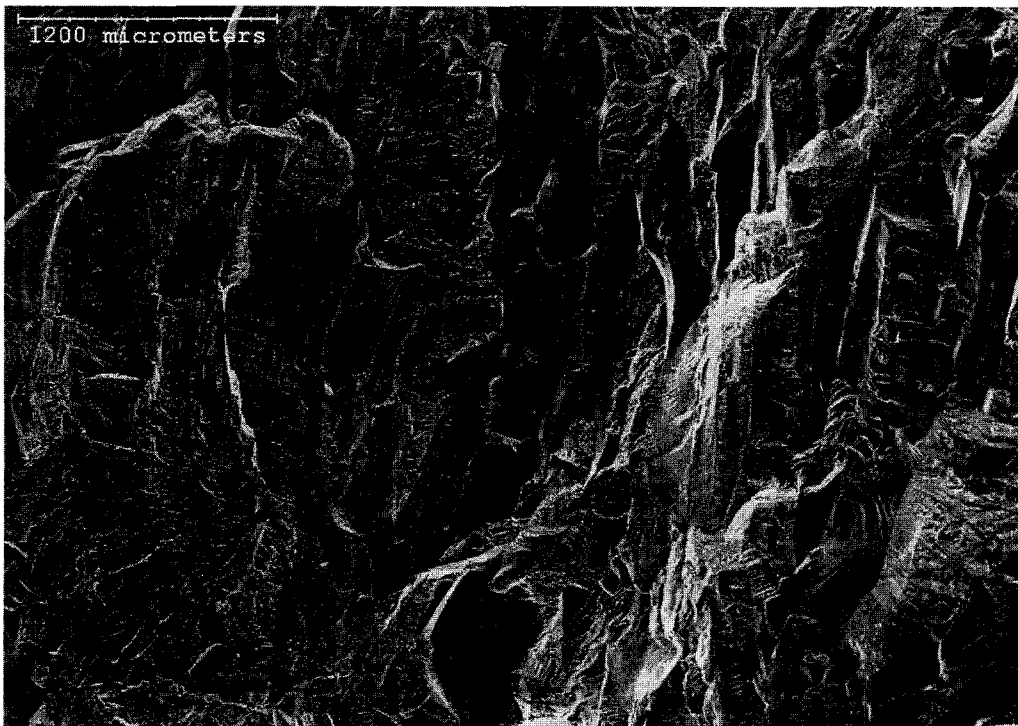
131
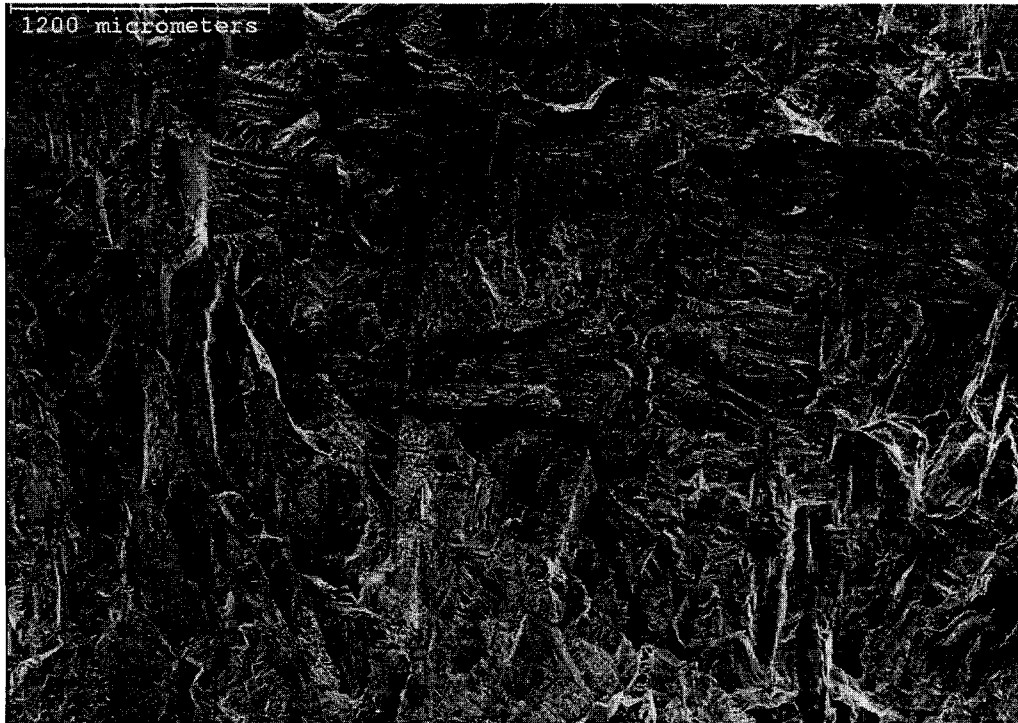
Figure 87: SEM Image of Alloy 8 Fracture Surface (24-hour cooled) (SE)
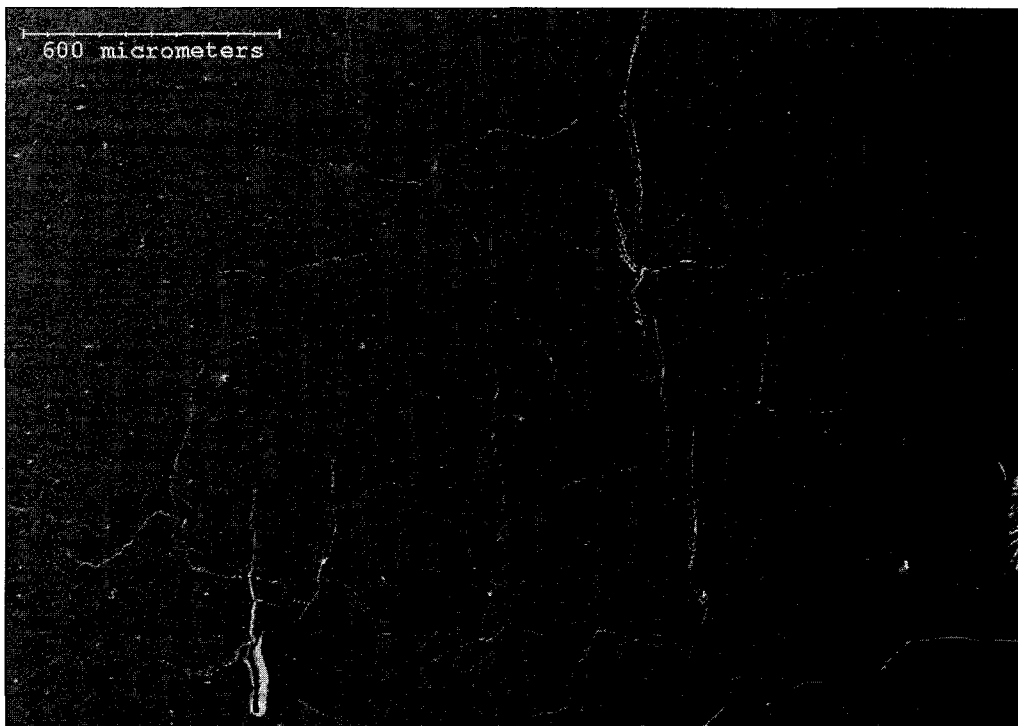
**Figure 88: SEM Image of Alloy 8, 812 MPa Compression (4-hour cooled) (SE, polished)**

132
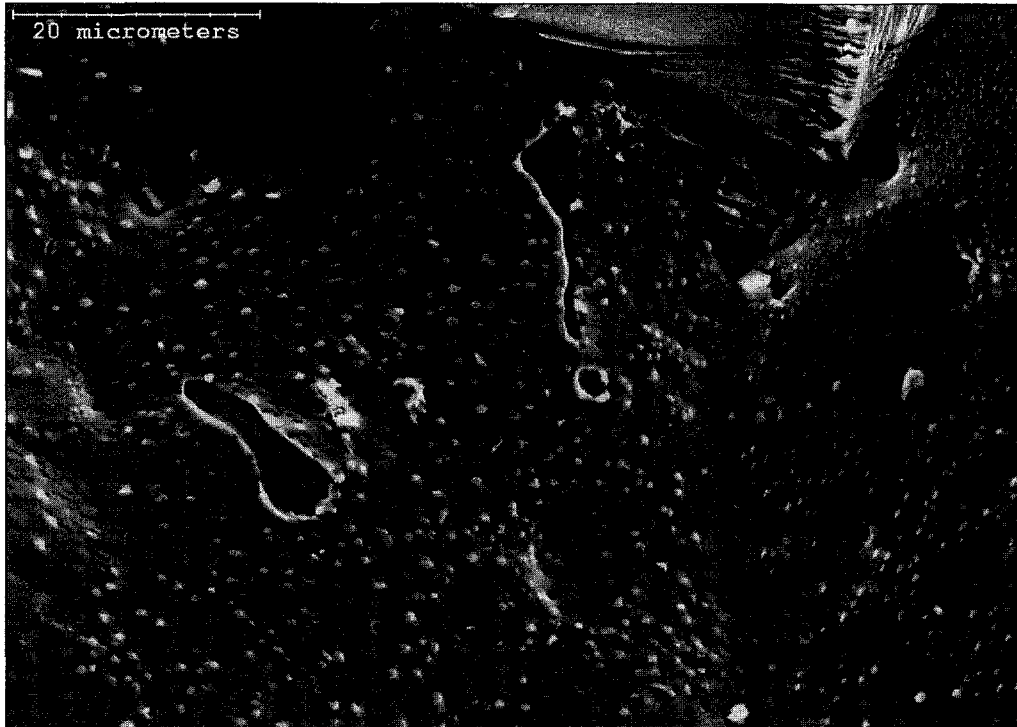
Figure 89: SEM Image of Alloy 8 Intergranular Fracture Surface (air cooled) (SE)
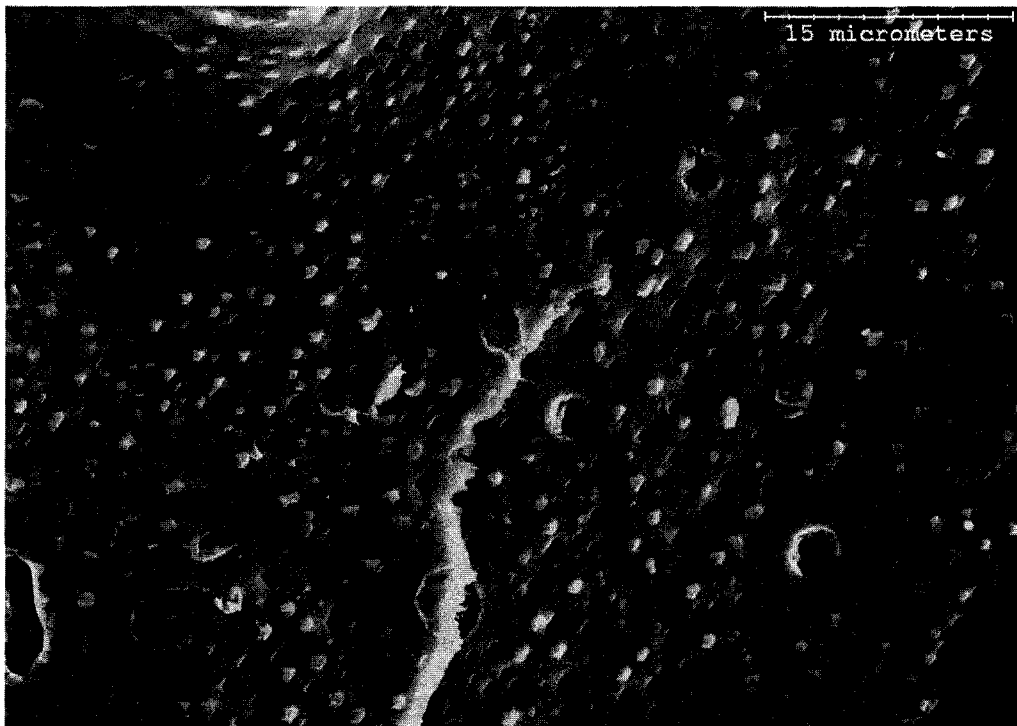
Figure 90: SEM Image of Alloy 8 Intergranular Fracture Surface (4-hour cooled) (SE)

133
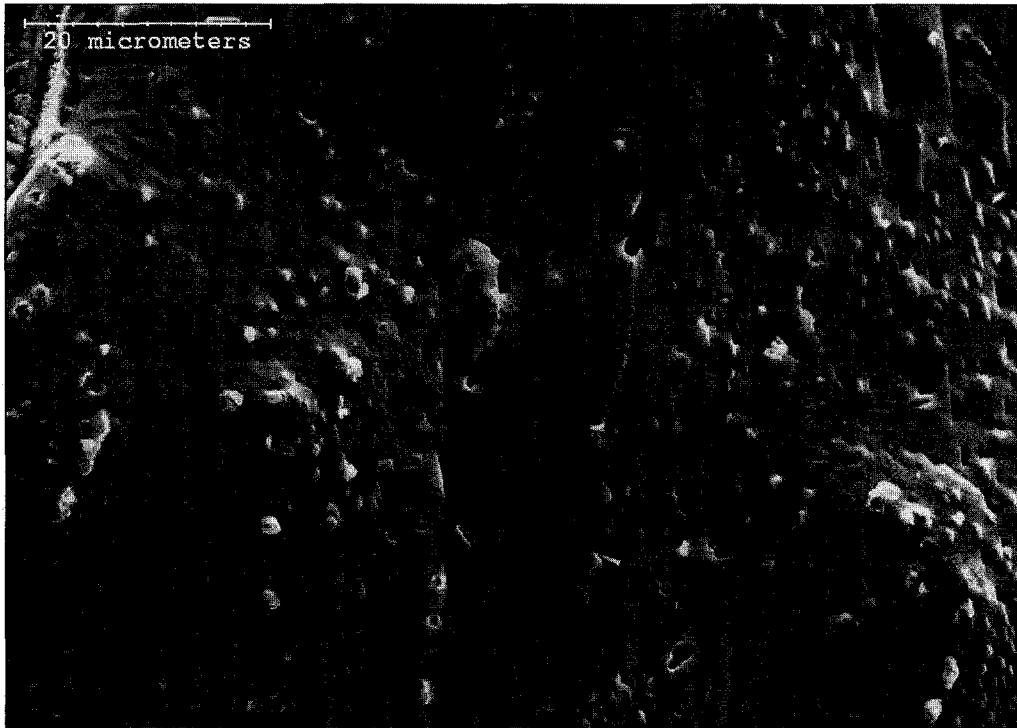
Figure 91: SEM Image of Alloy 8 Intergranular Fracture Surface (24-hour cooled) (SE)
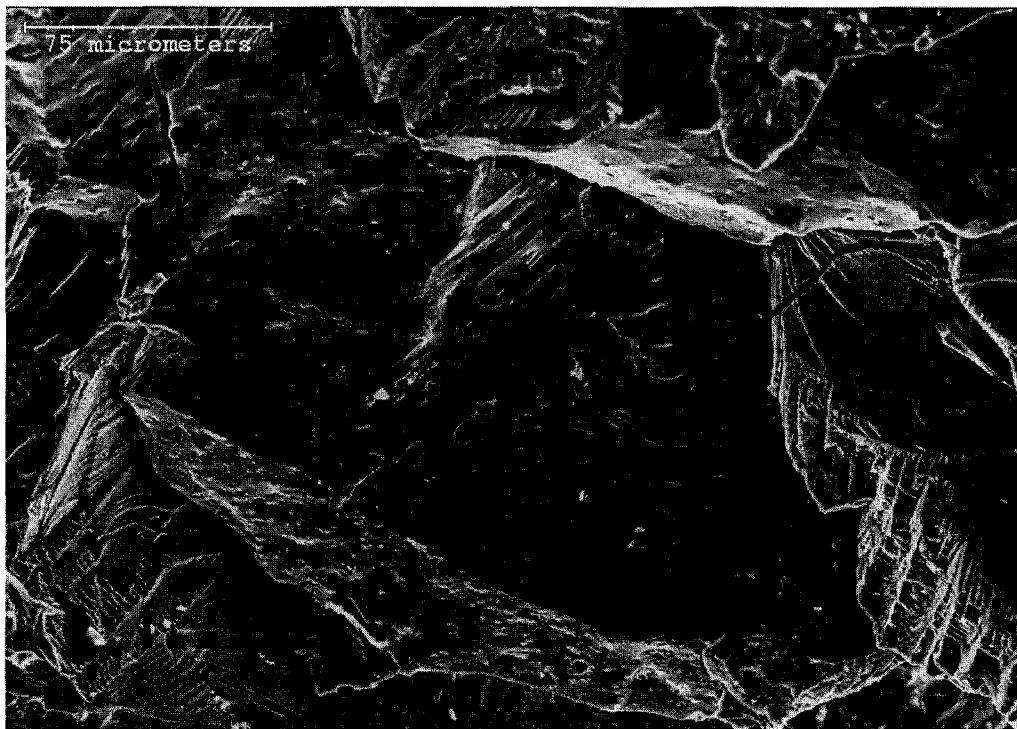
Figure 92: SEM Image of Alloy 8 Intergranular Fracture Surface (24-hour cooled) (SE)

134

5.3.2 Fracture Discussion

A summary of the observed fracture modes seen in the simulated and compressive fracture study are presented in Table 7. The percentage of intergranular (IG) or transgranular (TG) fracture has been approximated for the simulated fracture columns. For the compressive fracture columns, IG or TG are used when there are only single mode cracks seen, while IG/TG is used when both types of cracks are present.

Table 7: Fracture Mode Summary

Alloy	Al/Ni Fraction	Simulated Fracture			Compressive Fracture		
		Air	4 Hour	24 Hour	Air	4 Hour	24 Hour
1 (NiAl)	0.99	TG	TG	TG	NA	TG	NA
2 (NiAl + CeO$_2$ + Cr)	0.99	50% IG	IG	50% IG	IG/TG	IG/TG	IG/TG
3 (NiAl + Ce)	0.99	75% IG	30% IG	40% IG	NA	IG	NA
6 (NiAl + Ce + Cr)	1.03	IG	IG	IG	IG	IG	IG
8 (NiAl + CeO$_2$ + Cr)	1.02	TG	TG	TG	NA	IG/TG	TG

In an attempt to compare the ductility and fracture mode, the peak strain results from compression testing should be considered along with the fracture mode seen in the partially compressed specimens. A summary of the fracture mode versus peak strain and stress is shown in Table 8. Along with the peak strain, the peak stress must be considered. We accept that pure NiAl should fracture in an intergranular manner from slip incompatibility. Grain boundary weakening or embrittlement from second phase particles could also result in intergranular fracture, but at a much lower stress and strain.

135

Table 8: Fracture Mode versus Peak Strain and Stress Summary

Alloy	Fracture Mode	Peak Strain	Peak Stress
1	TG	0.105	937
2	IG/TG	0.118	1018
3	IG	0.028	488
6	IG	0.086	769
8	IG/TG	0.097	848

5.3.2.1 Transgranular Fracture in Commercially-Pure NiAl (Alloy 1)

The observation of transgranular fracture in alloy 1 under all cooling conditions is somewhat contrary to established literature [47, 48, 50, 65, 69, 75]. Intergranular fracture due to slip incompatibility is generally accepted as the fracture mode of stoichiometric NiAl. Transgranular fracture is said to occur with deviation from stoichiometry [19, 50] or with almost any hardening alloy addition, with the exception of carbon or beryllium [66]. It has also been stated that large grain sizes, high strain rates, or notch effects can lead to transgranular fracture [24, 113].

The most likely reason for the observed transgranular fracture would be stoichiometry. The aluminum-to-nickel fraction for alloy 1 was measured to be 0.99, which would not likely result in a change in fracture mode. The grain size of the tested alloy was in the range of approximately 300 μm. The majority of the research done on NiAl is in the extruded condition, which results in grain sizes around 30 μm. Work by Nagpal and Baker [49] has suggested that the ductility of NiAl dramatically decreases with increasing grain size (ie. From 30 to 275 μm). The same result was found earlier by Grala [47]. It is possible that a larger grain size will lead to fracture inside the grain due to dislocation

136

interactions with other sessile dislocations or dislocation tangles. In the case of smaller grains, the dislocations may be more likely to travel to the grain boundaries where they then pileup and lead to intergranular fracture. There is evidence that suggests that increased strain rate increases the propensity for transgranular fracture [50]. Although this behaviour is understandable, transgranular fracture was seen in both the impact fractured and partially compressed specimens. The impact fractured specimens had a very high strain rate, while the partially compressed specimens were strained at a rate of $1 \times 10^{-3} s^{-1}$. Since there is clearly transgranular fracture in both cases, the strain rate must not be responsible.

5.3.2.2 Metallic Cerium Addition (Alloy 3)

Alloy 3 displayed a combination of transgranular and intergranular fracture. There seemed to be a greater degree of intergranular fracture in the air and 24-hour cooled conditions compared to the 4-hour cooling. Unfortunately, there is a significant difference in the grain structure between the different cooling conditions. Both the air and 24-hour cooled alloys show a dendritic grain structure characteristic of preferred growth, while the 4 hour cooled alloy shows a more equiaxed grain structure. Figure 93 shows the grain structure of the ingots from which the compression specimens were cut. Research conducted by Kim, Hong, and Lee [114] indicates a strong relationship between the fracture mode and orientation of neighbouring grains. In the case of the dendritic grain structure, the distribution of high and low angle grain boundaries might be significantly different than for the equiaxed grain structure.

137

Because the preference between intergranular and transgranular fracture does not seem to be very strong, the strain rate might play a significant role. While the impact fractured specimens seem to be mixed mode, the partially compressed samples show almost all intergranular fracture paths. It is clear that the intergranular surfaces are covered in ceria or cerium which would not be expected to strengthen the grain boundaries. If the cerium were oxidized to produce ceria, an increase in intergranular nature might be expected due to the brittle nature of the oxide. The mixed fracture behaviour is probably a result of the slight deviation from stoichiometry and could be further promoted by the high strain rate in the impact fractured samples.

138
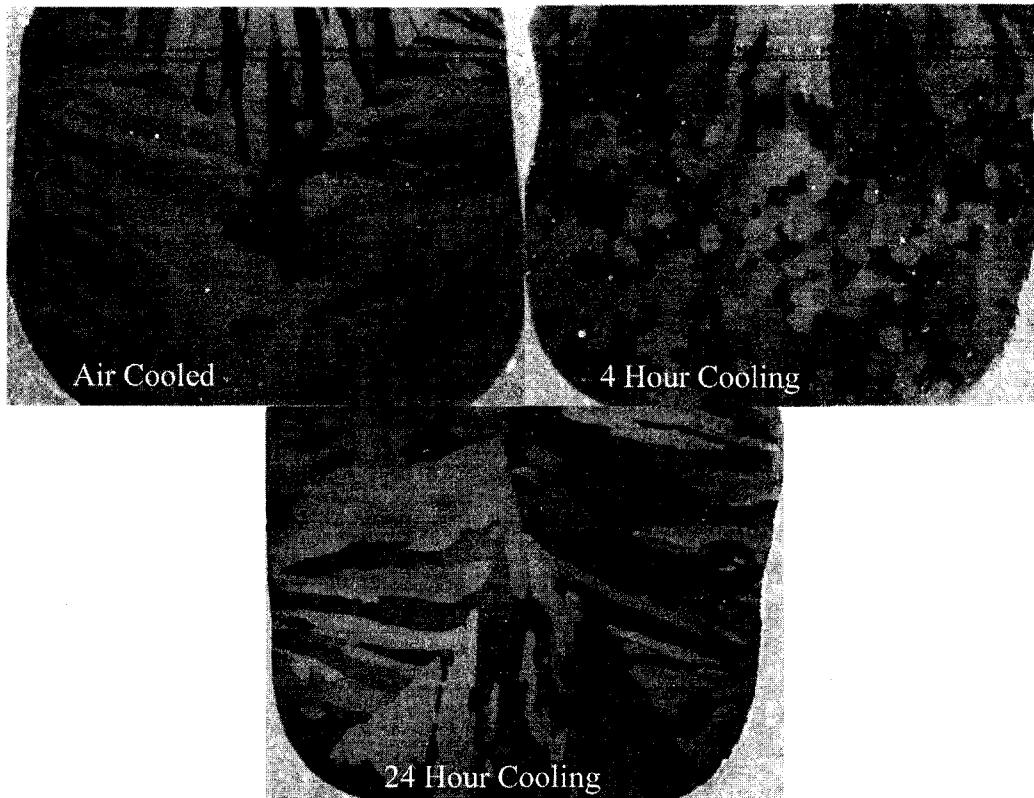
Figure 93: Optical Macro-Graphs of Alloy 3 As-Melted Ingots

5.3.2.3 Chromium Containing Alloys (Alloys 2, 6, and 8)

Alloys 2, 6, and 8 were similar in that they all contain both cerium or ceria and chromium. Ceria powder was added to alloys 2 and 8, while metallic cerium was added to alloy 6. It is interesting to note that alloys 2 and 6 both show mainly intergranular failure, while alloy 8 portrays almost complete transgranular behaviour. It has previously been found that chromium addition to NiAl results in a shift from the normal intergranular to transgranular fracture [19, 50, 99]. It was suggested that dislocation solute or precipitate interactions could generate cleavage fractures in the grain interior. In light of these findings, it is unexpected that intergranular fracture would occur in these chromium-containing alloys. A possible explanation for this would be if the grain boundaries were compromised

139

in some way. Looking at the intergranular surfaces of alloys 2, 6, and 8, many chromium precipitates can be seen (Figures 68, 70, 82, 84, 89, and 92). Alloy 6, in particular, has a large number of precipitates visible. The existence of these precipitates could compromise the cohesion of the grain boundary interface. If this were the case, similar behaviour would be expected in all three alloys. The only difference between the three alloys is with the cerium or ceria content. As was mentioned in the experimental procedure section (Section 3), only trace ceria is present in alloy 8. Chemical analysis showed no cerium content, but both metallography and fractography indicate its presence. There seems to be more difficulty in locating ceria particles on the fracture surfaces of alloy 8 than on alloys 2 or 6. The correlation between ceria content and fracture mode might suggest that too much ceria can compromise grain boundary integrity, making intergranular fracture easier. In this scenario, alloys 2 and 6 would form intergranular cracks before significant transgranular cracking occurred. These intergranular cracks would limit the ability for the transgranular cracks to propagate and cause failure. If the grain boundaries were stronger, with less ceria, there would be fewer intergranular cracks to stop transgranular propagation.

5.3.2.4 General Fractographic Discussion

Considering the results of this fractographic study, relevance to the results of the mechanical testing must be discussed. In general, alloys 1 (NiAl) and 8 (NiAl + ppm CeO_2 + Cr) fail by transgranular fracture, while alloy 6 (NiAl + Ce + Cr)

140

fails in an intergranular nature. Alloys 2 (NiAl + CeO$_2$ + Cr) and 3 (NiAl + Ce) demonstrate mixed mode failure.

The fact that alloy 6 failed at lower stress and strain levels could be justified by the highly intergranular fracture behaviour observed. This would suggest that the grain boundaries were in some way weakened, leading to premature fracture. As was mentioned before, intergranular fracture would not be expected in an alloy with such elevated hardness. The strongly intergranular nature of alloy 6 paired with the lower fracture strain compared with alloy 2 suggests that there may be a detrimental effect from metallic cerium addition.

Looking again at the compression curve of alloy 3, failure at low load and strain levels was noted. Although mixed mode failure was demonstrated in the impacted samples, the lower strain rate of compression testing could have lead to a mainly intergranular failure mechanism. Considering this intergranular fracture mode and the low stress and strain at failure, it would appear that the metallic cerium has resulted in grain boundary embrittlement.

A comparison of the fracture behaviour of alloys 2 and 6 over the three different cooling conditions shows a higher affinity for intergranular fracture in alloy 6. Although the 4-hour cooled condition for alloy 2 indicated mainly intergranular behaviour, the air and 24-hour cooling were mixed mode. In light of this, the differences in cooling rate versus compressive behaviour between alloys 2 and 6

141

might be understandable. The trend of the 4-hour cooled condition having higher hardness was identified first and is a matrix property. If the alloys were then to cleave in the grain from deformation resistance, the effect might be expected to manifest itself in the compression curves that we see in alloy 2.On the other hand, if the grain boundaries were to fracture at an early stage because of embrittlement, the trend might not present itself in the compression results. This might explain why the trend was not clearly seen in alloy 6.

6.0 General Discussion

Comparing the results from testing on the investment cast material (Section 4) with that of the re-melted material (Section 5) reveals some remarkable points. The hardness testing results are slightly harder for the re-melted material. As discussed previously, this could result from a decrease in the aluminum-to-nickel fraction due to aluminum loss during re-processing.

Compression testing results show significant differences. Alloys 2 and 6 showed drastically different behaviours from the other alloys in the investment cast material, while there was much less difference in the re-melted condition. The interesting effect from the combination of ceria or cerium and chromium seen in the investment cast material is nearly absent. While being of similar strength to alloys 1 and 8 in the investment cast material, alloy 3 fails at a significantly lower load in the re-melted condition. These differences in compressive behaviour could be a result of a number of variables including aluminum-to-nickel fraction and interstitial content.

Another key observation that has not been addressed to this point is the difference in aluminum-to-nickel fraction from the investment cast material to the re-melted material. The aluminum content of the alloys relative to the other constituents seems to have increased. This is very unlikely because of the high vapour pressure of aluminum over molten NiAl. It would be more likely that the aluminum-to-nickel fraction would remain the same or decrease. There is

143

sufficient evidence from the test data to bring the tested chemical composition of the re-melted alloys into question. If the aluminum-to-nickel fraction of the re-melted, commercially-pure NiAl alloy were closer to the 0.90 fraction of the investment cast material, the transgranular fracture mode and high strength would be justified.

A possible explanation for the degradation of alloys 3 and 6, both containing metallic cerium, from the investment cast to re-melted material involves oxidation. Through the process of re-melting and homogenizing, the metallic cerium may have either become oxidized or reacted with other elements, resulting in embrittlement of the grain boundaries. Because of its highly reactive nature and low melting temperature, cerium would never be a stable alloy addition for NiAl.

With respect to the ductility of the alloys investigated, the fractographic study has revealed some important information. As shown in the compression testing results, the ductility of alloy 2 (NiAl + CeO_2 + Cr) in the re-melted material and both alloys 2 and 6 (NiAl + Ce + Cr) in the investment cast material appeared to be significantly higher than the other alloys. Unfortunately, evidence of intergranular cracks in the partially compressed specimens from these and all of the alloys at low load levels indicates that any apparent ductility includes fracture propagation. In a tensile test, the first crack would grow to a critical length and cause failure well before yield.

144

One thing that would indicate that there is still potential for combined ceria and chromium additions to increase the ductility of NiAl would be if small cracks were already present in the alloys from processing. We have seen that there were casting defects in the re-melted material. If the castings were free of these, early fracture would possibly be avoided.

145

7.0 Conclusions

The effect of chromium and cerium as well as ceria additions to NiAl was investigated. Findings do not indicate any increase in the ductility of NiAl from the combined addition of cerium or ceria with chromium. Metallographic and fractographic characterization was conducted in addition to hardness and compression testing. The effect of cooling rate from the homogenization temperature was considered with respect to hardness, compression behaviour, and fracture mode. The following were the key conclusions of this investigation:

- The combination of chromium and ceria to NiAl resulted in a shift of the fracture mode from purely intergranular to a mixed mode with 0.02 at.% Ce content (analyzed from ceria addition). When less than the detectable limit of cerium (from ceria) was present, a transgranular fracture mode persisted.

- Addition of metallic cerium to NiAl, with or without chromium, resulted in grain boundary embrittlement leading to premature intergranular fracture after re-melting.

- An effect of the cooling rate from the homogenization temperature was seen in the hardness and compression test results of alloy 2 (NiAl + CeO_2 + Cr). Cooling over 4 hours resulted in higher hardness, peak stress, and peak strain compared to the samples cooled with forced air or over 24 hours.

146

- Evidence of intergranular and/or transgranular fracture was found at low loads in all the partially compressed samples. This indicates that the apparent ductility seen in compression test results involved fracture propagation and cannot be called ductility.

147

8.0 Future work

One item that was missing from this research was a control alloy that contained only chromium. In this way, one would be better able to discover the effect of cerium / ceria with chromium. Better control of the aluminum-to-nickel fraction would be absolutely necessary for further research because of the overwhelming effect of small deviations from stoichiometry. As well, proper comparison of alloys requires tight control of grain structure, which is difficult with arc-melting. For this, investment casting is more consistent, but the casting parameter would have to be altered to ensure sound casting that is free of cracks. If the production of sound castings were not possible via investment casting, hot extrusion might have to be employed. Finally, because of the potent nature of interstitial elements (mainly carbon and boron), alloys with as little interstitial content as possible would be desirable.

In particular, recommendations for future work would include the following:

- Addition of only 1% Cr to ensure solid solution and avoid the complication of precipitation.

- Addition of different amounts and particle sizes of ceria.

- Addition of ceria and chromium to a range of aluminum-to-nickel fraction alloys.

- Utilization of TEM to positively identify precipitates and possibly investigate dislocation phenomena.

148

REFERENCES

Literature Cited

1. Nash, P., M.F. Singleton, and J.L. Murray, *Al-Ni (Aluminum - Nickel)*, in *Alloy Phase Diagrams*, A. International, Editor. 1992, ASM International: Materials Park, OH.

2. Okamoto, H., *Al--Ni (Aluminum--Nickel)* Journal of Phase Equilibria, 1993. **14**(2): p. 257-259.

3. Liu, C.T. and J.O. Stiegler, *Ordered Intermetallics: Introduction*, in *Properties and Selection: Nonferrous Alloys and Special-Purpose Materials*, A. International, Editor. 1992, ASM International: Materials Park, OH

4. Deevi, S.C. and W.J. Zhang, *Nickel Aluminides*, in *Encyclopedia of Materials: Science and Engineering*, K.H.J. Buschow, et al., Editors. 2001, Elsevier Science Ltd: New York.

5. Sauthoff, G., *Intermetallics*. 1995, New York: VCH.

6. Dey, G.K., *Physical metallurgy of nickel aluminides*. Sadhana, 2003. **28**: p. 247-262.

7. Liu, C.T. and D.P. Pope, *Ni₃Al and its Alloys*, in *Structural Applications of Intermetallic Compounds*, J.H. Westbrook and R.L. Fleisher, Editors. 2000, John Wiley and Sons Ltd. p. 15-32.

8. Liu, C.T., C.L. White, and J.A. Horton, *Effect of boron on the grain boundaries of Ni₃Al*. Acta Metallurgica, 1985. **33**: p. 213-229.

9. Liu, C.T., *Recent advances in ordered intermetallics*. Materials Chemistry and Physics, 1995. **42**: p. 77-86.

149

10. Deevi, S.C., V.K. Sikka, and C.T. Liu, *Processing, Properties, and Applications of Nickel and Iron Aluminides.* Progress in Materials Science, 1997. **42**: p. 177-192.

11. Liu, C.T. and J.O. Stiegler, *Ordered Intermetallics: Nickel Aluminides*, in *Properties and Selection: Nonferrous Alloys and Special-Purpose Materials*, A. International, Editor. 1992, ASM International: Materials Park, OH

12. Sikka, V.K., et al., *Large-Scale Manufacturing of Nickel Aluminide Transfer Rolls for Steel Austenitizing Furnaces.* Intermetallics, 2004. **12**: p. 837-844.

13. Sikka, V.K., S.C. Deevi, and J.D. Vought, *Exo-Melt: A Commercially Viable Process.* Advanced Materials and Processes, 1995. **6**: p. 29-31.

14. Dannohl, H.D. and H.L. Lukas, *Calorimetric Determination of the Enthalpies of Formation of Intermetallic Compounds.* Z. Metallkunde, 1974. **65**: p. 642.

15. Lui, S.C., et al., *Electronic and Vibrational Properties of Nickel Aluminum Alloy.* Phys. Rev. B, 1990. **42**: p. 1582.

16. Ayushina, G.D., E.S. Levin, and P.V. Gel'd, *Density and Surface Energy of Liquid alloys of Aluminum with Cobalt and Nickel.* Russian Journal of Physical Chemistry, 1969. **43**: p. 1548.

17. Bradley, A.J. and A. Taylor, *An X-Ray Analysis of the Nickel-Aluminide System.* Proceedings of the Royal Society of London A, 1937. **159**(896): p. 56-72.

18. Taylor, A. and N.J. Doyle, *Further Studies on Nickel-Aluminum System .1. Beta-NiAl and Delta-Ni₂Al₃ Phase Fields.* Journal of Applied Crystallography, 1972. **5**: p. 201.

19. Noebe, R.D., R.R. Bowman, and M.V. Nathal, *Physical and Mechanical Properties if the B2 Compound NiAl.* International Materials Reviews, 1993. **38**(4): p. 193-232.

150

20. Georgopoulos, P. and J.B. Cohen, *Defect Structure and Debye Waller Factors vs. Composition in Beta-NI$_{1+/-x}$AL$_{-1+/-x}$.* Scripta Metallurgica, 1977. **11**: p. 147-150.

21. Fraser, H.L., et al., *Annealing of Point-Defects in Quenched NiAl.* Philosophical Magazine, 1975. **32**: p. 873-875.

22. Ortiz, C. and J.E. Epperson, *OMEGA-LIKE DIFFRACTION EFFECTS FROM BETA'-NIAL* Scripta Metallurgica, 1979. **13**: p. 237-239.

23. Wasilewski, R.J., *Structure Defects in CsCl Intermetallic Compounds .I. Theory* J. Phys. Chem. Solids., 1968. **29**: p. 39-49.

24. Guard, R.W. and A.M. Turkalo, *Fractographic Studied in NiAl and Ni$_3$Al,* in *Mechanical properties of Intermetallic Compounds,* J.H. Westbrook, Editor. 1960, John Wiley and Sons Inc.: New York. p. 141-160.

25. Enami, K., S. Nenno, and K. Shimizu, *Crystal-Structure and Iinternal Twins of Ni-36.8 at Percent A1 Martensite.* Transactions of the Japanese Institute of Metals, 1973. **14**(2): p. 161.

26. Tanner, L.E., et al., *Pre-Martensitic Microstructures in Ni-Al Ordered BETA-2 Phase .1. Effects Induced by Cooling* Scripta Metallurgica, 1990. **24**: p. 1731.

27. Bauccio, M.L., ed. *ASM Metals Reference Handbook.* third ed. 1993, ASM International: Materials Park, OH. 614.

28. Darolia, R., *Ductility and Fracture Issues Related to the Implementation of NiAl for Gas Turbine Applications.* Intermetallics, 2000. **8**: p. 1321-1327.

29. Wasilewski, R.J., *Elastic Constants and Young's Modulus of NiAl.* Transactions of the Metallurgical Society of AIME, 1966. **236**: p. 455-457.

30. Rusovic, N. and H. Warlimont, *The Elastic Behaviour of B2-NiAl Alloys.* Physica Status Solidi A, 1977. **44**: p. 609.

31. Rusovic, N. and H. Warlimont, *Young's modulus of B2 NiAl alloys.* Physica Status Solidi, 1979. **53**: p. 283-288.

32. Harmouche, M.R. and A. Wolfenden, *Temperature and Composition Dependence of Young's Modulus in Polycrystalline B2 NiAl.* Journal of Testing and Evaluation, 1987. **15**(2): p. 101-104.

33. Terada, Y., et al., *Thermal Conductivity of B2-Type Aluminides and Titanides.* Intermetallics, 1995. **3**: p. 347-355.

34. Darolia, R., *NiAl Alloys for High-Temperature Structural Applications.* JOM, 1991. **43**(3): p. 44-49.

35. Terada, Y., et al., *Effects of Ternary Additions on Thermal Conductivity of NiAl.* Intermetallics, 1999. **7**: p. 717-723.

36. Eisenkolb, F. and H.E. Roellig, *Development of scale resistant nickel aluminum base materials.* Neue Huette, 1958. **3**(12): p. 721-731.

37. Goward, G.W., *Current research on surface protection of superalloys for gas turbine engines.* Journal of Metals, 1970. **22**(10): p. 31.

38. Doychak, J., J.L. Smialek, and T.E. Mitchell, *Transient oxidation of single-crystal beta-NiAl.* Metallurgical Transactions A, 1989. **20A**: p. 499.

39. Grabke, H.J., *Oxidation of NiAl and FeAl.* Intermetallics, 1999. **7**: p. 1153.

40. Barrett, C.A., *Effect of 0.1 at.% Zirconium on the Cyclic Oxidation Resistance of Beta-NiAl.* Oxidation of Metals, 1988. **30**(5/6): p. 361-389.

41. Chen, W.

42. Meier, G.H. and F.S. Pettit, *Oxidation behaviour of intermetallic compounds.* Materials Science & Engineering A, 1992. **A153**: p. 548.

43. vonMises, R., *Mechanik der plastichen Formanderung von Kristallen. Z.* Agnew. Math. Mech, 1928. **8**: p. 161.

44. Rozner, A.G. and R.J. Wasilewski, *Tensile Properties of NiAl and NiTi.* Journal of the Institute of Metals, 1966. **94**: p. 169-175.

45. Ball, A. and R.E. Smallman, *The Operative Slip System and General Plasticity of NiAl--II.* Acta Metallurgica, 1966. **14**: p. 1517.

46. Ball, A. and R.E. Smallman, *The Deformation Properties and Electron Microscopy Studies of the Intermetallic Compound NiAl.* Acta Metallurgica, 1966. **14**: p. 1349-1355.

47. Grala, E.M., *Investigation of NiAl and Ni₃Al*, in *Mechanical Properties of Intermetallics Compounds*, J.H. Westbrook, Editor. 1960, Wiley: New York. p. 358.

48. Hahn, K.H. and K. Vedula, *Room Temperature Tensile Ductility in Polycrystalline B2 NiAl.* Scripta Metallurgica, 1989. **23**: p. 7-12.

49. Nagpal, P. and I. Baker, *The Effect of Grain Size on the Room - Temperature Ductility of NiAl.* Scripta Metallurgica et Materialia, 1990. **24**: p. 2381-2384.

50. Miracle, B.B., *The Physical and Mechanical Properties of NiAl.* Acta Metallurgical et Materialia, 1993. **41**(3): p. 649-684.

51. Cotton, J.D., *The influence of chromium on structure and mechanical properties of B2 nickel aluminide alloys.* 1991, University of Florida. p. 159.

52. Pascoe, R.T. and C.W.A. Newey, *Deformation Modes of the Intermediate Phase NiAl.* Physica Status Solidi, 1968. **29**: p. 357-366.

53. Lloyd, C.H. and M.H. Loretto, *Dislocations in Extruded Beta-NiAl.* Physica Status Solidi, 1970. **89**: p. 163-170.

54. Baker, I., *A Review of the Mechanical Properties of B2 Compounds.* Materials Science & Engineering A, 1995. **A192/193**: p. 1-13.

55. Wasilewski, R.J., S.R. Butler, and J.E. Hanlon, *Plastic Deformation of Single-Crystal NiAl.* Transactions of the Metallurgical Society of AIME, 1967. **239**: p. 1357-1364.

56. Sun, Y.Q. and N. Yang, *The Onset and Blocking of <011> Slip in NiAl.* Acta Materialia, 2003. **51**: p. 5601-5612.

57. Miracle, D.B., *Deformation of NiAl BiCrystals.* Acta Metallurgica et Materialia, 1991. **39**(7): p. 1457-1468.

58. Lahrman, D.F., R.D. Field, and R. Darolia, *The Effects of Strain Rate on the Mechanical Properties of Single Crystal NiAl.* Materials Research Society Symposia Proceedings, 1991. **213**: p. 603-607.

59. Fischer, R., G. Frommeyer, and A. Schneider, *APFIM investigation on site preferences, superdislocations, and antiphase boundaries in NiAl(Cr) with B2 superlattice structure.* Materials Science and Engineering A, 2003. **353**: p. 87-91.

60. Hong, T. and A.J. Freeman, *Effect of Antiphase Boundaries in Electronic Structure and Bonding Character of Intermetallic Systems: NiAl.* Physical Reviews B, 1991. **43**(8): p. 6446-6458.

61. Darolia, R., et al. *Alloy Modeling and Experimental Correlation for Ductility Enhancement in NiAl.* in *High-Temperature Ordered Intermetallic Alloys III.* 1988. Boston, Massachusetts, USA: Materials Research Society.

62. Hong, T. and A.J. Freeman, *Electronic Structure and Mechanical Properties of Intermetallics: APB Energies in Ni--AL-Based Systems*, in *High-Temperature Ordered Intermetallic Alloys III*, C.T. Liu, Editor. 1989, Materials Research Society: Boston, Massachusetts.

63. Baker, I. and E.M. Schulson, *The Structure of Extruded NiAl.* Metallurgical Transactions A, 1984. **15A**: p. 1129-1136.

64. Schulson, E.M. and D.R. Barker, *A Brittle to Ductile Transition in NiAl of a Critical Grain Size.* Scripta Metallurgica, 1983. **17**: p. 519-522.

154

65.   Raj, S.V., R.D. Noebe, and R. Bowman, *Observation of the Brittle to Ductile Transition Temperature of B2 Nickel Aluminides With and Without Zirconium.* Scripta Metallurgica, 1989. **23**: p. 2049-2054.

66.   George, E.P. and C.T. Liu, *Brittle Fracture and Grain Boundary Chemistry of Microalloyed NiAl.* Journal of Materials Research, 1990. **5**(4): p. 754-762.

67.   Westbrook, J.H. and D.L. Wood, *A source of grain-boundary embrittlement in intermetallics.* Journal of the Institute of Metals, 1963. **91**: p. 174-182.

68.   Law, C.C. and M.J. Blackburn, *Rapidly solidified lightweight durable disk material.* 1987, United Technology Corp., Pratt and Whitney Group: West Palm Beach.

69.   Bowman, R.R., et al., *Correlation of deformation mechanisms with the tensile and compressive behaviour of NiAl as NiAl(Zr) intermetallic alloys.* Metallurgical Transactions A, 1992. **23A**: p. 1493-1508.

70.   Weaver, M.L., et al., *The Effects of Interstitial Content, Heat Treatment, and Prestrain, on the Tensile Properties of NiAl.* Materials Science & Engineering A, 1995. **A192/193**: p. 179-185.

71.   Weaver, M.L., et al., *Observation of Static Strain-Aging in Polycrystalline NiAl.* Intermetallics, 1996. **4**: p. 533-542.

72.   Noebe, R.D. and A. Garg, *Characterization of Nitrogen-Doped NiAl.* Scripta Metallurgica et Materialia, 1993. **30**(7): p. 815-820.

73.   Golberg, D. and G. Sauthoff, *Effects of strain-rate and ageing at 573 and 973 K on the mechanical (compressive) behaviour of <110> oriented ('soft') NiAl single crystals with and withoug microalloying additions of Ti, Zr, and Hf. II.* Intermetallics, 1995. **4**: p. 253-271.

74.   Golberg, D. and G. Sauthoff, *Effects of ageing at 673 K on the compressive behaviour of <110> oriented ('soft') NiAl single crystals*

and polycrystals with and without Ti additions. Intermetallics, 1995. **4**: p. 143-158.

75.   Ebrahimi, F. and T.G. Hoyle, *Brittle-to-Ductile Transition in Polycrystalline NiAl.* Acta Materialia, 1997. **45**(10): p. 4193-4204.

76.   Darolia, R., D. Lahrman, and R. Field, *The Effect of Iron, Gallium, and Molybdenum on the Room Temperature Tensile Ductility of NiAl.* Scripta Metallurgica et Materialia, 1992. **26**: p. 1007-1012.

77.   Noebe, R.D. and M.K. Behbehani, *The effect of microalloying additions on the tensile properties of polycrystalline NiAl.* Scripta Metallurgica et Materialia, 1992. **27**: p. 1795-1800.

78.   Liu, C.T. and J.A. Horton, *Effect of Refractory Alloying Additions on Mechanical Proprties of Near-Stoichiometric NiAl.* Materials Science & Engineering A, 1995. **A192/193**: p. 170-178.

79.   Zhou, J. and J.T. Guo, *Effect of Ag Alloying on the Microstructure and Mechanical and Electrical Properties of NiAl Intermetallic Compound.* Materials Science & Engineering A, 2003. **A339**: p. 166-174.

80.   Guo, J.T. and J. Zhou, *Preliminary investigation of the phosphorus-induced softening in polycrystalline NiAl intermetallic compound.* Journal of Alloys and Compounds, 2003. **352**: p. 255-259.

81.   Locci, I.E., et al., *Microstructural and phase stability of single crystal NiAl alloyed with Hf and Zr.* Journal of Materials Research, 1996. **11**(12): p. 3024-3038.

82.   Messerschmidt, U., et al., *Dislocation Processes During the Deformation of NiAl- 0.2 at.% Ta.* Intermetallics, 1999. **7**: p. 455-466.

83.   Kovalev, A.I., R.A. Barskaya, and D.L. Wainstein, *Effect of alloying on electronic structure, strength and ductility characteristics of nickel aluminide.* Surface Science, 2003. **532-535**: p. 35-40.

84. Wang, Y., W. Chen, and L. Wang, *Micro-indentation and errosion properties of thermal sprayed NiAl intermetallic-based alloy coatings.* Wear, 2003. **254**: p. 350-355.

85. Wang, Y. and W. Chen, *Microstructures, properties and high-temperature carburization resistances of HVOF thermal sprayed NiAl intermetallic-based alloy coatings.* Surface and Coatings Technology, 2004. **183**: p. 18-28.

86. Pellegrini, P.W. and J.J. Hutta, *Investigation of phase relations and eutectic directional solidification on the NiAl-V join.* Journal of Crystal Growth, 1977. **42**: p. 536-539.

87. Field, R.D., R. Darolia, and D.F. Lahrman, *Precipitation in NiAl/Ni2AlTi Alloys.* Scripta Metallurgica, 1989. **23**: p. 1469-1474.

88. Vedula, K., et al., *Alloys based on NiAl for high temperature applications*, in *High Temperature Ordered Intermetallic Alloys*. 1985, Materials Research Society: Pittsburgh. p. 411-421.

89. Takeyama, M. and C.T. Liu, *Microstructures and mechanical properties of NiAl-Ni2AlHf Alloys.* Journal of Materials Research, 1990. **5**: p. 1189-1196.

90. Raman, V.A. and K. Schubert, *On the crystal structure of some alloy phases related to TiAl3.* Z. Metallkunde, 1965. **56**: p. 99-104.

91. Nash, P. and W.W. Liang, *Phase equilibria in the Ni-Al-Ti system at 1173K.* Metallurgical Transactions A, 1985. **16A**: p. 319-322.

92. Nash, P.G., V. Vejins, and W.W. Liang, *The Al-Ni-Ti (aluminum-nickel-titanium) system.* Bulletin of Alloy Phase Diagrams, 1982. **3**: p. 367-374.

93. Villars, P. and L.D. Calvert, *Pearson's handbook of crystallographic data for intermetallic phases.* 1985, Metals Park, Ohio: American Society for Metals.

94. Sauthoff, G., *Mechanical properties of intermetallics at high temperatures* in *High temperature aluminides & intermetallics*, S.H. Whang, et al., Editors. 1990, The Minerals, Metals & Materials Society: Warrendale, Pennsylvania. p. 329-352.

95. Patrick, D.K., et al., *Burger vector transition in Fe-Al-Ni alloys*, in *High-temperature ordered intermetallic alloys IV*. 1991, Materials Research Society: Pittsburg, Pensylvania. p. 267-272.

96. Crimp, M.A. and K. Vedula, *Room-temperature deformation of single-crystal B2 Fe-Al Alloys: the effect of stoichiometry and cooling rates.* philosophical Magazine A, 1991. **63**: p. 559-570.

97. Guha, S., P.R. Monroe, and I. Baker. *Improving the Low Temperature Duility of NiAl.* in *High-Temperature Ordered Intermetallic Alloys*. 1988. Boston, Massachusetts, USA: Materials Research Society.

98. Miracle, D.B., S. Russel, and C.C. Law. *Slip System Modification in NiAl.* in *High-Temperature Ordered Intermetallic Alloys III*. 1988. Boston, Massachusetts: Materials Research Society

99. Cotton, J.D., R.D. Noebe, and M.J. Kaufman, *The effects of chromium on NiAl intermetallic alloys: Part I. Microstructures and mechanical properties.* Intermetallics, 1993. **1**: p. 3-20.

100. Cotton, J.D., R.D. Noebe, and M.J. Kaufman, *The effects of chromium on NiAl intermetallic alloys: Part ii. Slip systems.* Intermetallics, 1993. **1**: p. 117-126.

101. Tian, W.H., C.S. Han, and M. Nemoto, *Precipitation of alpha-Cr in B2-Ordered NiAl.* Intermetallics, 1999. **7**: p. 59-67.

102. Fischer, R., G. Frommeyer, and A. Schneider, *Chromium Precipitation in B2-Ordered NiAl-2 at.% Cr Alloys Investigated by Atom Probe Field Ion Microscopy.* Materials Science & Engineering A, 2002. **A327**: p. 47-53.

103. Fischer, R., et al., *Precipitation of Cr-rich phases in a Ni-50Al-2Cr (at.%) alloy*. Intermetallics, 2006. **14**: p. 156.

104. Nagpal, P. and I. Baker, *Effect of Cooling Rate on Hardness of FeAl and NiAl*. Metallurgical Transactions A, 1990. **21A**: p. 2281.

105. Pollock, T.M., et al., *A Comparative Analysis of Low Temperature Deformation in B2 Aluminides*. Materials Science & Engineering A, 2001. **A317**: p. 241-248.

106. Zhou, J. and J.T. Guo, *The Phosphorus Effect on the Superplastic Deformation of NiAl*. Materials Science & Engineering A, 2003. **A360**: p. 140-145.

107. Jayaram, R. and M.K. Miller, *Direct Observation of Zirconium Segregation to Dislocations and Grain Boundaries in NiAl*. Scripta Metallurgica et Materialia, 1995. **33**(1): p. 19-26.

108. Westbrook, J.H., *Temperature Dependance of Hardness of the Equiatomic Iron Groupo Aluminides*. Journal of the Electrochemical Society, 1956. **103**: p. 54-63.

109. Vedula, K., K.H. Hahn, and B. Boulogne. *Room Temperature Tensile Ductility in Polycrystalline B2 NiAl*. in *High-Temperature Ordered Intermetallic Alloys III*. 1988. Boston, Massachusetts, USA: Materials Research Society.

110. Bozzolo, G., R.D. Noebe, and F. Honecy, *Modeling of ternary element site substitution in NiAl*. Intermetallics, 2000. **8**: p. 7-18.

111. Field, R.D., D.F. Lahrman, and R. Darolia, *Effect of alloying on slip systems in <001> oriented single crystals*. Acta Metallurgica et Materialia, 1991. **39**(12): p. 2961-2969.

112. Tiwari, R., et al., *Development of NiAl-Based Intermetallic Alloys: Effect of Chromium Addition*. Materials Science & Engineering A, 1995. **A192/193**: p. 356-363.

113.   Kumar, K.S., S.K. Mannan, and R.K. Viswanandham, *Fracture toughness of NiAl and NiAl-based composites*. Acta Metallurgica et Materialia, 1992. **40**(6): p. 1201-1222.

114.   Kim, T., K.T. Hong, and K.S. Lee, *The relationship between the fracture toughness and grain boundary character distribution in pollycrystalline NiAl*. Intermetallics, 2003. **11**: p. 33-39.

160